

# JOURNAL DES MATERIAUX NUCLEAIRES

## OF NUCLEAR MATERIALS

A JOURNAL ON METALLURGY, CERAMICS AND SOLID  
STATE PHYSICS IN THE NUCLEAR ENERGY INDUSTRY

### EDITORS:

R. W. CAHN — BIRMINGHAM, ENGLAND  
J. P. HOWE — CANOGA PARK, U.S.A. — P. LACOMBE — PARIS, FRANCE

### CONTENTS

T. H. BLEWITT, R. R. COLTMAN, R. E. JAMISON and J. K. REDMAN, Radiation hardening of copper single crystals . . . . .	277
A. SAULNIER, Etude structurale du beryllium par micrographie et microdiffraction électroniques sur coupes minces . . . . .	299
L. E. RUSSELL, J. D. L. HARRISON and N. H. BRETT, Perovskite-type compounds based on plutonium . . . . .	310
A. SAWATZKY, Hydrogen in zircaloy-2: its distribution and heat of transport .	321
C. W. TUCKER Jr. and F. J. NORTON, On the location and motion of rare gas atoms in metals . . . . .	329
ROGER CHANG, Phase transformation, twinning and anelastic phenomenon associated with zirconium dihydride . . . . .	335
D. SMART, A method suitable for the measurement of the thermal diffusivity of irradiated materials . . . . .	341
FRANCIS J. NORTON and C. W. TUCKER Jr., Krypton evolution from metallic uranium . . . . .	350

#### *Letter to the Editors — Lettre aux Rédacteurs*

S. E. BRONISZ and A. E. GORUM, The plastic deformation of monoclinic alpha plutonium . . . . .	353
Book Reviews . . . . .	356
News Item . . . . .	357
Author Index . . . . .	359
Subject Index . . . . .	361



NORTH-HOLLAND PUBLISHING COMPANY — AMSTERDAM

## EDITORIAL ADVISORY BOARD — CONSEIL DES REDACTEURS

S. AAS (Kjeller, Norway)  
K. F. ALDER (Lucas Heights, Australia)  
P. ALBERT (Vitry, France)  
G. W. ARDLEY (Whetstone, U.K.)  
J. E. BURKE (Schenectady, U.S.A.)  
R. CAILLAT (Saclay, France)  
G. CHAUDRON (Vitry, France)  
H. CHISWICK (Argonne, U.S.A.)  
A. T. CHURCHMAN (Bristol, U.K.)  
A. S. COFFINBERRY (Los Alamos, U.S.A.)  
A. H. COTTRELL (Cambridge, U.K.)  
R. L. CUNNINGHAM (Ottawa, Canada)  
C. DECROLY (Bruxelles, Belgium)  
M. D'HONT (Mol, Belgium)  
J. D. FAST (Eindhoven, Netherlands)  
H. M. FINNISTON (Newcastle, U.K.)  
J. FRIEDEL (Paris, France)

E. GEBHARDT (Stuttgart, Germany)  
E. GRISON (Saclay, France)  
R. E. HASIGUTI (Tokyo, Japan)  
J. HERENGUEL (Antony, France)  
L. K. JETTER (Oak Ridge, U.S.A.)  
R. KIESSLING (Stockholm, Sweden)  
K. LÜCKE (Aachen, Germany)  
B. LUSTMAN (Pittsburgh, U.S.A.)  
R. MADDIN (Philadelphia, U.S.A.)  
A. MERLINI (Milan, Italy)  
P. MURRAY (Harwell, U.K.)  
R. MYERS (Sydney, Australia)  
E. C. W. PERRYMAN (Culcheth, U.K.)  
J. A. L. ROBERTSON (Chalk River, Canada)  
J. A. SABATO (Buenos Aires, Argentina)  
K. TANGRI (Bombay, India)  
P. VACHET (Paris, France)

*Papers or letters* should be sent to one of the Editors,

R. W. CAHN (Dept. of Metallurgy, University of Birmingham, Birmingham 15, England).  
J. P. HOWE (Atomics International, P.O. Box 309, Canoga Park, California, U.S.A.).  
P. LACOMBE (Centre de Recherches Métallurgiques de l'Ecole des Mines, Blvd. St. Michel 60, Paris VI, France)

either directly or through a member of the Editorial Advisory Board.

*Papers or letters* should be written in English, French or German; papers should have a summary in the appropriate language. Translations of the summary into the two other languages will be added by the Editors.

*Instructions to contributors* will be found in Vol. 1, No. 1 (pp. 111-112).

*Books for review* should be sent to one of the Editors.

*The Journal of Nuclear Materials* will be published bi-monthly.

*The subscription price of a volume of 360 pages is \$ 18.00, 130s., Gld. 68.50 per volume, post-free.*

*Subscriptions* should be sent to the publishers, North-Holland Publishing Company, P.O. Box 103, Amsterdam or to any subscription-agent.

No part of this issue may be reproduced in any form, by print, photoprint, microfilm or any other means without written permission from the publisher. Reprints, photoprints or microfilms are obtainable at cost from the publisher.

*Les articles ou les lettres* devront être envoyés à un des Rédacteurs-en-chef,

R. W. CAHN (Dept. of Metallurgy, University of Birmingham, Birmingham 15, England).  
J. P. HOWE (Atomics International, P.O. Box 309, Canoga Park, California, U.S.A.).  
P. LACOMBE (Centre de Recherches Métallurgiques de l'Ecole des Mines, 60 Bd. St. Michel, Paris VI, France)

ou directement ou par un membre du Conseil des Rédacteurs.

*Les articles ou les lettres* devront être rédigés en anglais, français ou allemand, les articles avec un résumé dans la langue correspondante. Les traductions du résumé dans les deux autres langues seront ajoutées par les éditeurs.

*Les instructions aux auteurs* se trouvent dans le Vol. 1, No. 2 (pp. 211-212).

*Les Livres (exemplaires de presse)* devront être envoyés à un des Rédacteurs-en-chef.

*Le Journal des Materiaux Nucleaires* paraîtra tous les deux mois.

*Prix de souscription* par volume d'environ 360 pages: \$ 18.00, 130s., Gld. 68.50, franco.

*Les abonnements* devront être envoyés aux éditeurs, North-Holland Publishing Company, P.O. Box 103, Amsterdam, ou à votre librairie.

## RADIATION HARDENING OF COPPER SINGLE CRYSTALS

T. H. BLEWITT, R. R. COLTMAN, R. E. JAMISON <sup>†</sup> and J. K. REDMAN

*Solid State Division, Oak Ridge National Laboratory, <sup>††</sup> Tennessee, USA*

Received 4 January 1960

The effect of nuclear radiation on the mechanical properties of copper has been studied. It has been found that the yield stress, which is substantially increased by the radiation, increases as the cube root of the flux. A strong temperature dependence of the yield stress of irradiated copper is observed with the yield stress being given by a function similar to  $\sigma = A - BT^{\frac{1}{3}}$  above 40° K. A Lüders band with slip lines of very large step height is associated with the enhanced yield stress at small strains. At large strains the phenomenon of overshoot is observed.

The annealing kinetics of the radiation hardness have also been studied in the temperature range from 25° K to 700° K. Little or no annealing is observed in the region below 80° K. In the region from 80° K to 300° K approximately 20 % of the yield stress is recovered, with the remainder annealing in the range from 600° K to 700° K.

These results have been discussed in terms of the possible mechanisms by which the hardening can occur. While by no means conclusive, these data support a dislocation locking mechanism. On the other hand a very close analogy exists between radiation hardening and the hardening which arises from the addition of impurities, e.g. the hardening in  $\alpha$  brass. The correlation between work hardening and radiation hardening appears to be quite small.

Les auteurs ont étudié l'effet des radiations nucléaires sur les propriétés mécaniques du cuivre.

On a trouvé que la limite élastique, nettement augmentée par les radiations, croît comme la racine cubique du flux. On remarque qu'il existe une relation étroite entre la température et la limite élastique du cuivre irradié, la limite élastique étant donnée par une formule de la forme  $\sigma = A - BT^{\frac{1}{3}}$  au-dessus de 40° K. Une bande de Lüders avec des lignes de glissement aux marches très élevées est associée à l'accroissement notable de la limite élastique aux faibles déformations. Aux fortes déformations, on ob-

serve le phénomène de "overshoot" (glissement sur un plan unique dans le domaine théorique du glissement double).

La cinétique du recuit du durcissement provoqué par l'irradiation a aussi été étudiée entre 25 et 700° K. Peu ou aucun effet de recuit n'est observé aux températures inférieures à 80° K. Entre 80 et 300° K environ, 20 % environ de l'augmentation de la limite élastique due à l'irradiation est restaurée, et l'augmentation restante disparaît entièrement par recuit entre 600 et 700° K.

Ces résultats sont discutés en considérant les mécanismes éventuels qui peuvent causer le durcissement. Bien qu'il ne soit pas possible de conclure, on pourrait les expliquer par un mécanisme de blocage de dislocations. D'autre part, il y a une grande analogie entre le durcissement dû aux radiations et celui qui est causé par l'addition d'impuretés, comme par exemple dans le cas du laiton  $\alpha$ . Il semble y avoir peu de corrélation entre les durcissements causés respectivement par écrouissage ou radiations.

Es wurde der Einfluss von Reaktor-Bestrahlung auf die mechanischen Eigenschaften von Kupfer untersucht. Dabei wurde gefunden, dass die Streckgrenze, die unter Bestrahlung beträchtlich anwächst, proportional zur dritten Wurzel aus dem integrierten Fluss zunimmt. Bei bestrahltem Kupfer tritt eine starke Temperaturabhängigkeit der Streckgrenze auf; oberhalb etwa 40° K lässt sie sich durch  $\sigma = A - BT^{\frac{1}{3}}$  annähern. Mit der Erhöhung der Streckgrenze geht das Auftreten von Lüders-Bändern mit Gleitlinien sehr hoher Stufenhöhe einher. Während dieser Effekt bei kleinen Dehnungen auftritt, wurde bei grossen Dehnungen sogenanntes Überschiessen beobachtet.

Die Erholungskinetik der Bestrahlungsverfestigung wurde ebenfalls untersucht und zwar im Temperaturbereich zwischen 25° K und 700° K. Unterhalb 80° K wurde nur wenig oder keine Erholung festgestellt,

<sup>†</sup> Now with the Research Department of Carrier Corporation, Syracuse, New York.

<sup>††</sup> Oak Ridge National Laboratory is operated by Union Carbide Corporation for the United States Atomic Energy Commission.

während etwa 20 % der Streckgrenze im Bereich zwischen 80 und 300° K und der Rest zwischen 600 und 800° K ausheilt.

Die Ergebnisse werden an Hand verschiedener, möglicher Verfestigungsmechanismen diskutiert. Wenn auch in keiner Weise schlüssig, so sprechen die Ergebnisse doch für das Vorliegen einer Versetzungs-

Verankerung. Des weiteren wird eine weitgehende Analogie zwischen der Bestrahlungsverfestigung und der Verfestigung, die beim Zulegieren fremder Elemente auftritt, beispielsweise beim  $\alpha$ -Messing, festgestellt. Eine Korrelation zwischen Bestrahlungsverfestigung und Verformungsverfestigung scheint jedoch kaum zu bestehen.

## 1. Introduction

It is well known that the bombardment of metals by energetic nucleons induces substantial changes in their physical and mechanical properties<sup>1)</sup>. It has generally been accepted that these changes occur, at least in part, from vacant lattice sites and interstitial atoms generated by the collision of the energetic nucleons with atoms of the solid. In the case of bombardment with neutrons, protons, deuterons, and alpha particles, theoretical considerations suggest that in addition to the displaced atoms the atomic collisions of the nucleons generate sufficient thermal agitation that a small region of about  $10^4$  atoms may be considered to have been raised to a temperature above the melting point<sup>2)</sup>. The effect that this region (it can be called a thermal spike or a displacement spike † depending upon the range of the primary displacement) has on the physical properties of metal depends to a high degree on the duration of the high temperature. While in some cases – particularly those alloys which have a high temperature phase which can be retained at lower temperatures by quenching<sup>3)</sup> – there are indications that the thermal spike induces permanent changes, to date there are no experimental results on the effects of radiation on pure nonfissile metals which unambiguously require the concept of the thermal spike.

Several models of radiation damage have been devised to account for the observed annealing of samples damaged at very low temperatures<sup>4,5,6)</sup>. These models have been based on the assignment of a specific defect to

the annealing peaks in the disturbed metals. Not only have the annealing spectra of irradiated metals been considered, but those of deformed and quenched metals have also been utilized. Unfortunately, these studies have depended to a great extent on the results of the experimental studies based on changes in the electrical resistivity. As a consequence, many of these models have not attempted to explain the phenomenon of radiation hardening despite the very large effects which are observed and have largely ignored these experimental data, justifiably perhaps, because most data have been taken following room temperature bombardment. The most recent experiments at Oak Ridge remove this deficiency to some extent by measuring the low temperature mechanical properties of crystals following a low temperature bombardment. The results seem to indicate that the consideration of the mechanical properties will play an important role in the final analysis of the phenomenon of radiation damage. The authors have always felt that the study of the effects of neutron irradiation on the mechanical properties of metal single crystals would provide valuable information pertaining to the nature of radiation damage. An active research program has been underway since 1950 with a particular emphasis on the study of the stress-strain curve of copper following bombardment in a nuclear reactor. The results of this study have been for the most part published only in abstract form. While the present study is incomplete in the sense that a mechanism of radiation hardening is not now understood, the publishing of these data may be justified on the basis that these data will point out some of the weak points in the theories of radiation hardening and the more general radiation damage theories which have been proposed.

† Recent experiments by R. A. Schmitt and R. A. Sharp, Phys. Rev. Ltrs., 1, No. 12 (1958), show that the range of displaced particles is quite large, suggesting that some modification in the concept of a displacement spike may be necessary.

## 2. Experimental Techniques

The research described here has been centered about the study of the mechanical properties of copper single crystals with measurements of the stress-strain curve and the yield stress being made at temperatures ranging from room temperature to liquid helium temperature. The strain markings associated with radiation hardness and the annealing of radiation hardness has also been studied. For the most part these measurements have been made following a room temperature bombardment after sufficient time (about one week) for radioactive decay to occur so that the usual techniques followed for the study of the mechanical properties of unirradiated crystals could be used. These techniques have been previously described<sup>7,8</sup>. In those cases where modifications were necessary, a description of the modification will be made.

Samples were bombarded in the Oak Ridge Graphite Reactor when moderate doses were desired ( $6 \times 10^{18}$  nvt or less). This reactor with a thermal neutron flux of  $1 \times 10^{12}$  neutrons/cm<sup>2</sup> is air-cooled, graphite moderated, and fueled with natural uranium. With the exception of a few samples bombarded near liquid hydrogen temperature, all samples were bombarded in a natural uranium cylinder located near the geometrical center of the reactor. The ambient temperature in this facility is about 30° C. The spectrum of the neutron energies in this reactor is given by  $N(E) \propto 1/E$ , where  $N(E)$  is the number of neutrons of energy  $E$ , but, of course, in the center of the uranium cylinder the spectrum is greatly enhanced at the fission energy at the expense of the thermal neutrons. These fast neutrons increase the damage rate, measured by the changes of the electrical conductivity and the yield stress in copper, by a factor of 4 to 5 relative to the normal  $1/E$  spectrum. In the case of bombardments in Hole 12, the flux has been accurately measured, and the distribution of the flux can be determined from these measurements. The doses for samples bombarded in the graphite reactor will be specified in this paper by the thermal neutron dose.

Heavy neutron doses were obtained by bombardment in the Oak Ridge Low Intensity Test Reactor. This reactor, an MTR type with a thermal neutron flux of  $2 \times 10^{13}$  neutrons/cm<sup>2</sup>, is water-cooled, water-moderated, and fueled with enriched uranium. The samples were bombarded in a specially prepared fuel element (MTR type) with the central 9 plates removed to provide a rectangular opening approximately 2.5 cm  $\times$  10 cm (1"  $\times$  4"). Since there was only about 0.3 cm ( $\frac{1}{8}$ ") water between the nearest enriched fuel plate and the sample, the neutron spectrum was probably somewhat similar to that in the uranium cylinder of the graphite reactor. The flux of the fuel element facility in the LITR was calibrated in relation to the flux in the uranium cylinder of the graphite reactor by determining the change in yield stress of copper single crystals. Thus, the thermal neutron dose ascribed to samples bombarded in the LITR reactor is that which would produce an equivalent amount of radiation hardness in a copper crystal bombarded inside a uranium cylinder with a  $1/E$  neutron spectrum.

## 3. Results

### 3.1. STRESS-STRAIN CURVES

The room temperature stress-strain curves of a series of copper single crystals bombarded in the Oak Ridge Graphite Reactor are shown in fig. 1. These results were obtained before it was realized that the stress-strain curve had an orientation dependence, and since each sample of fig. 1<sup>9</sup>) had a different orientation, quantitative results cannot be deduced from these curves. They do, however, illustrate quite well in a qualitative way the four significant changes induced by neutron irradiation. First, it is noted that the yield stress increases with the neutron dose. These effects are quite considerable; for example, the yield stress for  $2 \times 10^{19}$  neutrons/cm<sup>2</sup> was increased by a factor of 22. Second, it is noted that some evidence for an upper yield point is apparent in that the flow stress falls as yielding occurs. Third, there is a region of slight work hardening near the origin suggestive of a Lüders band. Fourth, following

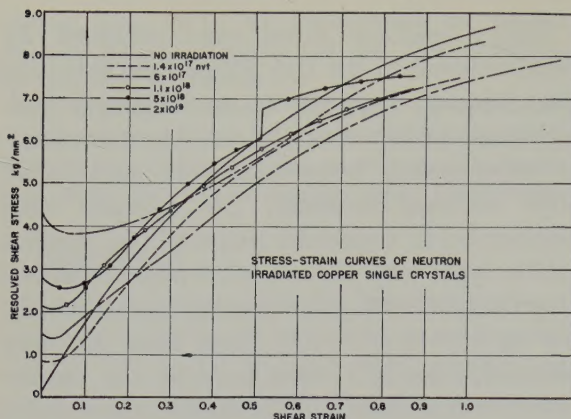


Fig. 1. The stress-strain curves of copper crystals after various neutron doses. The crystals had not the same orientation.

the region of slight work hardening (deformation by a Lüders band), the sample appears to work harden in the normal fashion of the unirradiated crystal. The results of experiments designed to examine each of these points in detail will now be discussed.

### 3.2. YIELD STRESS

The yield stress has been measured as a function of temperature and of dose<sup>10</sup>). In fig. 2 the

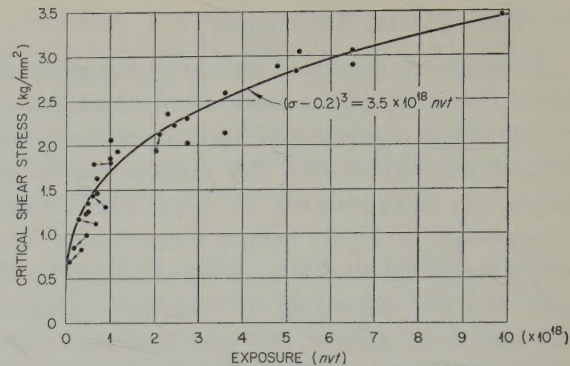


Fig. 2. The effect of neutron dose on the room temperature yield stress of copper single crystals. The solid curve satisfies the equation  $(\sigma - 0.2)^3 = 3.5 \times 10^{18}$  neutrons/cm<sup>2</sup>.

variation of yield stress is shown as a function of the neutron dose up to  $10^{19}$  nvt. The samples were bombarded in the graphite reactor and in the LITR reactor at essentially room temperature, and the yield stress was also measured at room temperature (300° K). It can be seen that the increase in the yield stress fits a curve given by

$$(\sigma - 0.2) = \sigma' = 1.48 \times 10^{-6} \phi^{\frac{1}{3}} \quad (1)$$

where  $(\sigma - 0.2) = \sigma'$  is the increase in yield stress

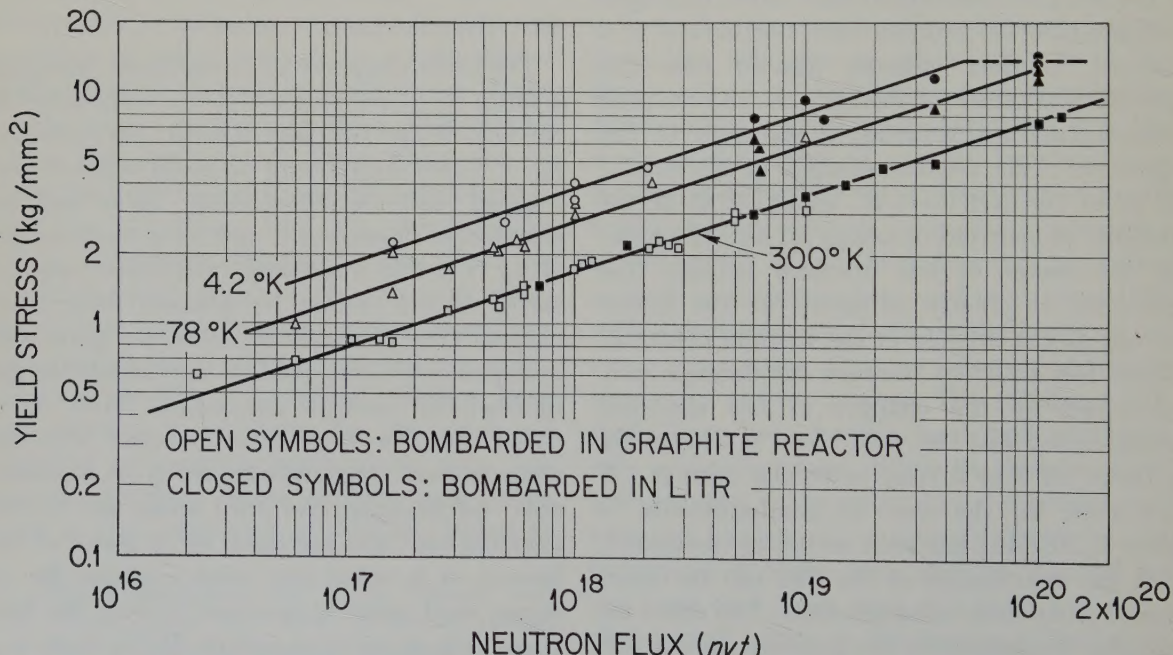


Fig. 3. Effect of neutron irradiation on the yield stress of copper at various temperatures. The log of the yield stress is plotted as a function of the log of the dose. A straight line of slope  $\frac{1}{3}$  is drawn through each set of points.

in  $\text{kg/mm}^2$ , and  $\phi$  is the neutron dose<sup>11</sup> in  $\text{neutrons/cm}^2$ . In fig. 3 the logarithm of the yield stress is plotted against the logarithm of the flux. The fact that a straight line of slope  $\frac{1}{3}$  can be drawn through the data clearly shows that  $\sigma'$  is proportional to the cube root of the flux from  $5 \times 10^{16}$  nvt through  $1 \times 10^{20}$  nvt †.

The yield stress has also been determined as a function of temperature following bombardment at reactor ambient temperatures<sup>12,13</sup>. This property shows a strong dependence on the temperature, increasing significantly as the temperature decreases. These data are plotted in fig. 3 along with the room temperature data. The yield stress at  $78^\circ \text{K}$  is given by

$$(\sigma - 0.2) = \sigma' = 2.80 \times 10^{-6} \phi^{\frac{1}{3}} \quad (2)$$

and at  $4.2^\circ \text{K}$  by

$$(\sigma - 0.2) = \sigma' = 3.80 \times 10^{-6} \phi^{\frac{1}{3}}. \quad (3)$$

While the yield stress varies as the cube root of the flux over the entire range of flux investigated for data obtained at both  $300^\circ \text{K}$  and at  $78^\circ \text{K}$ , it is clear that some form of saturation in the yield stress is observed when measured at  $4.2^\circ \text{K}$  following heavy neutron doses. The yield stress is observed to be of the order of

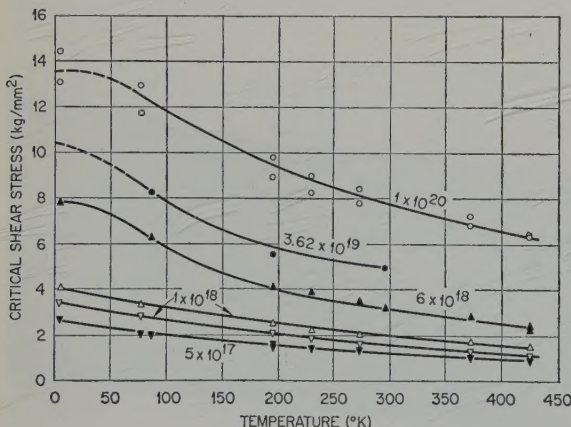


Fig. 4. The temperature dependence of the yield stress of reactor irradiated copper single crystals at various neutron doses. The yield stress is plotted as a function of temperature.

† It should be noted that these are essentially fission spectrum neutrons. Insofar as the hardness is concerned, these neutrons have five times the effect of pile neutrons, i.e., neutrons of a  $1/E$  spectrum.

14  $\text{kg/mm}^2$ . It is believed that this shear stress is the limiting value which can be introduced owing to a change in the mechanism of deformation.

The details of the temperature dependence of the critical shear stress are shown in figs. 4, 5, 6, and 7. In fig. 4 the critical shear stress is plotted as a function of temperature for samples bombarded at fluxes from  $5 \times 10^{17}$  to  $1 \times 10^{20}$ . In fig. 5 the critical shear stress is plotted as a function of  $T^{\frac{1}{3}}$ . A straight line can be drawn through the data as long as the temperature is greater than  $40^\circ \text{K}$ , indicating that the relationship between temperature and shear stress will fit a formula of the type

$$\sigma' = (\sigma - 0.2) = B - AT^{\frac{1}{3}} \text{ when } T \leq 40^\circ \text{K}. \quad (4)$$

The details of the temperature dependence in the low temperature region are shown in fig. 6. These data were obtained on a sample bombarded for one month in the X-10 reactor ( $2 \times 10^{18}$  neutrons/cm<sup>2</sup>) and deformed to the yield point at each indicated temperature.

It is worth emphasizing that the above data, particularly those illustrated in fig. 4, conclusively show that the critical shear stress can be written as

$$\sigma = g(\phi)f(T) \quad (5)$$

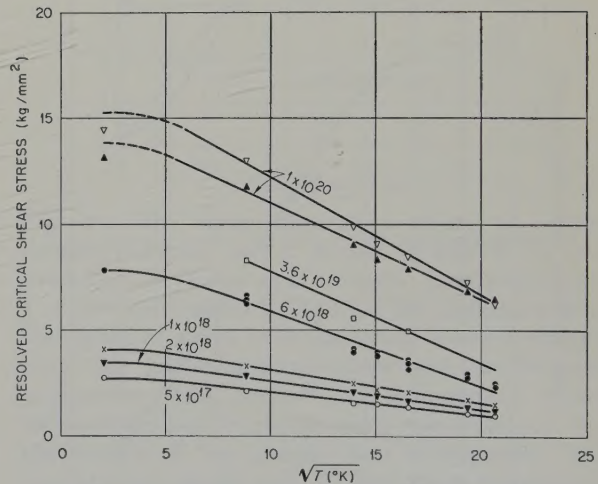


Fig. 5. The temperature dependence of the yield stress of reactor irradiated copper single crystals at various neutron doses. The yield stress is plotted as a function of  $T^{\frac{1}{3}}$ . The curvature at  $T < 40^\circ \text{K}$  is deduced from fig. 6. For  $T > 78^\circ \text{K}$ , a linear relationship can be noted between yield stress and  $T^{\frac{1}{3}}$ .

where  $g$  is independent of  $(T)$  and  $f$  is independent of  $(\phi)$ . The independence of  $g$  and  $f$  is illustrated by fig. 7 where the log of the critical shear stress is plotted as a function of the log of the temperature for a variety of neutron fluxes. It can be noted that each of the curves of different flux are approximately parallel, satisfying the condition that  $g(\phi)$  is independent of the testing temperature  $T$ .

### 3.3. UPPER YIELD POINT AND LÜDERS BAND FORMATION

A yield point followed by a region of small work hardening has been observed on all samples regardless of the temperature of deformation. This yield point and region of small work hardening is intimately connected with the fact that the plastic flow is inhomogeneous. This is rather dramatically illustrated in fig. 8 where the localized deformation can be macroscopically seen. Slip commences at one end of the crystal, and as the deformation continues the deformation front advances toward the other end of the crystal. This mode of deformation, called a Lüders band, has been studied in irradiated crystals, utilizing the density of

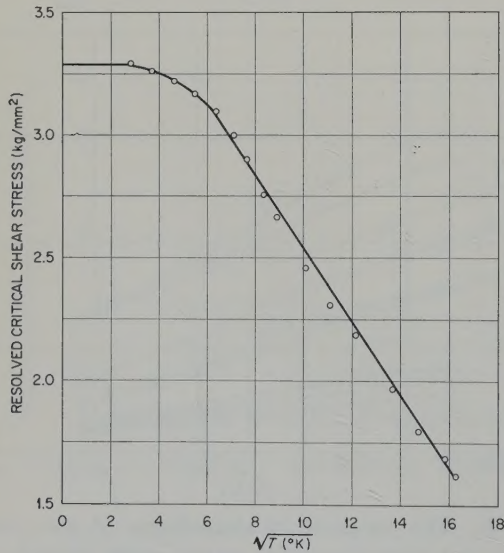


Fig. 6. The temperature dependence of the yield stress of a reactor irradiated copper crystal. The dose was  $1 \times 10^{18}$  neutrons/cm<sup>2</sup>. The yield stress is plotted as a function of  $T^{\frac{1}{2}}$ .

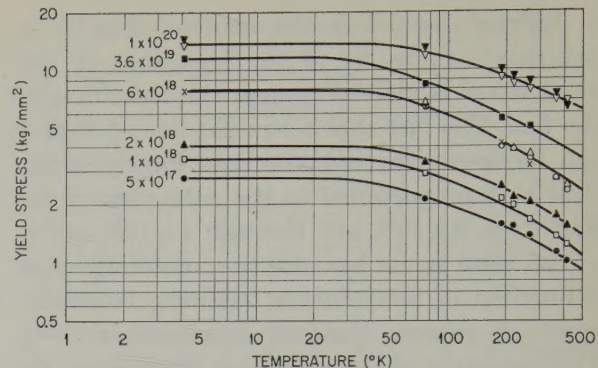


Fig. 7. The temperature dependence of the yield stress of reactor irradiated copper crystals. The log of the yield stress is plotted against the log of the absolute temperature.

slip lines. An experiment was performed whereby the slip lines were removed by electropolishing so that the progress of the deformation front could be followed. Fig. 9 schematically shows the results of this study. It can be seen from this figure that the greatest density of slip lines lies at the front of the Lüders band. No slip lines were observed in advance of the Lüders band, but slip continues behind the advancing

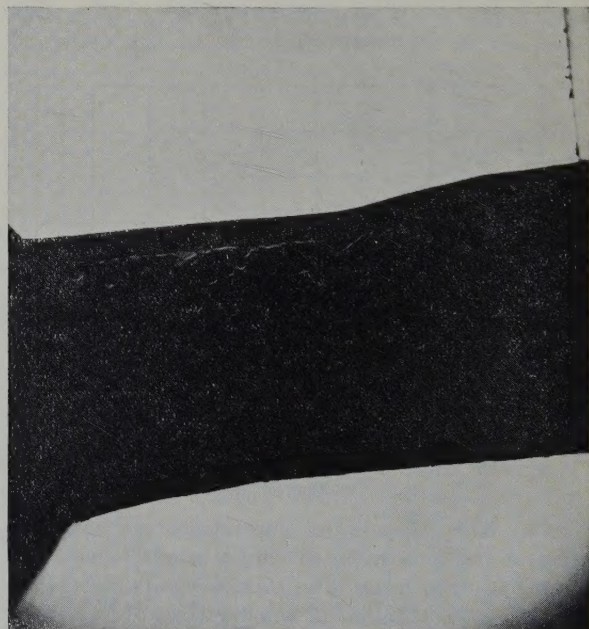


Fig. 8. The silhouette of a heavily irradiated copper crystal after a small deformation. The deformation can be seen to be localized by the offset in the edge of the crystal. Magnification 12  $\times$ .

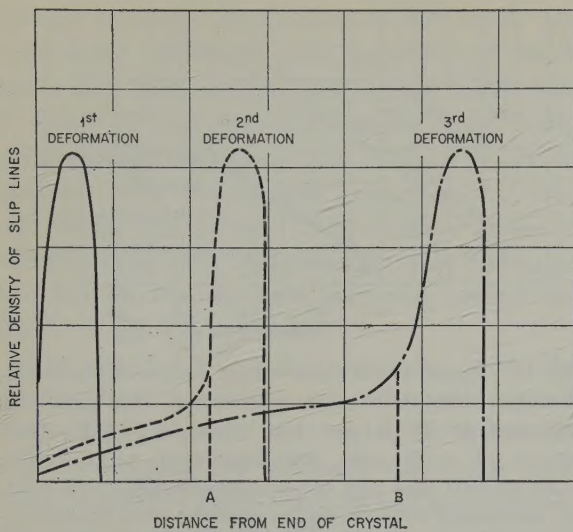


Fig. 9. Schematic diagram illustrating the method of Lüders band formation. The density of slip lines is plotted as a function of strain. After the first deformation, the sample was deformed until the Lüders band had propagated to point A. After all strain markings were polished from the surface and the second deformation was made, the slip lines associated with the deformation were studied. As the schematic diagram shows, no slip lines were observed in the region in advance of the Lüders band, but a small number of lines were observed in the region through which the band had passed.

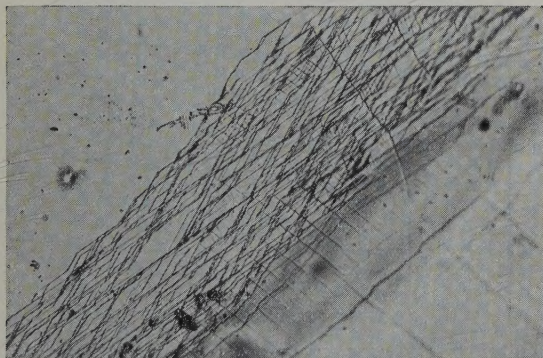


Fig. 10. The Lüders band in a heavily irradiated copper crystal. The tensile axis of this crystal lay on the dodecahedral plane so that simultaneous slip occurred on two systems. The copious amounts of cross slip apparently are the result of the interaction of the slip systems. This sample had been previously deformed, and the slip lines removed by electro-polishing. The sharp delineation of the Lüders band can be observed. Magnification 90  $\times$ .

front, although of diminished intensity. A photomicrograph illustrating this can be seen in fig. 10.

The fact that the load decreases following the yield stress can probably be explained by the local stress magnification introduced at the advancing front of the Lüders band. The upper yield stress can thus be directly attributed to the inhomogeneous nature of the Lüders band. Nothing can be deduced about the nature of the work hardening in the Lüders band. This is, of course, a result of the fact that the hardening occurs on a micro-scale, whereas the load-elongation curve is determined on a macro-

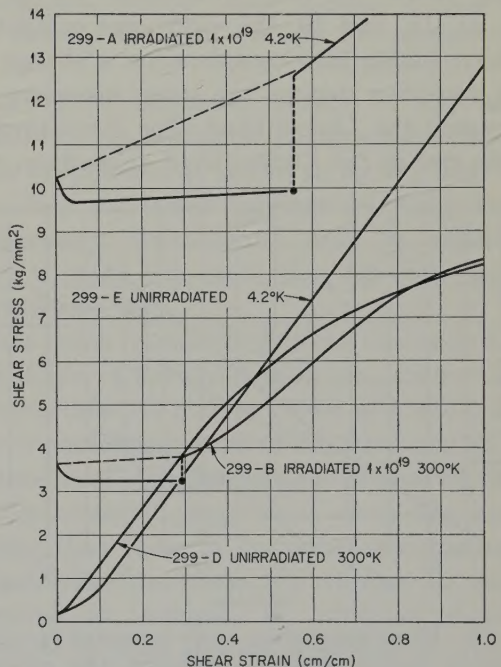


Fig. 11. The shear stress-shear strain of copper crystals obtained at 4.2° K and at 300° K for unirradiated crystals and crystals bombarded for  $1 \times 10^{19}$  neutrons/cm $^2$ . The solid line associated with the region of slight work hardening was determined from the load-elongation curve and the original orientation. This method of computation which differs from that normally used was based on the observation of the Lüders band propagation. The discontinuity at the end of the Lüders band arises as a result of the work hardening which occurs during the Lüders band deformation, and the upper stress at this point is determined by assuming a homogeneous rotation of the crystal. The height of the discontinuity represents the minimum work hardening which occurs in the Lüders band.

scale. All that can be deduced is the shear stress necessary to activate the Lüders band and to keep it propagating. There is, of course, some work hardening as there is a reduction of area and a rotation of the crystal which will increase the stress despite the fact that the load remains nearly constant during the Lüders band propagation (aside from the upper yield stress effect). Thus, at the point where the crystal is filled with the Lüders band and homogeneous strain occurs, a representative yield stress can again be computed; however, between these two points nothing can be deduced about the stress-strain curve. In the stress-strain curves of figs. 11, 12, and 13, the stress was computed without taking into consideration a change in area and thus depicts the stress necessary to propagate the Lüders band. The discontinuity at the end of the Lüders band arises from the

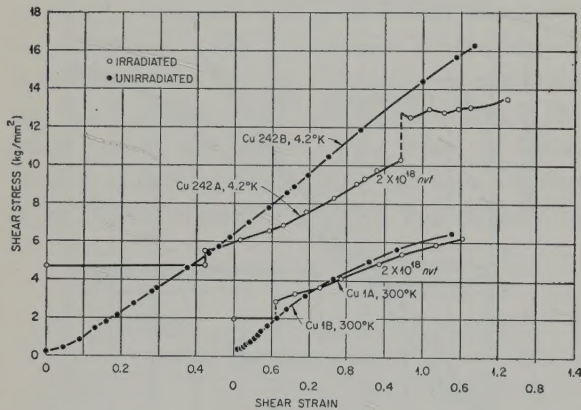


Fig. 12. Shear stress-shear strain curves of two pairs of copper crystals of same orientation. One pair was deformed at 78° K and the other at 300° K. One sample of each pair was irradiated to  $2 \times 10^{18}$  neutrons/cm<sup>2</sup> and the other unirradiated. The solid line associated with the region of slight work hardening was determined from the load-elongation curve and the original orientation. This method of computation which differs from that normally used was based on the observation of the Lüders band propagation. The discontinuity at the end of the Lüders band arises as a result of the work hardening which occurs during the Lüders band deformations, and the upper stress at this point is determined by assuming a homogeneous rotation of the crystal. The height of the discontinuity represents the minimum work hardening which occurs in the Lüders band. The second discontinuity in sample 242-A arises from the onset of duplex slip.

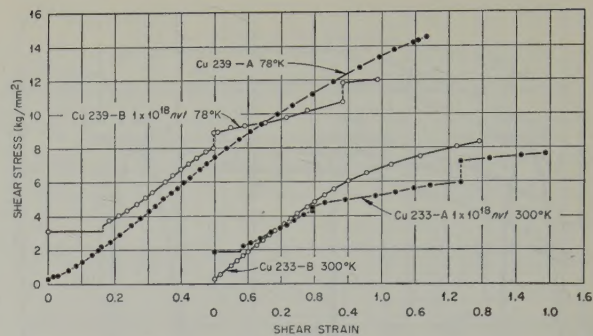


Fig. 13. Shear stress-shear strain curves of two pairs of copper crystals of same orientation. One pair was deformed at 78° K and the other at 300° K. One sample of each pair was irradiated to  $1 \times 10^{18}$  neutrons/cm<sup>2</sup> and the other unirradiated. The solid line associated with the region of slight work hardening was determined from the load-elongation curve and the original orientation. This method of computation which differs from that normally used was based on the observation of the Lüders band propagation. The discontinuity at the end of the Lüders band arises as a result of the work hardening which occurs during the Lüders band deformation, and the upper stress at this point is determined by assuming a homogeneous rotation of the crystal. The height of the discontinuity represents the minimum work hardening which occurs in the Lüders band. The discontinuity in the irradiated samples beyond the first is the result of duplex slip.

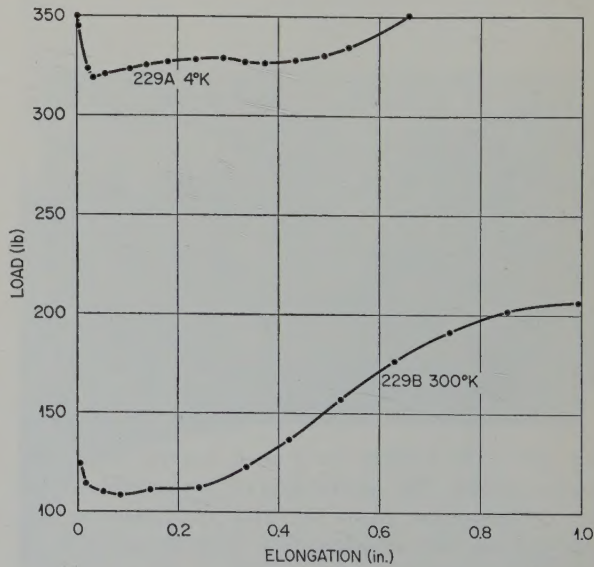


Fig. 14. The load-elongation curve of copper crystals of identical orientation and geometry bombarded for  $1 \times 10^{19}$  neutrons/cm<sup>2</sup> at deformation temperatures of 4.2° K and 300° K.

change in area. This discontinuity does not necessarily represent the amount of work hardening occurring in the Lüders band and, in point of fact, probably arises from a slip process more nearly similar to that in homogeneous flow due to the reduction in area increasing the stress. Undoubtedly, these in combination with the constraints at the grips account for the slip lines occurring behind the front of the Lüders band.

The amount of strain associated with the Lüders band increases with the yield stress. Thus, fig. 14 shows that reducing the deformation temperature increases the strain associated with the Lüders band, as well as increasing the yield stress. In like fashion, an enhancement of the Lüders band will also result when the yield stress is increased by an increase in neutron dose. This is illustrated in figs. 11, 12, and 13. This increase in the strain of the Lüders band can be attributed to the result of an increased step height of each slip line or it can be the

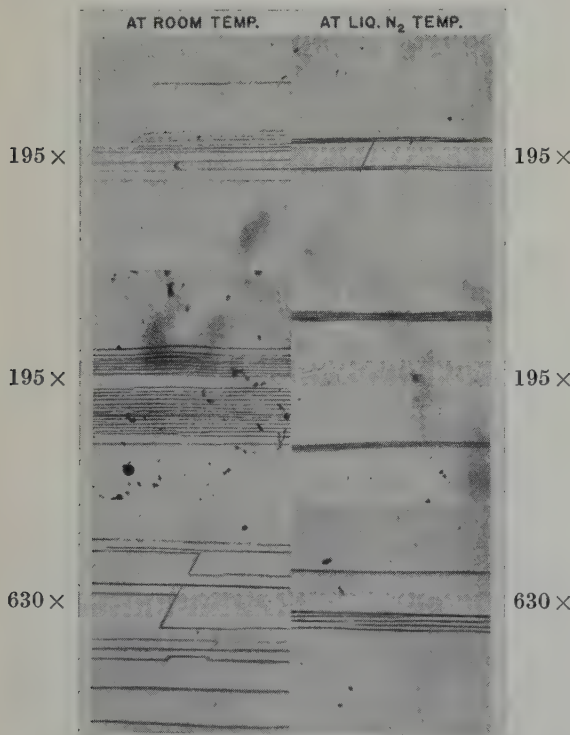


Fig. 15. The effect of temperature on the slip lines of irradiated copper. Single crystals extended 0.9%. Dose  $1 \times 10^{18}$  neutrons/cm<sup>2</sup>.

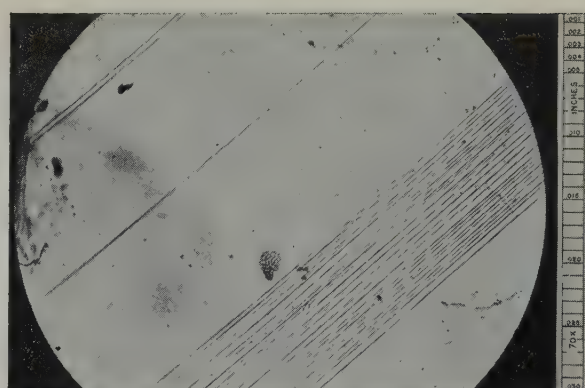


Fig. 16. A Lüders band in irradiated copper. The tensile axis of the crystal is near the center of the stereographic triangle. Small amounts of cross slip can be seen. The dose was  $1 \times 10^{18}$  neutrons/cm<sup>2</sup>.

result of an increased density of slip lines. Studies of the temperature dependence would seem to indicate, as shown in fig. 15, that the slip lines are closer together following lower temperature deformation, and, in addition, there is some indication that the step height increases as well.

It is worth commenting on the obviously high step height of the slip lines in the Lüders band. The slip lines are clearly visible with the naked eye. A photomicrograph of the front end of the Lüders band is shown in figs. 10 and 16. It is readily observed that these lines are much coarser than those in unirradiated copper and superficially, at least, are similar to those observed in  $\alpha$ -brass. In addition, copious amounts of cross slip are observed<sup>12)</sup>. This is readily observed in fig. 10. Cross slip is slip which is in the same slip direction as primary slip but in a different slip plane. If, for example, one labels the primary slip plane as the (111) plane, then the cross slip plane is the (111) plane. It has been verified that the strain markings do indeed occur on the primary system and on the cross slip system from geometrical considerations utilizing the method outlined by Barrett. Cross slip has never been found in pure annealed copper deformed at helium temperatures and at higher temperatures it was found only after extensive strain in the nonlinear portion of the stress-strain curve. On the other

hand, copious amounts of cross slip have been observed in the Lüders band of  $\alpha$ -brass. It might also be noted that the cross slip may be associated with slip on the latent system. It has been noted that relatively small amounts of cross slip are observed in samples whose tensile axis is near the center of the stereographic net,



Fig. 17. Micrographs of the slip lines in the Lüders band of an irradiated copper crystal shown in fig. 10 obtained with an electron microscope. Magnification 6000  $\times$ . Obtained through the co-operation of T. S. Noggle.

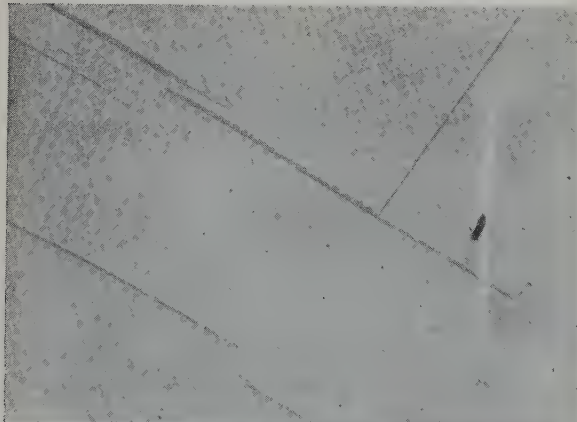


Fig. 18. Micrographs of slip lines in an irradiated copper crystal. Bombardment dose  $1 \times 10^{18}$ . Tensile axis near the center of the net. Field of view has an unusually large density of cross slip.

whereas those samples whose tensile axis is on the dodecahedral plane have extremely large amounts of cross slip.

The large step height of slip lines observed in the optical microscope has been verified by examination at magnifications up to 10 000  $\times$  in the electron microscope  $\dagger$ . Fig. 17 shows a photomicrograph obtained in the electron microscope. The sample and field of view are the same as those of fig. 10, which were obtained with the light microscope. It is clear that these lines are considerably different from those of unirradiated copper and that they bear a resemblance to slip lines in  $\alpha$ -brass. The step height seems to be about 1 micron. Fig. 18 is a photomicrograph of a slip line in a sample whose tensile axis is near the center of the net. In this sample cross slip can be seen infrequently.

### 3.4. STRESS-STRAIN CURVE FOLLOWING THE LÜDERS BAND

In the previous sections we have seen that irradiation dramatically changes the yield stress and associated phenomena. Following the com-

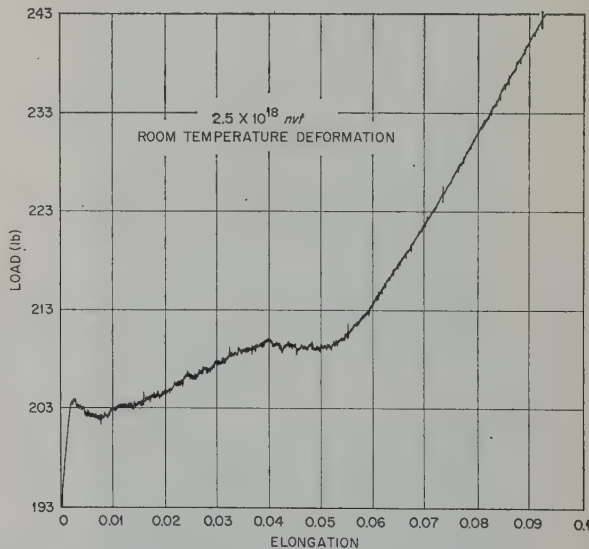


Fig. 19. Load-elongation curve of a copper crystal deformed at room temperature following exposure to  $2.5 \times 10^{18}$  neutrons/cm $^2$ . The sharp transition from Lüders band deformation to homogeneous deformation is typical and readily observable.

$\dagger$  The photomicrographs of figs. 17 and 18 were the work of T. S. Noggle and J. O. Stiegler.

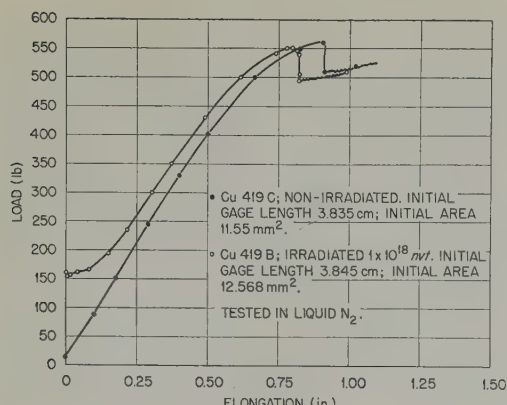


Fig. 20. Load-elongation curve of copper crystals of identical orientation obtained at 78° K. One crystal was irradiated for a dose of  $1 \times 10^{18}$  nvt and the other was retained in its initial condition.

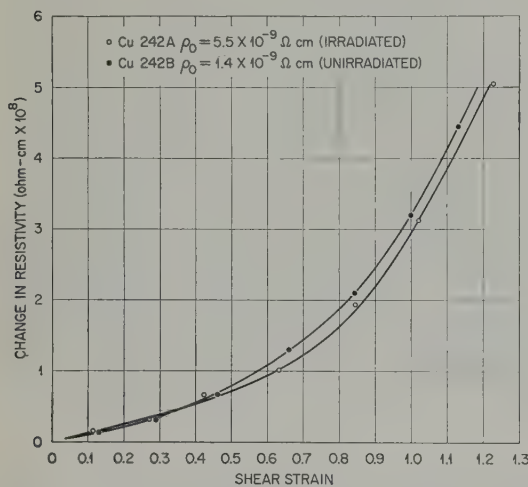


Fig. 21. The change in resistivity due to plastic deformation. Two samples of identical orientation, one of which was irradiated for a dose of  $2 \times 10^{18}$  neutrons/cm<sup>2</sup> (shear strain curves shown in fig. 13), were deformed in liquid helium, and the resistance measured as a function of strain without warming up. It can be seen that the neutron irradiation does not affect the deformation induced resistance.

pletion of deformation by the Lüders band the effects of neutron irradiation are less pronounced. Fig. 19 shows that the transition from the Lüders band to a more normal rate of work hardening seems to be a sharp one. The rate of work hardening after this transition point does not seem to be greatly affected by neutron bombardment at least for moderate doses<sup>13</sup>. This can be seen from figs. 12, 13, and 20. For

high doses the rate of work hardening seems to be somewhat smaller, as illustrated by fig. 11. It would thus seem that the neutron irradiation does not greatly affect the mechanism of work hardening. Measurements made on the electrical resistivity of deformed single crystals indicate that there is a one-to-one correspondence in irradiated and unirradiated crystals of the dislocation density as a function of strain. This is illustrated in fig. 21. Two crystals of the same orientation, one of which was irradiated to  $2 \times 10^{18}$  nvt, have been deformed at 4.2° K, and the electrical resistivity was measured as a function of strain. The stress-strain curves of these crystals are shown in fig. 12. Presumably, the resistivity is a measure of the defect concentration generated by the creation and motion of dislocations. Earlier experiments have shown that about half of this resistivity change can be attributed to point defects, probably vacancies, while the other half can be attributed to the generation of dislocations<sup>14</sup>. Since there is no a priori reason why the generation of one defect should occur at the expense of the other, the fact that the resistivity changes are the same in plastically deformed irradiated and unirradiated crystals implies that the dislocation density of crystals is unaffected by neutron irradiation.

Neutron irradiation does, however, strongly affect the stress-strain curve at the point where slip commences on the second slip system. In the case of the tensile deformation of face centered cubic metals, deformation proceeds on the (111) plane in a [110] direction.

Since there are four such planes, each of which have three [110] directions, slip will proceed only on that system which has the highest resolved shear stress. This system is called the primary slip system. As deformation proceeds, however, the constraints of the grips cause the tensile axis to rotate relative to the crystallographic axis. This effect eventually will cause the tensile axis to lie in the dodecahedral plane (the great circle in the stereographic net connecting poles of the (100) and (111) planes). At this point the resolved stress on a second slip system, called the latent system, becomes

equal to the primary system. In the case of high purity crystals slip then occurs simultaneously on both slip systems and the tensile axis of the crystals remains on the dodecahedral plane. This new mode of deformation, duplex slip, does not affect the rate of work hardening and in point of fact cannot be detected in the load-elongation or stress-strain curves. In the case of alloy crystals, however, the onset of duplex slip occurs in a different manner<sup>15</sup>. For reasons which are not understood, the latent system does not become active when the resolved shear stress is equal to that on the primary system but, rather, slip continues on the first system. The tensile axis thus continues to rotate and crosses over the dodecahedral plane (this phenomenon is generally referred to as *overshoot*). The latent plane then has a higher resolved shear stress than the primary plane. The extent of this overshoot and, thus, the degree to which the latent plane has hardened, increases with the content of the alloying elements. In contrast to the case for high purity metals, a change in slope is observed in the load-elongation curve upon the onset of duplex slip. This is a direct consequence of the

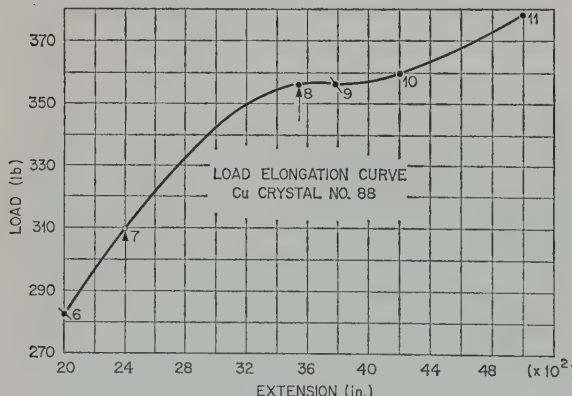


Fig. 22. The load-elongation curve of copper crystal No. 88 irradiated to  $1 \times 10^{18}$  neutrons/cm<sup>2</sup> and deformed at room temperature. At all numbered points the sample was metallographically examined, at points 6, 8, 9, 10 and 11 photomicrographs were obtained, at points 7 and 8 the sample was electrolytically polished to remove all slip lines following examination, and at points 6 and 9 Laue back reflection X-ray photographs were obtained.

fact that the latent plane is harder than the active plane. In the stress-strain curve there will, of course, be a discontinuity in stress at the strain where duplex slip occurs.

The load-elongation curve of neutron irradiated crystals shows an unmistakable change in slope at the point where the latent slip system becomes operative (see fig. 27), which results in a discontinuity in the stress-strain curve of neutron irradiated crystals<sup>16</sup>. From this standpoint the effect of neutron irradiation shows up in the same manner as the addition of an

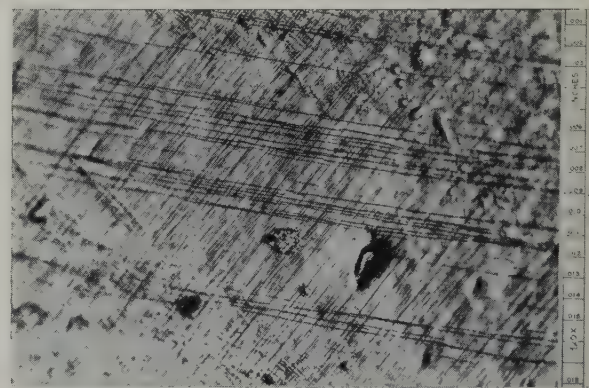


Fig. 23. Photomicrograph taken at point 8 of fig. 22. Bands of clustered slip lines of large step height from the latent system can be seen superimposed on the background of slip lines from the primary system.

Magnification 120 X.

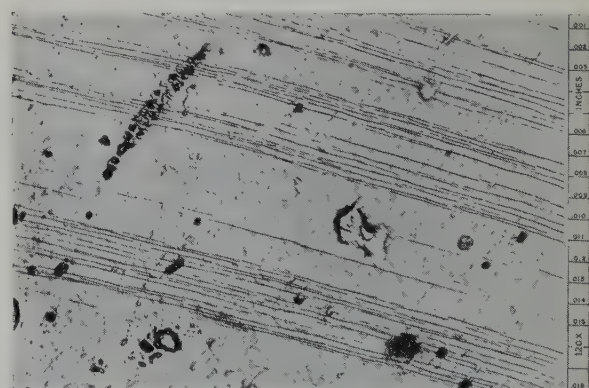


Fig. 24. Photomicrograph taken at point 9 of fig. 22. The slip lines seen in fig. 23 taken at point 8 have been removed by electrolytic polishing. Slip lines from the latent system predominate almost to the point of exclusion of slip lines from the primary system. Magnification 120 X.

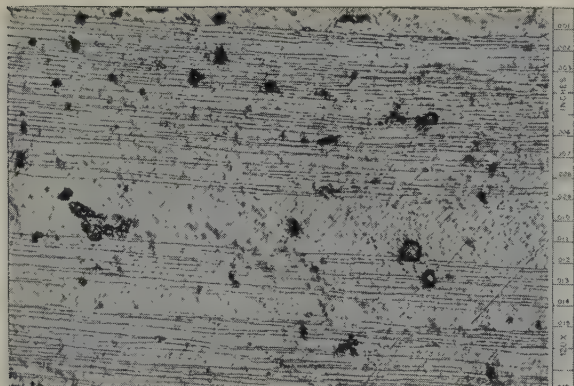


Fig. 25. Photomicrographs taken at point 10 of fig. 22. Slip lines from the latent system predominate almost to the point of exclusion of slip lines from the primary system. Magnification 120  $\times$ .

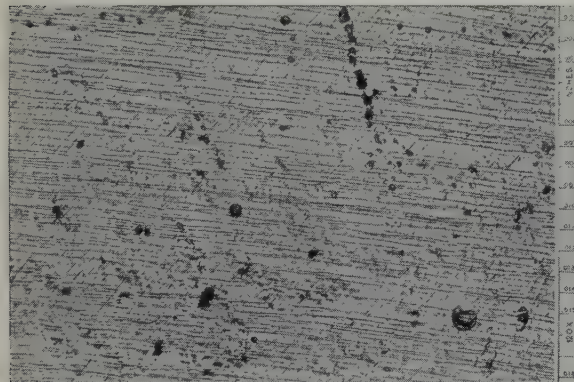


Fig. 26. Photomicrographs taken at point 11 of fig. 22. At this point the Lüders band associated with the latent slip system has filled up the crystal and a uniform density of slip lines, predominantly those of the latent slip system, is visible. Magnification 120  $\times$ .

alloying element<sup>17</sup>). The investigation of this point was done in some detail. The load-elongation curve of sample 88 is shown in fig. 22. The strain markings were examined at various points of the load-elongation curve. Photomicrographs were taken at points 6, 8, 9, 10, and 11 of fig. 22. Following examination of the strain markings, the samples were electrolytically polished to remove strain markings at points 7 and 8. Up to point 8 only one set of lines, the primary set, could be observed despite the fact that at point 6 the shear stress in the latent slip system exceeded that of the primary system. The strain markings at points 8, 9, 10, and 11 are shown in figs. 23, 24, 25, and 26,

respectively. The photomicrograph taken at point 8 shows the high density of slip lines from the primary system plus a few slip lines from the latent system. As has been noted earlier, the sample was polished at this point to remove all slip lines. As slip progresses beyond this point and in coincidence with the change in slope, figs. 24, 25, and 26 show that the strain markings are predominately in the latent slip system. It is worth noting that the photomicrographs show the clustering of slip bands characteristic of Lüders band formations upon the onset of slip on the latent system. A Lüders band has been observed on several samples with the onset of duplex slip. These photomicrographs thus demonstrate that the discontinuity in the load-elongation curve is associated with slip commencing on the latent system. The discontinuity associated with slip changing back to the primary system has also been observed. This is shown in fig. 27 where the discontinuities are plainly evident.

This phenomenon of overshooting has important consequences for the yield stress when

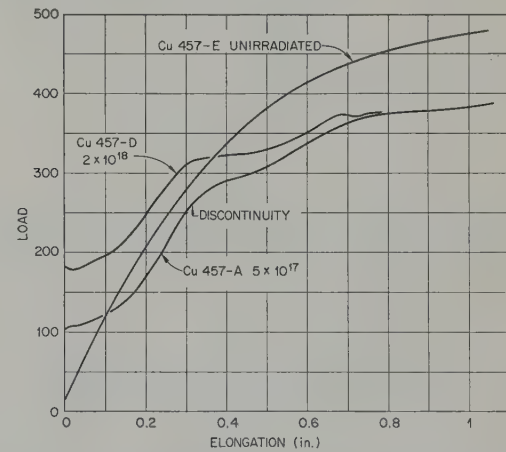


Fig. 27. Load-elongation curves of copper crystals deformed at 78° K following neutron bombardment. These curves show the discontinuities which arise from the onset of a second slip system. The first discontinuity near 0.30 in elongation is the result of slip changing from the primary system to the latent system. The second discontinuity near 0.7 in elongation is the result of slip changing from the latent system back to the primary system. It can be noted that an increase in dose results in a sharpening up of the discontinuity due to an increase in the Lüders band formation.

the tensile axis lies very near to the dodecahedral plane. In this case both the primary and conjugate slip systems have resolved shear stresses which are nearly the same. Both systems can become operative independently, and the interaction of the two with each other causes the yield stress to be greatly enhanced. For example, six samples of a crystal with an orientation on the dodecahedral plane were bombarded for a dose of  $1.5 \times 10^{19}$  nvt. Three of these initially deformed on one slip system and the yield stress was  $4.1 \text{ kg/mm}^2$ . The remaining three deformed initially by slip on the conjugate and primary systems with an average yield stress of  $7.1 \text{ kg/mm}^2$ . (The photomicrograph of fig. 10 is one of the three with the abnormally high yield stress.) These data

regions in the range between  $7^\circ \text{ K}$  and  $700^\circ \text{ K}$  where presumably different defects are moving or interacting with other defects. In addition to these, a fifth peak has been reported just below room temperature (about  $235^\circ \text{ K}$ ) †.

The influence of each of these annealing peaks on the radiation hardening would be of great value in understanding this phenomena. Studies of this type, while not complete, have been performed at Oak Ridge National Laboratory. Perhaps the most significant experiments in this regard were those performed in the Hole 12 cryostat of the Oak Ridge Graphite Reactor. In these experiments samples were tested in a tensile machine specially designed to permit the determination of the yield stress at very low temperatures in the confined space of the Hole

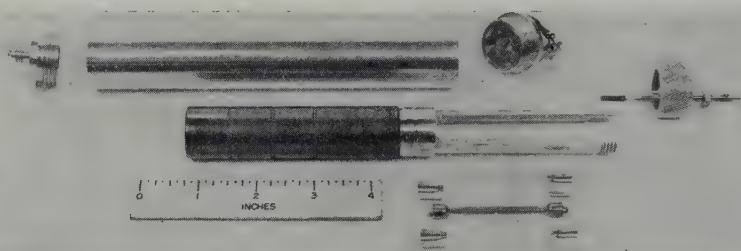


Fig. 28. The in-pile tensile machine. The load is applied with helium gas pressure on the graphite piston. The extension is measured with a differential transformer, the core being mounted on the piston assembly and the coils being mounted on the cylinder assembly.

thus show that the interaction of two slip systems will raise the yield stress significantly.

### 3.5. ANNEALING STUDIES

Extensive measurements of the annealing kinetics of reactor irradiated copper have been made utilizing radiation induced resistivity on samples bombarded as low as  $3.8^\circ \text{ K}$ <sup>18,19</sup>. These measurements show that about 5 % of the resistivity induced by the bombardment anneals out continuously in the range from  $7.2^\circ \text{ K}$  to  $30^\circ \text{ K}$ , from  $30^\circ \text{ K}$  to  $50^\circ \text{ K}$  about 40 % of the resistance anneals out, from  $50^\circ \text{ K}$  to  $550^\circ \text{ K}$  about 40 % anneals out in a rather uniform fashion, and finally in the region from  $550^\circ \text{ K}$  to  $700^\circ \text{ K}$  the balance of the resistivity recovers. There are thus four distinct annealing

12 cryostat<sup>20</sup>). The load was applied hydraulically using helium as the fluid. The piston was constructed of graphite and the cylinder of 24 ST aluminum. Lubrication was provided by adjusting the clearance between these two components so that the helium gas acted as the lubricant after the principle of the Kapitza expansion engine. The extension was measured by means of a differential transformer. An exploded photograph of the tensile machine is shown in fig. 28.

The experiment was performed by determining the yield stress at  $25^\circ \text{ K}$  of a copper

† Recent experiments at ORNL by the authors suggest that a diffusion activated process which may or may not affect the resistance is operative in this temperature range.

TABLE 1  
Effect of low temperature annealing on the flow stress of high purity copper

Sample No.		
Cu 316	Cu 425-A	
Yield stress (kg/mm <sup>2</sup> )		
0.59	0.5926	Yield point at 25° K before bombardment
2.48	2.168	Yield point at 25° K after bombardment
2.39	2.085	Yield point at 25° K after anneal at 80° K
1.80		Yield point at 25° K after anneal at 300° K

Bombardment temperature — 20° K  
Dose =  $1.6 \times 10^{17}$  nvt

crystal utilizing the tensile machine described above in the Hole 12 cryostat. The samples were then bombarded in a reactor for three days at a temperature of 15° K (a total dose of  $1.6 \times 10^{17}$  n/cm<sup>2</sup>) and the critical shear stress was again determined. Following this determination of the flow stress the cryostat was warmed to 78° K so that the crystal was heated above the temperature at which a large fraction of the resistivity recovers. The yield stress was then redetermined after the sample had been cooled to 20° K. The results of these experiments are shown in table 1.

A similar experiment was performed utilizing a beryllium-doped copper sample. It has been found that the presence of this small amount of beryllium prevents the electrical resistivity from annealing until temperatures of 130° K are reached<sup>21</sup>. This isothermal annealing curve of Be doped Cu is shown in fig. 29. Samples of 1% beryllium in copper were then bombarded

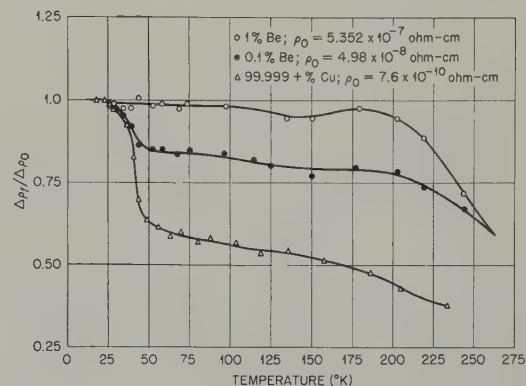


Fig. 29. Isothermal annealing of high purity copper and of beryllium doped copper (Blewitt, Coltman, Klabunde, and Noggle<sup>21</sup>). (Courtesy of Journal of Applied Physics.)

at 15° K and withdrawn in a bath of liquid nitrogen. The yield stress of these samples was then determined in a bath of liquid nitrogen utilizing an Instron tensile machine without allowing the sample to warm up. The samples

TABLE 2  
Effect of room temperature annealing on the flow stress of high purity copper

Sample No.			
Cu 190	135	1 % Be †	
113	14	14	Bombardment temperature (°K)
$5 \times 10^{17}$	$8 \times 10^{17}$	$8 \times 10^{17}$	Dose
0.2	0.22	0.83	Yield stress at 78° K before bombardment (kg/mm <sup>2</sup> )
2.12	2.69	2.45	Yield stress at 78° K after bombardment (kg/mm <sup>2</sup> )
		2.37	Yield stress at 78° K after anneal at 180° K (kg/mm <sup>2</sup> )
		2.30	Yield stress at 78° K after anneal at 233° K (kg/mm <sup>2</sup> )
1.8	2.28	2.18	Yield stress at 78° K after anneal at 300° K (kg/mm <sup>2</sup> )

† Due to uncertainty in orientation the absolute magnitude may be in error by  $\pm 10\%$ .

TABLE 3

Effect of bombardment temperature on the yield stress of high purity copper

Sample No.	C.S.S. (kg/mm <sup>2</sup> )	
	300° K	78° K
Samples bombarded at 14° K, annealed at room temperature		
Cu 377-D	1.31	1.89
Cu 377-E	1.28	1.97
Cu 377-F	1.08	1.55
Cu 378-D	0.93	1.44
Cu 378-E	1.19	1.88
Cu 378-F	1.16	1.84
Samples bombarded at 300° K, annealed at room temperature		
Cu 377-A	1.09	1.37
Cu 377-B	0.92	1.19
Cu 377-C	0.971	1.21
Cu 378-B	0.88	1.11
Cu 378-C	0.78	1.01

were then annealed at various temperatures and then reimmersed in liquid nitrogen, and the flow stress was again measured. The results of these experiments are shown in table 2.

The data of both table 1 and table 2 clearly show that the annealing associated with the annealing peak at 30–50° K had a negligible influence on the hardening. In the case of high purity copper, however, the evidence suggests that a low temperature bombardment will increase the shear stress more than will an equivalent neutron dose at higher temperatures. This was shown by bombarding two sets of samples to the same dose in Hole 12, one set being kept at 14° K during the bombardment and the other at 320° K. The yield stress samples were measured in both cases at room temperature in the Instron tensile machine. The results are shown in table 3.

Measurements on the effect of annealing temperatures in the range from 80° K to 300° K on the yield stress have also been measured. Samples were bombarded in the graphite reactor at 14° K in Hole 12 and removed in a bath of liquid nitrogen. Measurements of the yield stress were then made without warm-up and after

warming to room temperature. The results, which are shown in table 1, indicate that about 20 % of the flow stress is recovered by the room temperature anneal. A definitive experiment has not been performed so that this annealing may be attributable to either the range of annealing from 50° K to 230° K or to that usually attributed to vacancy migration (230° K to 270° K). It should also be noted that annealing in 80–300° K does not apparently effect the temperature dependence of the flow stress. A sample was bombarded at 14° K and the yield stress measured at 4.2° K and at 78° K following a long anneal at 78° K. The yield stresses of 3.6 and 2.7 kg/mm<sup>2</sup> are in good agreement with samples bombarded at 300° K.

Annealing experiments conducted in the region above room temperature<sup>22)</sup> show that the remaining radiation hardness is annealed in

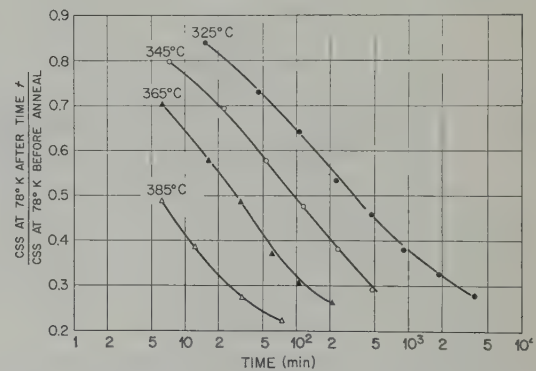


Fig. 30. Isothermal annealing of the yield stress of copper crystals irradiated to a dose of  $1 \times 10^{19}$  neutrons/cm<sup>2</sup>. Deformation temperature 78° K.

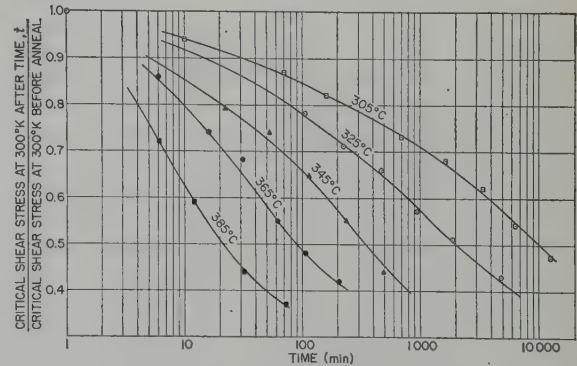


Fig. 31. Isothermal annealing of the yield stress of copper crystals irradiated to a dose of  $1 \times 10^{19}$  neutrons/cm<sup>2</sup>.

the region from 300° C to 400° C. Samples bombarded in the LITR reactor to a flux of  $10^{19}$  were utilized to make these measurements. Isothermal annealing was done in a salt bath at 305, 325, 345, 365, and 385° C. The critical shear stress was measured at both 78° K and 300° K. The results are shown in figs. 30 and 31. The apparent activation energy can be determined from the isochronal annealing curves. The rate equation may be written as follows:

$$\int_{n_0}^n \frac{dn}{n^\alpha} = A e^{-\varepsilon/kT} t \quad (6)$$

where  $n$  is the number of defects,  $\alpha$  is the order of the reaction,  $A$  is a constant related to the jump frequency,  $\varepsilon$  is the activation energy,  $k$  is Boltzman's constant,  $T$  is the absolute temperature, and  $t$  is the time of anneal at temperature  $T$ . If all of the samples are bombarded simultaneously, as these were, then the number of defects introduced will be the same. Under the assumption that the flow stress  $\sigma$  is a single valued function of the number of defects, the rate equation can be written as

$$c \int_{n_0}^n \frac{dn}{n^\alpha} = e^{\varepsilon/kT_i} t_i = c'' \quad (7)$$

for the case where the sample has been annealed to a flow stress  $\sigma_i$  (a given value of  $\sigma_i$  implies that the number of defects has been reduced to the same value  $n_i$  regardless of the annealing path).

Or,  $\ln c'' = \ln t_i - \varepsilon/kT_i \quad (8)$

for any heat treatment which anneals the same amount of flow stress. The activation energy if unique will then be given by slope of the line relating the log of the relaxation time  $t$  to the reciprocal of the absolute temperature. A plot of this type is shown in fig. 32. It can be seen that reasonably good straight lines can be drawn through five points with an activation energy ranging from 2.0 to 2.5 eV  $\dagger$ . It is not, however, clear that this is a uniquely activated

$\dagger$  It may be advisable to disregard the more uncertain data pertaining to the 20 % recovery and 60 % recovery, in which case the spread in activation energies would be reduced from 2.1 to 2.3 eV.

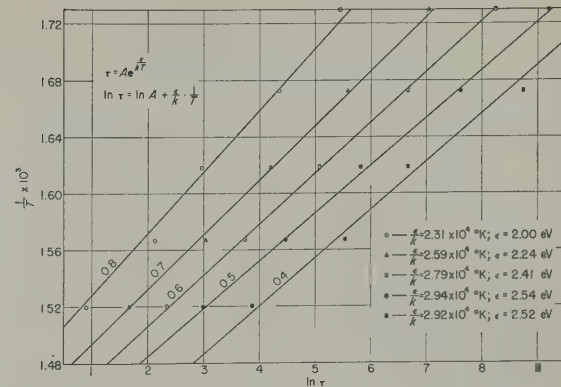


Fig. 32. Phenomenological determination of the activation energy for the recovery of radiation hardness in copper. The  $\ln$  of the relaxation time  $\tau$  or the time required for the recovery 0.8, 0.7, 0.6, 0.5, and 0.4 of the yield stress (measured at room temperature) is plotted as a function of the reciprocal of the absolute temperature. The apparent activation energy is proportional to the slope of the line.

process. The fact that the apparent activation energy increases somewhat as the fraction recovered increases would seem to suggest a spectrum of activation energies. A unique activation energy would also require that the isothermal annealing curves plotted in figs. 30 and 31 should be parallel to each other since

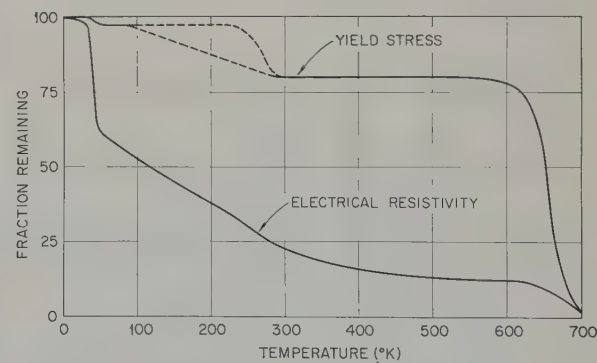


Fig. 33. Schematic diagram of the effect of temperature on the critical shear stress and on the electrical resistivity. In both curves the data are taken at a reference temperature (yield stress 25° K, resistivity 4° K) so that these curves represent an annealing phenomenon with any temperature dependence eliminated. The shape of the yield stress curve in the region between 80° K and 290° K has not been determined. It would be expected, however, that this curve would fall between the two dotted lines.

eq. (8) can be written as:

$$\frac{\varepsilon}{k} \left( \frac{1}{T_i} - \frac{1}{T_{i+1}} \right) = \ln t_i - \ln t_{i+1} \quad (9)$$

at the same flow stress  $\sigma = \sigma(n_i)$ . Since

$$\frac{\varepsilon}{k} \left( \frac{1}{T_i} - \frac{1}{T_{i+1}} \right)$$

is a constant for any two isothermal annealing curves, it can be seen that the time increment between any two curves must be a constant. It can be seen from figs. 30 and 31 that this is not the case. It can, therefore, be concluded that the activation energy is probably not unique. The apparent values of 2.1 to 2.3 eV may require modification to some extent when the annealing kinetics are more fully understood.

It is also of interest to note that in the data of figs. 30 and 31 annealing the sample in the 300 to 400° C range reduces the temperature dependence of the yield stress, the yield stress at 78° K being smaller after annealing than the yield stress observed in an unannealed sample with the same room temperature critical shear stress. It is not clear, however, whether the  $T^{\frac{1}{2}}$  dependence or the coefficient is changed by the anneal. The results of these sections can well be summarized in fig. 33 where the annealing spectra of the hardness and of the electrical resistivity are plotted.

### 3.6. PHYSICAL PROPERTY CHANGES ASSOCIATED WITH RADIATION HARDENING

The experiments discussed in the previous section make it clear that 80 % of the radiation hardness is retained until temperatures in the vicinity of 350° C are reached. Measurements of the electrical resistivity, density, and X-ray line shapes have been measured following room temperature reactor bombardment. Presumably, the changes in these properties are associated with the defects that cause radiation hardening. Measurements of the electrical resistivity were made by the IR drop method on samples bombarded at room temperature with the resistance being measured at 4.2° K. Measurements of this kind were made with neutron doses ranging from  $5 \times 10^{17}$  to  $8 \times 10^{19}$  n/cm<sup>2</sup>. These results are shown in fig. 34 where the log of resistance

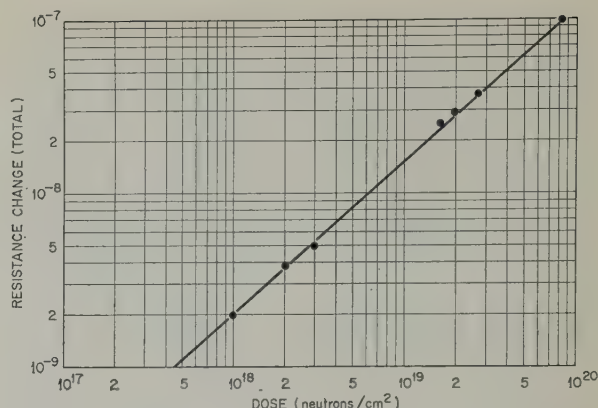


Fig. 34. Effect of room temperature bombardment on the electrical resistivity of copper single crystals. The change in resistivity is plotted as a function of the neutron dose (nvt). About  $\frac{1}{3}$  of this change is associated with transmutations.

TABLE 4  
The change in resistivity and flow stress in reactor irradiated copper

Change in resistivity (ohm cm $\times 10^{-9}$ )	Flow stress (kg/mm <sup>2</sup> )		Dose (neutrons/cm <sup>2</sup> )
	300° K	78° K	
2.0	1.8	2.8	$1 \times 10^{18}$
3.8	2.1	3.6	$2 \times 10^{18}$
5	2.3	4	$3 \times 10^{18}$
25	4.0	7.2	$1.6 \times 10^{19}$
36	4.7	8.3	$2.5 \times 10^{19}$
100	7.2	12	$8 \times 10^{19}$

is plotted against the log of the dose. It is significant that the slope of the line is unity within experimental accuracy showing that the resistance and presumably the number of defects contributing to the hardness is directly proportional to the dose  $\dagger$ . It can be seen that there is little indication of an exponential component, so it can be concluded that a saturation effect has not become appreciable at doses up to  $8 \times 10^{19}$ . Table 4 illustrates, especially for small doses, that extremely large changes in the yield stress can occur with relatively small changes in the electrical resistivity.

$\dagger$  While the probable error is relatively small, it is believed that systematic errors such as bombardment temperature, slow flux, fast flux, impurity content, etc., account for the slope of the line in fig. 34 not being exactly unity.

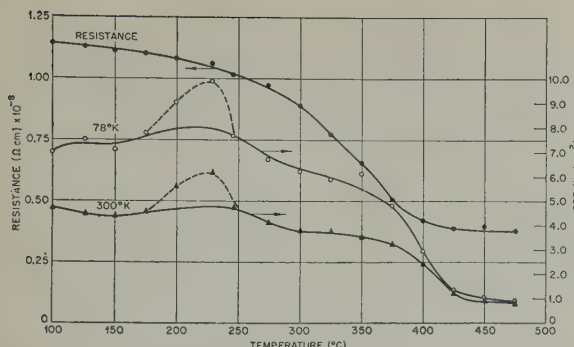


Fig. 35. Isochronal annealing curves of the electrical resistance and yield stress of a copper crystal irradiated to  $9 \times 10^{18}$  nvt. The apparent increase in shear stress in the region from  $175^\circ\text{C}$  to  $250^\circ\text{C}$  is not believed to be significant.

Annealing experiments have also been undertaken. In these studies the critical shear stress, as well as the electrical resistivity, has been measured. The purpose of this particular study was to determine the change in resistivity associated with the radiation hardness; consequently, isochronal type anneals were made. Measurements of the electrical resistivity and of the critical shear stress were made following ten minute pulse anneals at temperature intervals of about  $25^\circ\text{C}$  in the range of temperature from  $100^\circ\text{C}$  to  $500^\circ\text{C}$ . These results are shown in fig. 35. There is a small decrease in resistivity in the region from  $100^\circ\text{C}$  to  $275^\circ\text{C}$  which apparently does not affect the flow stress, but it is apparent that a large drop in resistivity is associated with the recovery of the hardness. The remaining resistivity probably is the result of transmutations. Thus, in fig. 35 about 75 % of the resistivity should be associated with the flow stress †.

Studies of the X-ray diffraction line shape were made on samples irradiated for  $3 \times 10^{19}$  nvt ‡. A double crystal spectrometer was utilized using mica as the monochromator. This enabled the  $\text{K}\alpha$  doublet of copper to be resolved, and

† Fig. 35 represents the work on one crystal. The increase in yield stress in the  $200$  to  $250^\circ\text{C}$  range has not been verified in several instances whereas the decrease in yield stress has been verified many times.

‡ This work was done in conjunction with F. A. Sherrill.

the  $\text{K}\alpha$  copper line was then utilized as the source of radiation. The detector was a proportional counter designed at ORNL which permitted the measurements to be made with a very low background.

A single crystal plate whose surface was within a few degrees of the (111) plane was utilized as the sample. Half of it was irradiated in the LITR to a dose of  $3 \times 10^{19}$  nvt. Rocking curves were then measured of each portion of the crystal under identical conditions. The results are shown in fig. 36. It can be seen that, with the exception of the tail, there is no change in line shape and, of particular importance, the half breadth is unchanged by irradiation (the half breadth of 4.4 minutes is relatively small for a metal crystal). There is evidence that the increase in the tail is the result of only partial discrimination by the counter of the residual radioactivity from the irradiated sample.

#### 4. Discussion

The previous sections have clearly shown that substantial changes in the mechanical properties of copper crystals occur as the result of neutron bombardment. It is quite clear that the defects produced by the bombardment must interact with the dislocations to produce these

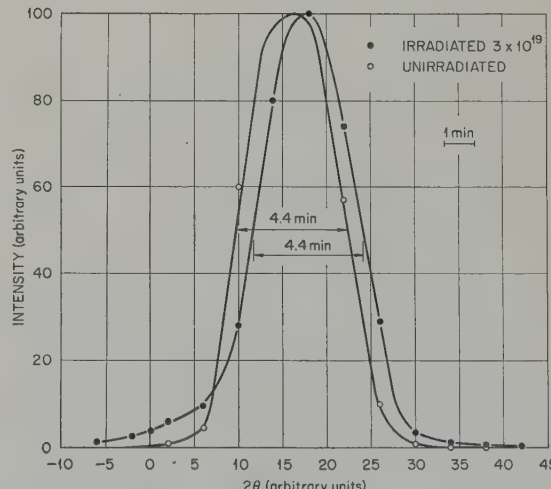


Fig. 36. Rocking curves of the (111) reflection of a copper crystal before irradiation and after a neutron dose of  $3 \times 10^{19}$ . The values of  $2\theta$  are given in arbitrary units, and the apparent shift in  $2\theta$  is not significant.

changes. Two types of interaction may occur. Some of the radiation induced defects may lie in the vicinity of the Frank-Read generators (dislocation sources) acting as barriers to their operations (source hardening). The defects may form a Cottrell atmosphere, they may lie in the region of the stacking faults; or they may form clusters on the dislocation line. Instead of this type of interaction, however, the radiation induced defects may impede the motion of the dislocation after they have been formed (friction hardening). The barriers to the motion of the dislocations after they have formed may be clusters of vacancies or interstitials, the debris from a thermal spike, or a small recrystallized region. In order to understand the basic mechanism of radiation hardening, it is imperative to decide which of these two types of interaction results in the hardening.

Unfortunately, our present state of knowledge in the field of plastic deformation does not permit a definitive experiment to be performed in order to distinguish between these two alternatives. For example, the temperature dependence of the yield stress, the hardening of the slip system, the formation of an upper yield stress and Lüders band propagation, and the mechanism of cross slip are not sufficiently understood so that these phenomena can be utilized to distinguish between source and friction hardening. There are, however, a few clues available in the data presented in this paper, and these will now be discussed.

First of all, the results of the flow stress measurements which show that

$$\sigma(\phi, T) = g(\phi)f(T),$$

make it improbable that radiation hardening is a mixture of friction and source hardening. The fact that the above equation exists means that  $g(\phi)$  and  $f(T)$  must be the same for both types of hardening or that the contribution of each of these mechanisms must remain independent of the flux if the flow stress  $\sigma$  is assumed to be the result of a joint contribution of source and friction hardening. Since it is rather unlikely that either of these conditions

exist, it is perhaps safe to draw the conclusion that either source of friction hardening, but not both, is responsible for radiation hardening for doses ranging from  $10^{17}$  to  $10^{20}$  n/cm<sup>2</sup>.

Now the problem remains as to which of these mechanisms is responsible for radiation hardening. The substantial temperature dependence which for temperatures greater than 30° K can be written as  $f(T) = h(T^{\frac{1}{2}})$  does not help in resolving the dilemma since either mechanism can account for this temperature dependence. It does, however, make the specific mechanism of source hardening arising from vacancy clusters in the dislocation line, suggested by Friedel<sup>23</sup>, most unlikely as this model predicts a much smaller temperature dependence.

On the other hand, the flux dependence  $g(\phi) = j(\phi^{\frac{1}{2}})$  raises a serious objection to the concept of friction hardening. The objection arises from the fact that plastic deformation is a slip process which occurs on a plane. If, then, the impedance to slip is purely a result of a random distribution of barriers on this plane, the dependence on the flux should be a  $\phi^{\frac{1}{2}}$  rather than  $\phi^{\frac{1}{3}}$  term †. This objection is supported by the resistance data which shows that for fluxes to  $8 \times 10^{19}$  n/cm<sup>2</sup> the number of defects is proportional to the neutron flux. This result then indicates that the function  $\phi^{\frac{1}{2}}$  is indeed a fundamental relationship. It would thus appear difficult to rationalize these results with the lattice friction scheme. It should be noted, however, that this evidence supports the source hardening scheme only in a negative sense.

The very large slip steps observed in the electron microscope would also seem to offer support to the source hardening scheme since an avalanche of dislocations would be expected once the stress had become large enough to overcome the obstacles to dislocation generation. While it may be possible to concoct a

† The  $\phi^{\frac{1}{2}}$  dependence is discussed in some detail by D. K. Holmes (ORNL-2413, 1957) and A. K. Seeger (ref. 6). The experimental data to which reference was made in these discussions were a limited version of those shown in fig. 3.

model on the friction hardening scheme to account for the large slip step, the model must, of necessity, be cumbersome and hence less satisfying than that required for source hardening.

An interesting experiment by F. W. Young † also supports the concept of source hardening. A single crystal plate of copper was irradiated and deformed by bending. The application of the bending stress was performed in a very careful manner so that the yield stress was just barely exceeded at the surface. Since the bending stress diminishes to zero as one approaches the center line of the plate, the dislocations should not travel very far in the lattice friction picture as sufficient stress will not be available in the interior of the crystal to enable the dislocation line to overcome the randomly distributed barriers. On the other hand, in the source hardening picture a generator on the surface would have sufficient stress to become operative, and the force required to keep dislocations moving would be very small so that large step heights should be observed in the source hardening scheme. The results of the experiment showed slip lines of long length and of large step height, thus supporting the source hardening scheme.

It would seem that the experiment of measuring the yield stress following bombardment at 25° K and after warm up to 80° K would be a critical experiment to distinguish between these two models. If one assumes that some form of defect migration occurs at 30° K to 50° K then one should expect the yield stress to increase after the anneal if the source hardening picture were utilized, since the mobility of the defect would enable more defects to reach the dislocation. On the other hand, the yield stress would be expected to decrease if the lattice friction picture were utilized, since the mobility of the defect would result in an annihilation of some of the barriers to the motion of the dislocation lines. The results as we have seen have shown that the large annealing peak

† Private communication (1959) from F. W. Young, Jr., Solid State Division, ORNL.

has not appreciably affected the yield stress ‡.

It is somewhat difficult to rationalize this experiment with either picture. The source hardening picture requires that some of the defects (due to the formation of crowdion or to a focusing effect) travel large distances to the vicinity of the dislocation sources at the low bombardment temperatures. There is, indeed, good evidence that defects do interact with dislocation lines at bombardment temperatures of 20° K from the fact that the logarithmic decrement and the elastic constants are changed by bombardment at 20° K. There is also evidence that defects are formed near dislocations, probably the result of a focusing effect, from the fact that the radiation induced resistivity is enhanced in a severely deformed crystal. On the other hand, it is also observed that the changes in decrement and elastic constants greatly increase during the 30 to 50° K bombardment ‡‡.

The results of this experiment also raise serious objections to the lattice friction scheme. It is difficult to conceive of barriers formed by bombardment which would not be changed by the migration of a radiation induced defect. The low temperature shear-stress measurements while extremely important are very difficult to interpret in a positive sense.

In summary, then, although the evidence is by no means conclusive, radiation is most probably the result of an interaction of radiation defects with the dislocation sources. Perhaps the most satisfying conclusion to be derived from this work is the fact that radiation hardening appears to be completely analogous to solution hardening. For example, one finds a one-to-one correspondence between the deformation characteristics of  $\alpha$ -brass and samples

‡ It is interesting to note that if the assumption is made that interstitials become mobile and are annihilated at vacant lattice sites, then the low temperature yield stress experiment requires that defects other than single vacancies and single interstitials must be present on bombardment at 20° K.

‡‡ A detailed discussion of the low temperature experiments becomes considerably involved and will be postponed to a subsequent publication.

which have been reactor irradiated. The stress-strain curve with the Lüders band, the fact that the latent plane hardens faster than the active plane (overshoot), the temperature dependence of the flow stress, the high step height of the slip bands, and the appearance of cross slip are characteristic of deformed  $\alpha$ -brass and of neutron irradiated copper. It thus appears that if an understanding of the basic mechanisms of hardening is gained for either of these materials both will be understood.

It might be worth pointing out that radiation hardness is not analogous to work hardening. This is immediately obvious when the stress-strain curve, the temperature dependence of the flow stress, and the slip lines are considered. It is also significant that no recrystallization is observed on annealing the radiation hardness. It can be argued, however, that dislocation loops may form in neutron irradiated copper from the condensation of vacancies. The fact that the radiation hardening occurs at temperatures as low as 25° K and that a much higher temperature would be required for vacancy migration and coagulation raises a serious objection to a theory attributing the major source of hardening to dislocation loops formed from condensed vacancies.

### Acknowledgement

The authors are very pleased to acknowledge the helpful discussions with D. K. Holmes, J. Diehl, and C. E. Klabunde. They are also appreciative of the encouragement and interest shown by D. S. Billington.

### References

- 1) Among the numerous reviews are the following: D. S. Billington and J. H. Crawford, Jr., *Radiation Damage in Solids* (to be published by Princeton University Press, Princeton, New Jersey)
- 2) F. Seitz and J. S. Koehler, *Solid State Physics* (edited by F. Seitz and D. Turnbull), Vol. 2 (Academic Press, New York, 1956) p. 305
- 3) J. G. Dienes and G. H. Vineyard, *Radiation Effects in Solids* (Interscience Press, New York, 1957)
- 4) H. Brooks, USAED Document, TID-10033 (1950)
- 5) S. Siegel, *Phys. Rev.* **75** (1949) 1823
- 6) T. H. Blewitt, R. R. Coltman, C. E. Klabunde and T. S. Noggle, *J. Appl. Phys.* **28** (1957) 639
- 7) T. H. Blewitt, R. R. Coltman, D. K. Holmes and T. S. Noggle, *Creep and Recovery* (ASM, Cleveland, Ohio, 1957) p. 84
- 8) F. Seitz and J. S. Koehler, *Solid State Physics* (edited by F. Seitz and D. Turnbull), Vol. 2 (Academic Press, New York, 1956) p. 305
- 9) A. K. Seeger, Proc. U. N. Intern. Conf. of Peaceful Uses of Atomic Energy, 2nd, Geneva 1958, **6** (1959) 250
- 10) T. H. Blewitt, *Phys. Rev.* **91** (1953) 1115
- 11) T. H. Blewitt, R. R. Coltman and J. K. Redman, *J. Appl. Phys.* **28** (1957) 651
- 12) T. H. Blewitt and R. R. Coltman, AECD-3095; NSAS: 3260 (1951)
- 13) T. H. Blewitt and R. R. Coltman, *Phys. Rev.* **82** (1951) 769(A)
- 14) T. H. Blewitt and R. R. Coltman (reported by G. Kinchin and R. Pease), *Progress in Physics*, Vol. 18, 1 (1955)
- 15) R. E. Jamison and T. H. Blewitt, *Phys. Rev.* **91** (1953) 237(A)
- 16) D. K. Holmes, J. K. Redman, T. H. Blewitt and R. R. Coltman, *Bull. Am. Phys. Soc.* (II) **1** (1956) 130
- 17) T. H. Blewitt, R. R. Coltman and J. K. Redman, *Defects in Crystalline Solids-Report of 1954 Bristol Conference* (The Physical Society, London, 1955) p. 369
- 18) E. Schmid and W. Boas, *Plasticity of Crystals* (F. A. Hughes & Co., Ltd., London, 1950)
- 19) R. E. Jamison and T. H. Blewitt, *Phys. Rev.* **86** (1952) 641(A)
- 20) V. Goler and G. Sachs, *Z. Physik* **55** (1929) 581
- 21) T. H. Blewitt, R. R. Coltman, D. K. Holmes and T. S. Noggle, *Creep and Recovery* (ASM, Cleveland, Ohio, 1957) p. 84
- 22) T. H. Blewitt, R. R. Coltman, C. E. Klabunde, J. K. Redman and J. Diehl, *Bull. Am. Phys. Soc.* (II) **4**(3) (1959) 135
- 23) R. R. Coltman, T. H. Blewitt and T. S. Noggle, *Rev. Sci. Instr.* **28** (1957) 375
- 24) T. H. Blewitt, R. R. Coltman, C. E. Klabunde and T. S. Noggle, *J. Appl. Phys.* **28** (1957) 639
- 25) J. K. Redman, R. R. Coltman and T. H. Blewitt, *Phys. Rev.* **91** (1953) 448(A)
- 26) P. Coulomb and J. Friedel, *Dislocations and Mechanical Properties of Crystals* (edited by J. C. Fisher, W. G. Johnston, R. Thomson and T. Vreeland, Jr.) (John Wiley & Sons, Inc., New York, 1957) Sec. VIII, p. 555

ETUDE STRUCTURALE DU BERYLLIUM  
PAR MICROGRAPHIE ET MICRODIFFRACTION ELECTRONIQUES SUR COUPES MINCES

A. SAULNIER

Service des Recherches de la Cie. Péchiney, Chambéry, France

Reçu le 5 avril 1960

Une technique simple et rapide permet d'obtenir des coupes minces de beryllium, directement observables dans le microscope électronique. Elle est utilisée à la comparaison des structures à l'état écroui et à l'état recuit, de tôles minces de beryllium obtenues par filage et laminage d'une billette coulée ou par métallurgie des poudres. Des différences importantes dans la répartition des dislocations à l'état écroui, ont été relevées. Le comportement au cours de recuits à des températures comprises entre 800 et 1000° C, dépend lui aussi du mode d'élaboration et du taux d'écrouissage, les tôles pouvant, soit recristalliser franchement, soit éliminer progressivement leurs dislocations en accompagnant cette élimination de migrations lentes des joints du grain d'écrouissage.

La répartition de l'oxyde dans le métal fritté est aisément identifiable sur ces mêmes coupes, par micrographie et microdiffraction électroniques. Elle peut être déterminée également par extraction à l'aide de répliques de carbone.

A simple and direct technique has been developed for making thin sections of beryllium which can be directly observed in an electron microscope. It is used for comparing the structure, both in the cold-worked and the annealed conditions, of thin beryllium sheets made by drawing and rolling either cast billets, or billets produced by powder metallurgy. Significant differences were observed in the distribution of dislocations in the two cases. The behaviour of the metal during annealing at temperature in the range 800-1000° C also depends on the mode of preparation of the metal and on the degree of deformation; the

sheets either recrystallize in a straightforward manner, or else dislocations are eliminated gradually with simultaneous slow movement of grain boundaries already present in the deformed structure.

The distribution of oxide in the sintered metal can readily be recognized by electron micrography or microdiffraction of thin sections. Alternatively, the distribution can be determined by an extraction method with the aid of carbon replicas.

Mit einer einfachen und raschen Methode lassen sich dünne Schnitte von Beryllium herstellen, die unmittelbar im Elektronenmikroskop betrachtet werden können. Diese Methode wird für einen Vergleich der Gefüge im kaltverformten und geglühten Zustand herangezogen. Die zu verwendenden dünnen Beryllium Bleche werden durch Auswalzen eines gegossenen Blocks oder auf pulvermetallurgischem Wege angefertigt. Wichtige Unterschiede in der Verteilung der Versetzungen beim kaltverformten Material sind herausgestellt worden. Das Verhalten während der Glühungen zwischen 800 und 1000° C hängt von der Art der Vorbehandlung und von dem Verformungsgrad ab. Die Bleche können entweder rekristallisieren oder aber es können in zunehmendem Masse Versetzungen aufgehoben werden, was von einer langsamen Wanderung der Grenzen verformter Körner begleitet ist.

Die Verteilung der Oxyde im gesinterten Metall ist in den gleichen Schnitten ebenfalls durch Elektronen-Mikroskopie und Elektronenbeugung festzustellen. Sie kann ebenso gut mit Hilfe eines Kohleabdrucks ermittelt werden.

Certains attribuent cette fragilité à une propriété intrinsèque du métal, cependant que d'autres la relient à la présence d'impuretés. De même, la constatation a bien été faite que la résistance à la rupture et les allongements augmentent lorsque la grosseur du grain

## 1. Introduction

La fragilité et les mécanismes de rupture du beryllium posent aux laboratoires métallurgiques des énigmes que, ni les essais technologiques, ni les méthodes analytiques, ni les études de texture n'ont pu résoudre jusqu'à présent.

diminué mais on ignore encore à peu près complètement les propriétés des dislocations des réseaux hexagonaux et les modes d'interaction qui conduisent à l'initiation des critiques. Les phénomènes de restauration, recristallisation et grossissement du grain qui ne sont pas complètement élucidés pour les métaux anciens, sont pour autant dire inconnus dans le cas du beryllium. Il n'existe enfin que peu de données précises sur le mode de répartition de l'oxyde dans les produits élaborés par frittage bien que ce facteur fondamental régisse l'inhibition du grossissement du grain et, probablement, la modification des caractéristiques par irradiation.

Ainsi se trouvent brièvement soulignés les insuffisances de nos connaissances de base et les problèmes qui doivent être approfondis si l'on veut déterminer les raisons de la fragilité du beryllium et savoir en définitive s'il est possible ou non d'y remédier. Après l'échec des études métallurgiques classiques, il convient désormais de faire appel à cet effet aux techniques métallographiques les plus évoluées, à celle surtout de l'examen direct de coupes métalliques minces dans le microscope électronique qui a remporté, dans d'autres domaines, au cours des trois dernières années d'incontestables succès.

## 2. Méthode d'amincissement

Les premiers essais d'observation directe de coupes minces de beryllium, ont été effectués par Baird, Hartree et Phillips<sup>1</sup>). La méthode générale d'amincissement que nous avons eu, de notre côté, l'occasion de développer, s'applique sans difficulté au beryllium<sup>2</sup>). Elle est commode, rapide et présente l'avantage de ne pas faire intervenir d'écrouissage parasite lorsque les échantillons ont été préalablement laminés à quelques centièmes de millimètre et traités thermiquement à cette épaisseur. Elle est désormais suffisamment connue de l'ensemble des chercheurs spécialisés pour qu'il soit inutile d'y revenir en détail.

Le point de départ est constitué par des échantillons de quelques centimètres carrés de

surface et de quelques centièmes de millimètre d'épaisseur réalisés, soit par prélèvement à la scie et amincissement à la lime douce, soit par laminage. L'amincissement est ensuite poursuivi par dissolution électrolytique à l'aide d'un appareil semi-automatique analogue à celui qui est représenté sur la figure 1 et utilisant le procédé Knuth-Winterfeldt. La préparation amincie mécaniquement étant placée à l'anode de la cellule, on la polit alternativement sur chacune de ses faces, pendant 5 à 10 secondes chaque fois, jusqu'à destruction complète de la région soumise au polissage. Les fragments qui résultent de cette destruction sont entraînés dans le bêcher qui contient l'électrolyte. Après les avoir recueillis et lavés à l'eau distillée, on les examine dans le microscope électronique.

Si l'on utilise l'électrolyte A2, recommandé par le constructeur de l'appareil pour le polissage du beryllium, on obtient des micrographies qui sont parsemées de taches noires. Nous n'avons pu déterminer l'origine de ces attaques; peut-être fournissent-elles la possibilité de révéler des impuretés à l'état de traces.

Avec l'électrolyte E2 par contre, constitué par 300 g de nitrate de cuivre, 900 cm<sup>3</sup> d'alcool méthylique et 30 cm<sup>3</sup> d'acide nitrique, la tension appliquée aux bornes de la cellule étant de 50 volts, on obtient des coupes parfaitement claires, sans attaque préférentielle et dans lesquelles la sous-structure, les dislocations et les phases étrangères sont mises en évidence avec beaucoup de contraste.

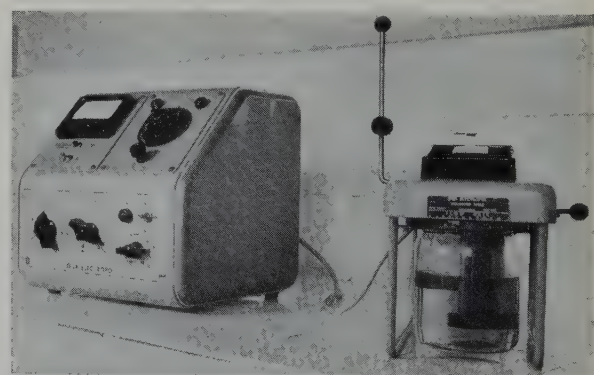
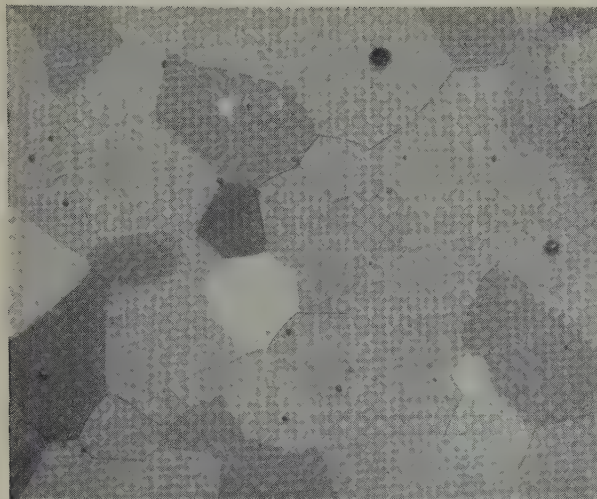


Fig. 1. Appareil de polissage électrolytique semi-automatique.

Fig. 2. Tôle C, recuite 1 h à 1000°C.  $\times 110$ .

### 3. Elaboration des échantillons

Nous nous sommes proposé de poursuivre par la technique des coupes minces, la comparaison entre produits élaborés à partir de métal coulé ou de matières pulvérulentes, précédemment entreprise par les méthodes classiques<sup>3</sup>).

Le beryllium utilisé dans ces essais était du métal de pureté commerciale, dont l'analyse à l'état coulé-filé était la suivante:

Fe	Si	Cu	Mn	Mg	Ti	Al	B	Cl
ppm	300	200	<100	<50	<50	<100	300	<2
								<100

BeO: 0,1 à 0,3 %

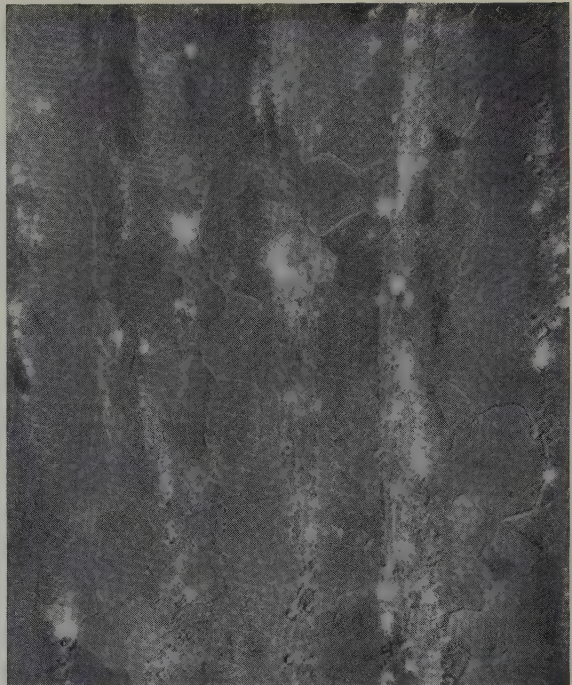
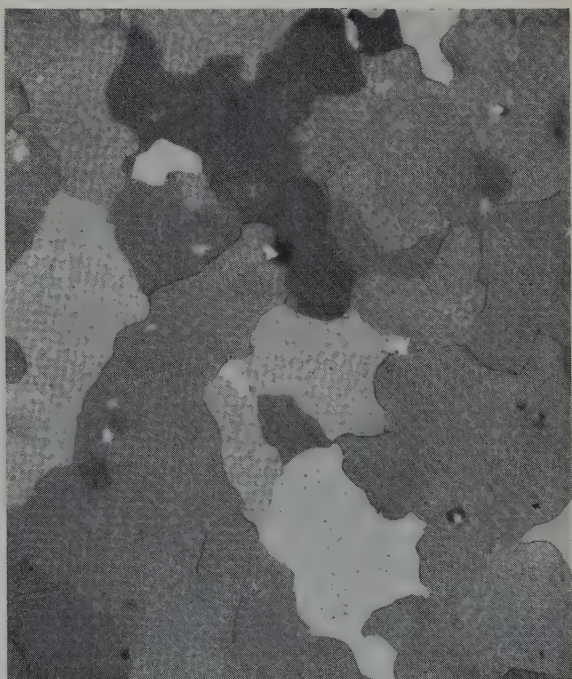
A l'état fritté, l'analyse demeure sensiblement la même mais le fer passe aux environs de 700 ppm et l'oxyde à 0,7-0,8 %.

Des tôles minces ont été réalisées par les deux processus sommairement décrits ci-après:

#### 1) Tôle C, à partir de métal coulé.

Une billette coulée de 2,5 kg, a été filée en largets de 50 × 15 mm, laminée à 800°C, en travers par rapport au filage, de 15 mm à 2/10 mm, puis à froid de 2/10 à 5/100 mm.

Un traitement thermique de 1 h à 800°C ou à 1000°C, effectué sous vide à l'épaisseur de 5/100 mm, provoque la recristallisation en grains réguliers polygonaux (fig. 2).

Fig. 3. Tôle F, après filage. Particules d'oxyde en clair. Recristallisation en bandes.  $\times 370$ .Fig. 4. Tôle F, après laminage et recuit de 1 h à 1000°C.  $\times 130$ .

2) Tôle F, élaborée par métallurgie des poudres.

La poudre, de grain moyen voisin de 80 microns, a été comprimée successivement à froid et à 500° C puis filée à 1000° C en largets de 50 × 15 mm. Après filage, la texture est très orientée; l'oxyde, identifiable sous forme de taches blanches sur la figure 3, est réparti en bandes discontinues allongées dans le sens du filage. Entre les bandes d'oxyde, le métal est recristallisé en grains fins irréguliers.

Les largets tronçonnés sont laminés, en travers par rapport au filage, de 15 mm à 1/10 mm à chaud et ensuite à froid de 1/10 à 7/100 mm. Après laminage à froid, la texture de filage a disparu et la structure micrographique est constituée de grains à contours irréguliers, sans orientation visible. L'oxyde est réparti dans toute la tôle sous forme de très fines particules isolées et de quelques agrégats.

Un recuit sous vide pendant 1 h à 1000° C ne modifie pas radicalement cette structure qui demeure irrégulière avec des contours de grains incurvés (fig. 4 que l'on comparera à la fig. 2).

Le diagramme de Debye-Scherrer pris après laminage à froid (fig. 5) est caractéristique de l'état écroui. Les points blancs qui parsèment les anneaux proviennent probablement de grains qui n'ont été que peu déformés par le faible taux d'écrouissage. Après recuit de 1 h à 1000° C (fig. 6), le diagramme est de type recristallisé.

4. Examen au microscope électronique, sur coupes minces

4.1. TÔLE C

Après amincissement par la méthode que nous avons exposée, les coupes sont claires et ne présentent que très peu d'oxyde et de constituants hors solution lors de l'examen au microscope électronique. A l'état brut de laminage à froid (figs. 7 et 8), les monocristaux sont divisés en bandes ou ensembles polygonaux de sous-grains dont les dimensions varient de 1 micron à une dizaine de microns. Ces sous-grains sont séparés par des frontières très

marquées. Leur intérieur est recouvert d'un réseau très dense de dislocations.

Le recuit de 30 minutes à 800° C sous vide, à l'épaisseur de 5/100 mm, fait disparaître la majorité de ces ensembles de dislocations et les plages observées sont uniformes et sans structure. L'aspect des coupes minces est celui qui est reproduit sur la figure 9 et qui a été obtenu par traitement de 1 h à 1000° C. Quelques rares réseaux de dislocations peuvent cependant être observés sur certaines plages, soit qu'ils aient survécu au traitement thermique, soit qu'ils proviennent d'une légère déformation plastique

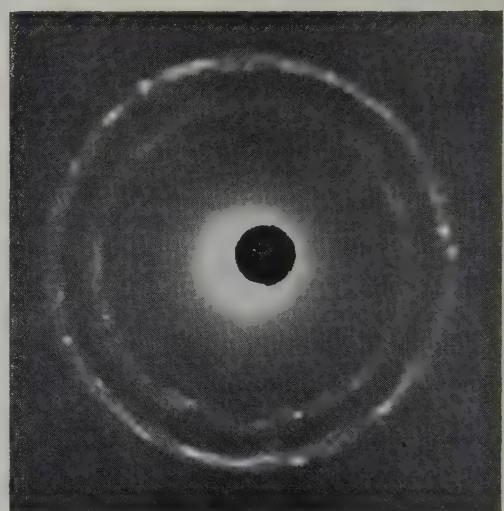


Fig. 5. Tôle F, brute de laminage.

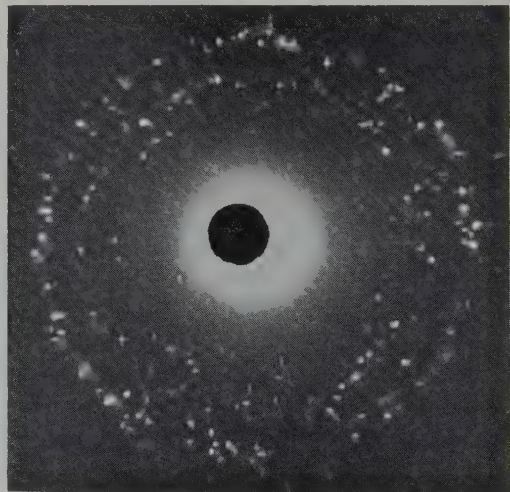


Fig. 6. Tôle F, recuite 1 h à 1000° C.

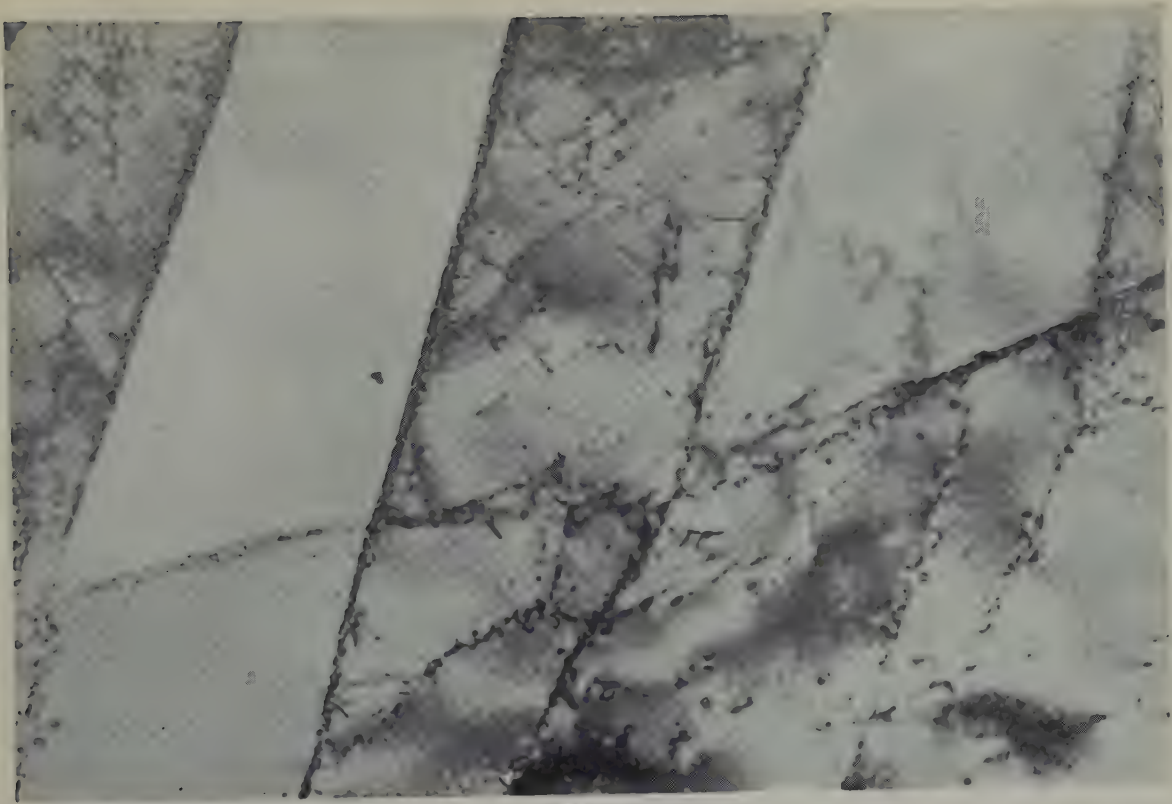


Fig. 7

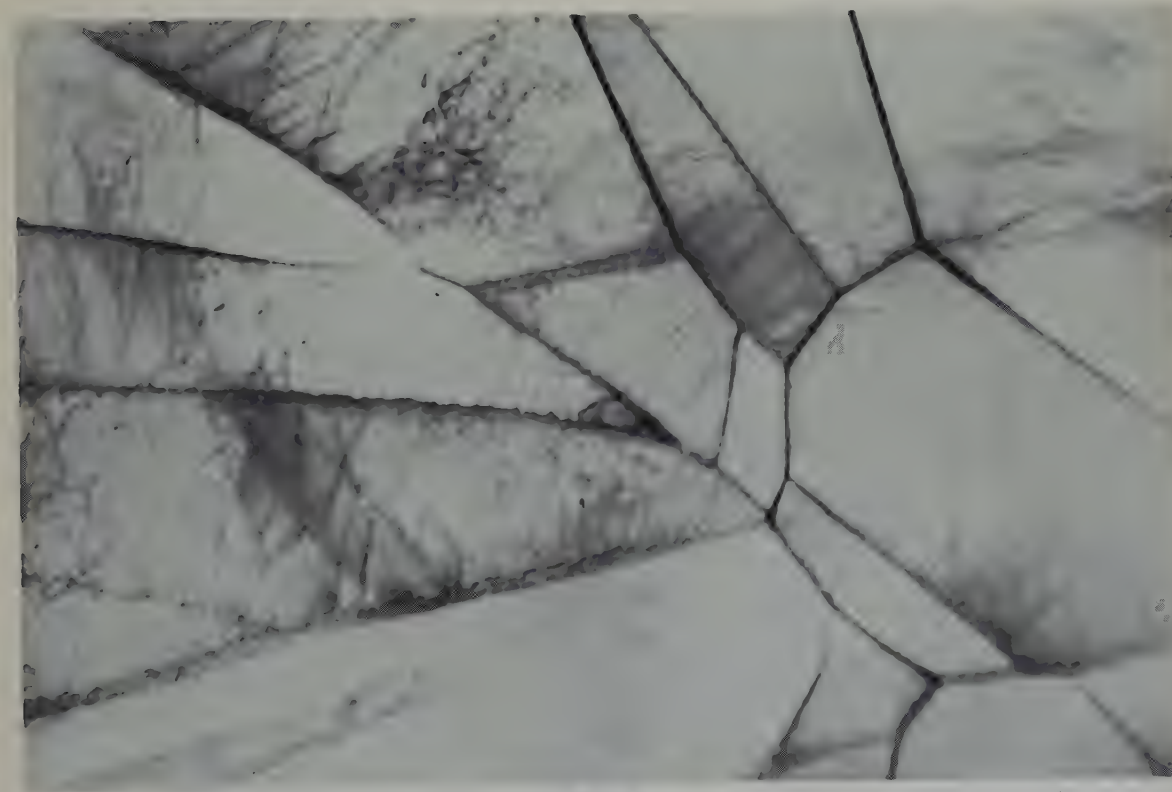


Fig. 8

Figs. 7 et 8. Tôle C, brute de laminage. Coupes minces.  $\times 16\,000$ .

1  $\mu$

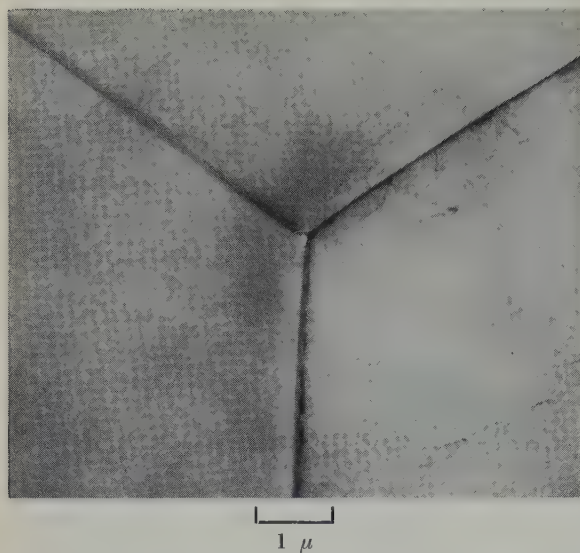


Fig. 9. Tôle C. Recuite 1 h à 1000° C. Coupe mince.  $\times 10\,500$ .

lors de la manipulation des préparations: sur la figure 10 par exemple, on reconnaîtra un "empilement" de dislocations dans un plan de glissement contre un joint de grains (marqué par une flèche). Un autre système de dislocations tend à donner par intersection avec cet empilement, un réseau hexagonal. Un phénomène analogue, à un stade plus avancé, a été enregistré sur la figure 11. A quelques irrégularités près, la maille du réseau hexagonal de dislocations devient de plus en plus grande lorsqu'on s'éloigne du joint (repéré par des flèches) comme on peut s'y attendre d'après la loi qui régit l'empilement des dislocations dans un plan de glissement contre un obstacle fixe. On identifiera sur la même figure un second empilement de dislocations, situé dans le grain adjacent.

#### 4.2. TÔLE F

Les coupes, obtenues à partir de métal élaboré par la métallurgie des poudres, sont assez sensiblement différentes des précédentes: la sous-structure y est moins nettement délimitée et les micrographies sont parsemées de taches sombres, isolées ou agglomérées qui correspondent aux particules d'oxyde.

#### 1. Sous-structure

Un aspect typique de ces coupes, après laminage à froid, est représenté sur la figure 12. L'interprétation peut en être donnée à l'aide d'un diagramme de microdiffraction (fig. 13) effectué sur une plage de 3 microns de diamètre située au centre de la figure 12: Le dédoublement des taches de diffraction indique que l'on est en présence de deux sous-grains, d'orientation moyenne (10 $\bar{1}$ 1). La ligne horizontale qui sépare la figure 12 en deux parties à peu près égales, constitue le joint entre ces sous-grains. Les veines épaisses qui aboutissent à ce sous-joint sont constituées par des ensembles complexes de dislocations. D'autres dislocations moins denses sont également identifiables. Les particules d'oxyde, représentées par de petites taches grises de 1/10° de micron environ, sont peu nombreuses ce qui explique que l'oxyde n'ait donné sur le diagramme de la figure 13, ni taches, ni anneaux.

#### 2. Oxyde

La figure 14 représente au contraire une plage dans laquelle sont présentes peu de dislocations, mais de nombreuses particules d'oxyde, les unes dispersées, les autres aggrégées en un agrégat long de 5 microns. Ces particules font apparaître sur le diagramme de micro-diffraction correspondant (fig. 15) les anneaux ponctués de l'oxyde BeO. Les taches de diffraction appartiennent à deux cristaux de beryllium au moins. Grâce à elles, un joint de grains, par ailleurs peu visible, a été identifié. Il est repéré par une flèche sur la figure 14. On remarquera que l'agrégat d'oxyde est intra-granulaire et non pas situé à la limite actuelle des grains.

#### 3. Traitement thermique

Des recuits sous vide ont été effectués sur cette tôle à l'épaisseur de 7/100 mm. Après un recuit de 30 min à 800° C, les images s'éclaircissent par disparition des veines épaisses de dislocations; cependant des sous-joints subsistent ainsi que des dislocations dont le déplacement a été freiné par des particules d'oxyde et



Fig. 10

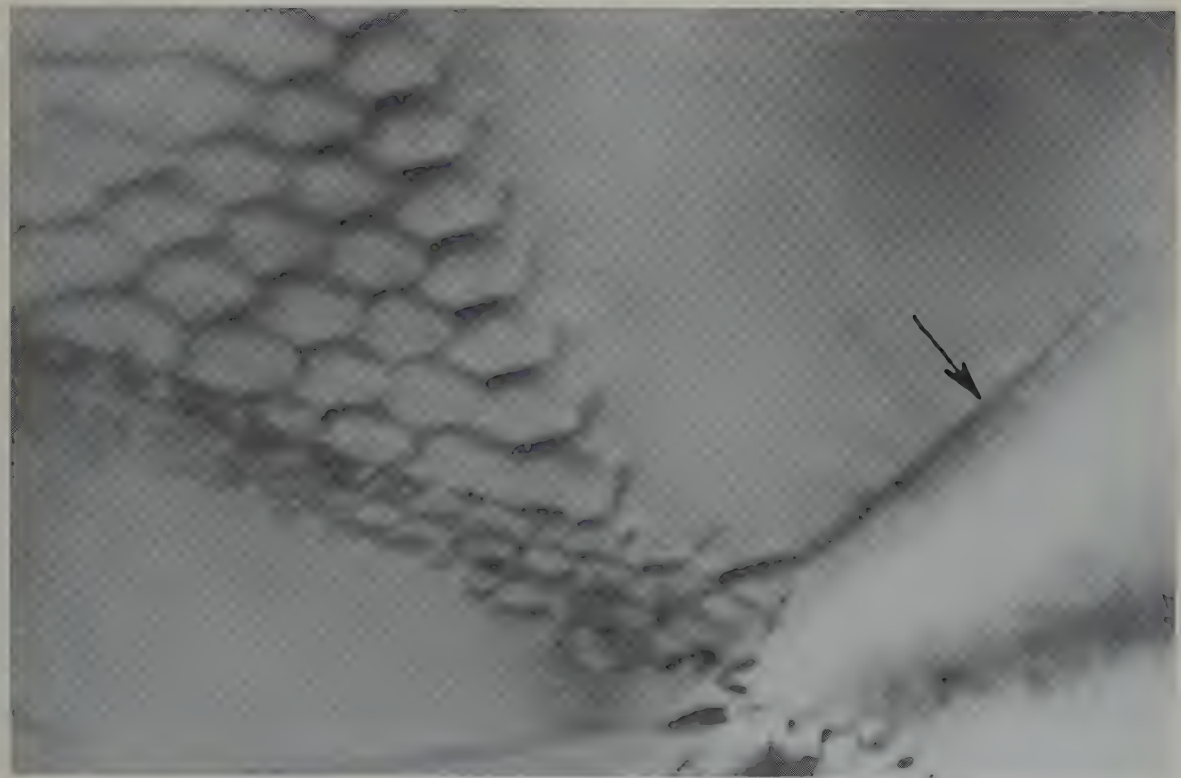


Fig. 11

Figs. 10 et 11. Tôle C, recuite 1 h à 1000°C. Coupes minces  $\times 100\,000$

$\frac{1}{10}\mu$



Fig. 12. Micrographie.

1  $\mu$



Fig. 14. Micrographie. Particules d'oxyde. La flèche indique un joint de grains.



Fig. 13. Microdiffraction de la fig. 12. Coupe (1011).



Fig. 15. Microdiffraction de la fig. 14. Anneaux de l'oxyde.

Figs. 12-15. Tôle F. Etat brut de laminage. Coupes minces.  $\times 12\,000$ .



Fig. 16. Coupe (0001).



Fig. 17

Figs. 16 et 17. Tôle F. Etat recuit 30 min à 800° C. Coupes minces.  $\times 80\,000$ .

$\frac{1}{10} \mu$

qui y demeurent ancrées (figs. 16 et 17). Après 3 h à 800° C, la densité des dislocations a encore diminué; il en demeure cependant un assez grand nombre, groupées en parois de sous-grains. De même, un traitement de 15 minutes à 850° C a pour effet de simplifier les réseaux de dislocations qui ne disparaissent cependant pas complètement. Dans des échantillons traités pendant 1 heure à 1000° C, nous avons encore trouvé des réseaux analogues, en même temps que les diagrammes de Debye-Scherrer donnent des résultats irréguliers qui peuvent être interprétés comme correspondant à une recristallisation partielle.

Il semble donc que l'amélioration des caractéristiques que l'on enregistre par recuit à 800° C<sup>3)</sup> est liée à la disparition observée d'ensembles complexes de dislocations; l'élimination complète des défauts de structure résultant de l'écrouissage n'est ensuite que lente et progressive et encore très incomplète au bout de 1 h à 1000° C. La "recristallisation" dans ce cas particulier où le taux d'écrouissage réalisé au cours du laminage à froid est faible, prend ainsi un aspect qui est essentiellement celui du perfectionnement de la sous-structure par élimination des dislocations et du grossissement du grain existant. Nous retrouvons le résultat précédemment signalé dans l'étude du traitement thermique de tôles de titane faiblement écrouies<sup>4,5)</sup>. D'après les micrographies enregistrées, on peut estimer par ailleurs que les particules d'oxyde freinent la disparition des dislocations en les ancrant et contribuent sans doute à donner au phénomène son caractère de lenteur et de progressivité.

## 5. Conclusion

Dans les conditions où nous avons opéré, le laminage à froid fait apparaître dans le métal C coulé-filé-laminé, une sous-structure régulière et des réseaux denses mais clairs de dislocations; dans les tôles F élaborées par la métallurgie des poudres, une sous-structure beaucoup moins nette et des enchevêtrements complexes de dislocations en veines épaisses.

Le recuit effectué entre 800 et 1000° C qui

améliore grandement les caractéristiques mécaniques, entraîne la recristallisation du métal C et, pour le métal F faiblement écroui, des phénomènes progressifs de perfectionnement



Fig. 18. Beryllium d'origine étrangère. Coupe mince. Cristal d'oxyde.  $\times 50\,000$ .



Fig. 19. Recuit 1 h à 1000° C. Réplique de carbone. Particules d'oxyde extraites.  $\times 11\,500$ .

par élimination des dislocations et migration des joints du grain d'écrouissage.

Dans les tôles réalisées par la métallurgie des poudres, l'oxyde est présent sous forme de particules de  $1/10^\circ$  de micron environ, dispersées dans tout le produit avec une densité qui peut varier sensiblement d'une plage à l'autre. Ces particules peuvent se trouver agglomérées en agrégats dont les dimensions atteignent plusieurs microns. Dans des tôles d'origine étrangère, nous avons décelé par ailleurs des cristaux plus gros (fig. 18) qui correspondent probablement à l'oxydation complète d'une fine paillette de poudre. L'ensemble de nos observations sur coupes minces, complétées par des extractions de l'oxyde à l'aide de répliques de carbone (fig. 19), indique que les particules et agrégats d'oxyde dans les tôles ne sont qu'accidentellement dispersés aux joints des grains actuels

et que, lorsque ces barrières d'oxyde existent, elles sont de toutes façons très discontinues.

Nos remerciements vont à MM. Billamboz et Mirand pour leur précieuse collaboration technique à ce travail et à la Direction de la Compagnie Péchiney qui en a autorisé la publication.

### Bibliographie

- 1) J. D. Baird, O. P. Hartree et R. Phillips, *Nature* 182 (1958) 1660
- 2) A. Saulnier et P. Mirand, *C.R. Acad. Sc.* 250 (1960) 709
- 3) R. Syre, A. Saulnier et M. Perez, *Revue de Métallurgie* 56 (1959) 359
- 4) A. Saulnier et R. Develay, *Revue de Métallurgie* 54 (1957) 689
- 5) A. Saulnier et R. Develay, *Symposium de Métallurgie spéciale sur la Recristallisation, Saclay* (1957) p. 89. (Edité par „Presses Universitaires” Paris)

## PEROVSKITE-TYPE COMPOUNDS BASED ON PLUTONIUM

L. E. RUSSELL, J. D. L. HARRISON and N. H. BRETT

UKAEA Research Group, Metallurgy Division, Atomic Energy Research Establishment, Harwell, Didcot, UK

Received 27 May 1960

The preparation of perovskite-type compounds containing trivalent or quadrivalent plutonium has been attempted. Crystallographic data for the compounds  $\text{PuAlO}_3$ ,  $\text{PuVO}_3$ ,  $\text{PuCrO}_3$  and  $\text{BaPuO}_3$  are reported.

On a essayé la préparation de composés de plutonium du type perovskite, contenant le plutonium trivalent ou quadrivalent. On donne des détails cristallo-

## 1. Introduction

Of the structures adopted by  $\text{ABO}_3$ -type <sup>†</sup> compounds the perovskite structure is one of the most common and one of the most fully investigated since many of these compounds have interesting dielectric properties <sup>1)</sup>. The ideal perovskite structure typified by barium titanate,  $\text{BaTiO}_3$  <sup>2)</sup>, above 120° C, is illustrated in fig. 1. It is cubic, with a cell side of about 4 Å, each cell containing one formula-unit. The structure may be regarded as a network of  $\text{BO}_6$  octahedra linked through oxygen ions at the corners of each octahedron, with A ions located in the interstices between the  $\text{BO}_6$  groups, the A ions being in 12 fold co-ordination with the oxygen ions surrounding them.

From geometrical considerations <sup>3)</sup> it can be deduced that the radius ratio  $R_B/R_O$  must be between 0.414 and 0.732 for a 6-fold co-ordination of oxygen about a B cation. Taking Pauling's <sup>4)</sup> value for the radius of the oxygen ion, 1.40 Å, the radius of B cations in perovskite structures should therefore be between 0.58 Å and 1.025 Å. The only restriction on the size of the A ions is that they should be able to fit

<sup>†</sup> A and B represent cations present in the perovskite structure.

graphiques pour les composés  $\text{PuAlO}_3$ ,  $\text{PuVO}_3$ ,  $\text{PuCrO}_3$  et  $\text{BaPuO}_3$ .

Die Herstellung von Verbindungen von perovskitartiger Struktur, mit drei- oder vierwertigen Plutonium, ist versucht worden. Kristallographische Zahlwerte werden angegeben für die Verbindungen  $\text{PuAlO}_3$ ,  $\text{PuVO}_3$ ,  $\text{PuCrO}_3$  und  $\text{BaPuO}_3$ .

into the interstices without causing excessive distortion of the network.

In the idealised perovskite structure made of rigid spheres, each in contact with its neighbours, the radii of the  $\text{A}^{n+}$ ,  $\text{B}^{(6-n)+}$  and  $\text{O}^{2-}$  ions are related by the following equation

$$R_A + R_O = \sqrt{2}(R_B + R_O). \quad (1)$$

However, ions are not rigid spheres and the cubic structure can still be obtained when there is some slight distortion of the  $\text{BO}_6$  network. To allow for this a tolerance factor  $t$  is introduced into eq. (1).

$$R_A + R_O = t\sqrt{2}(R_B + R_O). \quad (2)$$

Cubic structures are usually found when  $t$  is close to unity and perovskite-like structures of rhombohedral or orthorhombic symmetry, which represent slight distortions of the cubic lattice, are found for values of  $t$  down to 0.8.

Zachariasen <sup>5)</sup> estimates that the ionic radii for  $\text{Pu}^{3+}$  and  $\text{Pu}^{4+}$  (C.N.=6) are 1.00 Å and 0.90 Å respectively. When  $\text{Pu}^{3+}$  is in 12-fold co-ordination with oxygen its effective radius is increased to 1.09 Å. Substitution in eq. (2) indicates that  $\text{Pu}^{3+}\text{B}^{3+}\text{O}_3$  perovskite-type compounds might be formed when the radius of

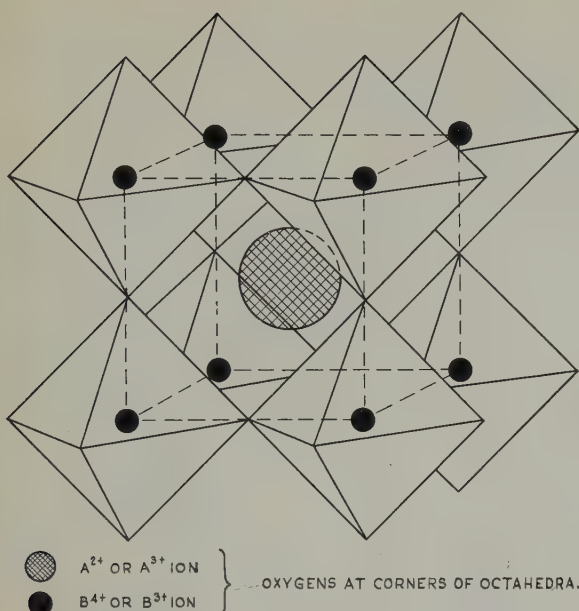


Fig. 1. Ideal cubic perovskite structure.

$B^{3+}$  is between 0.36 Å and 0.80 Å. Cubic structures would be favoured by the smaller sized  $B^{3+}$  ion. Similarly  $A^{2+}Pu^{4+}O_3$  compounds might have a perovskite-type structure if the  $A^{2+}$  ion has a radius between 1.20 Å and 1.85 Å and in this case cubic structures would be expected where the ionic radius is close to 1.85 Å.

Suitable  $B^{3+}$  ions in  $Pu^{3+}B^{3+}O_3$  are  $Al^{3+}$ ,  $V^{3+}$ ,  $Cr^{3+}$ ,  $Mn^{3+}$ ,  $Fe^{3+}$  and  $Ga^{3+}$  and suitable  $A^{2+}$  ions in  $A^{2+}Pu^{4+}O_3$  are  $Ba^{2+}$  and  $Pb^{2+}$ .

## 2. Experimental Details

Attempts have been made to prepare perovskite compounds based on  $Pu^{3+}$  and  $Pu^{4+}$  in combination with the ions mentioned above. In addition preparations containing plutonium with  $Sr^{2+}$ ,  $Ca^{2+}$ ,  $Mg^{2+}$ ,  $Cd^{2+}$ ,  $Pb^{2+}$  and  $K^+$  ions have been examined to extend the range of the work and to define more closely the limiting values for the tolerance factor.

The  $K^+$  ion was included to investigate the possibility that  $K^+Pu^{5+}O_3$  exists since it is known that  $Pu^{5+}$  is found in liquids.

Plutonium was introduced as oxide powder with a surface area of 28 m<sup>2</sup>/g prepared by the decomposition of plutonium oxalate at about

600° C. In some experiments the  $PuO_2$  powder was reduced by heating for 3 hours at 1650° C in hydrogen prior to mixing with the other components. This treatment yielded a product which contained about 50 %  $\alpha$ - $Pu_2O_3$  and 50 %  $PuO_2$  as determined by X-ray analysis.

The other oxides were incorporated directly or as oxalate, carbonate or hydroxide. Stoichiometric amounts of the powders were intimately mixed and then fired directly in alumina containers or pressed into small pellets and fired on alumina or thoria boats. Thoria containers were used where chemical reaction between  $\alpha$ - $Pu_2O_3$  and alumina was suspected.

The results of some experiments showed that a slight excess of  $PuO_2$  was present in the fired mixture. In these cases additional specimens were prepared from mixtures containing about 10 % less than the stoichiometric amount of  $PuO_2$ .

A summary of the methods used is given below:

*Method A.* Mixed powders fired in hydrogen.

*Method B.* Mixed powders compacted to 0.6 cm (1/4") right cylinders at 300 kg/cm<sup>2</sup> (40 000 psi). Sintered in hydrogen.

*Method C.* Mixed powders + excess graphite above that needed to reduce  $PuO_2$  to  $Pu_2O_3$ . Compacted into 0.6 cm (1/4") right cylinders and sintered in argon.

*Method D.*  $PuO_2$  previously reduced in hydrogen to about 50 %  $\alpha$ - $Pu_2O_3$  used instead of  $PuO_2$ . Compacted into 0.6 cm (1/4") right cylinders. Sintered in hydrogen.

*Method E.* Mixed powders fired in air.

*Method F.* Mixed powders compacted into 0.6 cm (1/4") right cylinders and sintered in air.

X-ray powder photographs were obtained from all fired specimens using molybdenum K $\alpha$  radiation in an 8 cm. Guinier focussing camera<sup>6</sup>.

## 3. Results

The experiments performed together with an assessment of the X-ray diffraction patterns are summarised in table 1. Perovskite or

TABLE 1  
Summary of plutonium perovskite preparations

Compound	$R_A$ (C.N.=12) (Å)	$R_B$ (Å)	$t$	Firing conditions					X-ray examination	
				Reactants	Temp (°C)	Time (h)	Atmosphere	Container		
PuAlO <sub>3</sub>	1.09	0.50	0.93	PuO <sub>2</sub> +Al <sub>2</sub> O <sub>3</sub> +C	1500	2	Argon	Alumina	(PuAlO <sub>3</sub> ) Cubic pattern with line splitting. PuO <sub>2</sub> only. PuO <sub>2</sub> +cubic pattern (PuAlO <sub>3</sub> ). Cubic pattern (PuAlO <sub>3</sub> ) with line splitting and some other lines. PuO <sub>2</sub> +Pu <sub>2</sub> O <sub>3</sub> +cubic pattern (PuAlO <sub>3</sub> ).	
				PuO <sub>2</sub> +Al(OH) <sub>3</sub>	1500	2	Air	Alumina		
				PuO <sub>2</sub> +Al(OH) <sub>3</sub>	1500	2	Hydrogen	Alumina		
				PuO <sub>2</sub> +Al(OH) <sub>3</sub> (10 % excess)	1500	2	Hydrogen	Thoria		
PuVO <sub>3</sub>	1.09	0.66	0.86	PuO <sub>2</sub> +V <sub>2</sub> O <sub>5</sub>	1500	2	Hydrogen	Thoria	Orthorhombic pattern only (PuVO <sub>3</sub> ). Orthorhombic pattern only (PuVO <sub>3</sub> ). Orthorhombic pattern only (PuVO <sub>3</sub> ).	
				PuO <sub>2</sub> +V <sub>2</sub> O <sub>5</sub>	1500	2	Hydrogen	Thoria		
				PuVO <sub>3</sub> from above	Arc melted		Argon			
PuCrO <sub>3</sub>	1.09	0.64	0.87	PuO <sub>2</sub> +CrO <sub>3</sub>	1500	2	Hydrogen	Alumina	PuAlO <sub>3</sub> . Orthorhombic pattern only (PuCrO <sub>3</sub> ). PuO <sub>2</sub> +orthorhombic pattern (PuCrO <sub>3</sub> ).	
				PuO <sub>2</sub> +CrO <sub>3</sub>	1500	2	Hydrogen	Thoria		
				PuO <sub>2</sub> +Pu <sub>2</sub> O <sub>3</sub> +CrO <sub>3</sub>	1300	2	Hydrogen	Thoria		
PuMnO <sub>3</sub>	1.09	0.62	0.87	PuO <sub>2</sub> +MnCO <sub>3</sub>	1500	2	Hydrogen	Alumina	Cubic pattern (PuMnO <sub>3</sub> )+ other lines. PuO <sub>2</sub> +other lines. PuO <sub>2</sub> +other lines.	
				PuO <sub>2</sub> +MnCO <sub>3</sub>	1500	2	Hydrogen	Thoria		
				PuO <sub>2</sub> +MnCO <sub>3</sub>	1500	2	Hydrogen	Thoria		
PuFeO <sub>3</sub>	1.09	0.60	0.88	PuO <sub>2</sub> +Fe <sub>2</sub> (C <sub>2</sub> O <sub>4</sub> ) <sub>5</sub> H <sub>2</sub> O	1500	2	Hydrogen	Alumina	PuO <sub>2</sub> +other lines (weak). PuO <sub>2</sub> +other lines (weak). PuO <sub>2</sub> +other lines (weak).	
				PuO <sub>2</sub> +Fe <sub>2</sub> (C <sub>2</sub> O <sub>4</sub> ) <sub>5</sub> H <sub>2</sub> O	1500	2	Hydrogen	Thoria		
				PuO <sub>2</sub> +Pu <sub>2</sub> O <sub>3</sub> +Fe <sub>2</sub> (C <sub>2</sub> O <sub>4</sub> ) <sub>5</sub> H <sub>2</sub> O	1300	2	Hydrogen	Thoria		
PuGaO <sub>3</sub>	1.09	0.62	0.87	PuO <sub>2</sub> +Ga <sub>2</sub> O <sub>3</sub>	1600	3	Hydrogen	Thoria	B	PuO <sub>2</sub> +Pu <sub>2</sub> O <sub>3</sub> .
SrPuO <sub>3</sub>	1.23	1.00	0.78	PuO <sub>2</sub> +SrCO <sub>3</sub>	1500	2	Air	Alumina	PuO <sub>2</sub> +other lines. PuO <sub>2</sub> +other lines. PuO <sub>2</sub> +other lines. PuO <sub>2</sub> +other lines.	
				PuO <sub>2</sub> (SrCO <sub>3</sub> ) <sub>(10 % excess)</sub>	1400	3	Air	Thoria		
				PuO <sub>2</sub> +SrCO <sub>3</sub> (10 % excess)	1750	½	Air	Thoria		
				PuO <sub>2</sub> +SrCO <sub>3</sub> (10 % excess)	Arc melted		Argon			
BaPuO <sub>3</sub>	1.47	1.00	0.85	PuO <sub>2</sub> +BaCO <sub>3</sub>	1500	1	Air	Alumina	PuO <sub>2</sub> +BaPuO <sub>3</sub> (cubic). PuO <sub>2</sub> +BaPuO <sub>3</sub> (cubic).	
				PuO <sub>2</sub> +BaCO <sub>3</sub> (10 % excess)	1650	3	Air	Thoria		
CaPuO <sub>3</sub>	1.08	1.00	0.73	PuO <sub>2</sub> +CaCO <sub>3</sub>	1500	1	Air	Alumina	PuO <sub>2</sub> +other lines. PuO <sub>2</sub> only. Melted - PuO <sub>2</sub> only. Melted - PuO <sub>2</sub> only. PuO <sub>2</sub> only. PuO <sub>2</sub> only.	
				PuO <sub>2</sub> +CaCO <sub>3</sub>	1400	3	Air	Thoria		
				PuO <sub>2</sub> +CaCO <sub>3</sub>	1600	3	Air	Alumina		
				PuO <sub>2</sub> +CaCO <sub>3</sub>	1550	2	Air	Alumina		
				PuO <sub>2</sub> +CaCO <sub>3</sub>	1090	2	Air	Alumina		
				PuO <sub>2</sub> +CaCO <sub>3</sub>	1450	3	Air	Alumina		
MgPuO <sub>3</sub>	0.71	1.00	0.63	PuO <sub>2</sub> +MgCO <sub>3</sub>	1500	3	Air	Alumina	F	PuO <sub>2</sub> +MgO.
CdPuO <sub>3</sub>	1.06	1.00	0.73	PuO <sub>2</sub> +CdCO <sub>3</sub>	1500	3	Air	Alumina	F	PuO <sub>2</sub> only.
PbPuO <sub>3</sub>	1.44	1.00	0.84	PuO <sub>2</sub> +Pb <sub>3</sub> O <sub>4</sub>	1500	3	Air	Alumina	F	PuO <sub>2</sub> only.
BePuO <sub>3</sub>	0.34	1.00	0.52	PuO <sub>2</sub> +BeO	1500	3	Air	Thoria	F	PuO <sub>2</sub> only.
K PuO <sub>3</sub>	1.45	1.00	0.84	PuO <sub>2</sub> +K <sub>2</sub> CO <sub>3</sub>	1300	1	Oxygen	Platinum	E	PuO <sub>2</sub> only.

NOTE:  $R$  values from Pauling<sup>4</sup>.  $t = \frac{R_0 + R_A}{\sqrt{2} (R_0 + R_B)}$ .

perovskite-like structures which have been produced and identified are  $\text{BaPuO}_3$ ,  $\text{PuAlO}_3$ ,  $\text{PuVO}_3$  and  $\text{PuCrO}_3$ . Typical diffraction patterns are shown in fig. 4.

### 3.1. $\text{PuAlO}_3$ (TABLE 2)

“Plutonium aluminate” was first observed in the remains of a pellet of mixed  $\text{PuO}_2$  and graphite which had been fired on an alumina boat in an argon atmosphere. The graphite appeared to have reduced the  $\text{PuO}_2$  to  $\alpha\text{-Pu}_2\text{O}_3$  which had reacted with the alumina container. The  $\text{PuAlO}_3$  formed had melted and some of it

had volatilised and condensed in cooler parts of the furnace tube. An X-ray photograph, (film 646) of powder taken from the condensate gave lines which were indexed on a hexagonal unit cell. All the lines except the one corresponding to the (30.7) plane had indices which were transformed into those of a rhombohedral unit cell. The dimensions of the two equivalent cells are given in table 2. Attempts to index the weaker lines, either in conjunction with the strong lines or by themselves, have been unsuccessful.

Other preparations made by sintering  $\text{PuO}_2$

TABLE 2  
X-ray powder diffraction data for  $\text{PuAlO}_3$

Indices		Film 646 $\text{PuAlO}_3$			Film 754 $\text{PuAlO}_3$			PrAlO <sub>3</sub>	
Hex	Rhomb	$d_{\text{obs}}$ (Å)	$d_{\text{calc}}$ (Å)	$I$	$d_{\text{obs}}$ (Å)	$I$	$d_{\text{obs}}$ (Å)	$I$	
01.2	110	3.762	3.760	S	3.775	S	3.750	S	
10.4	211	2.654	2.665	VS	2.663	VS	2.656	VS	
02.1	111								
11.3	210						2.267	W-	
20.2	200	2.162	2.162	M+	2.175	S	2.173	S	
00.6	222	2.164	2.170	M+	2.085	VW	2.159	M-	
02.4	220	1.881	1.881	M+	1.889	M	1.879	S	
21.1	201								
20.5	311						1.728	VVV	
12.2	211						1.687	M-	
11.6	321	1.677	1.679	M+	1.683	M	1.679	M-	
30.0	211	1.538	1.539	M-	1.545	W+	1.536	S	
01.8	332	1.530	1.530	M+	1.537	M	1.528	M-	
22.0	202						1.332	M-	
20.8	422	1.327	1.326	W	1.332	W+	1.326	M	
31.2	301						1.257	W-	
03.6	330	1.253	1.253	W	1.254	W	1.254	M-	
10.10	433	1.249	1.249	W+	1.240	VW	1.249	W-	
13.4	321						1.192	M	
12.8	431	1.189	1.188	W+			1.188	M+	
30.7		1.184	1.184	W+	3.483	VW			
04.2	222	1.136	1.136	W	2.549	VW			
22.10	424	1.130	1.131	W+	2.486	VW			
04.4	004	1.087	1.087	W	1.909	VW	These lines appear in 754 but not in 646.		
00.12	444	1.081	1.081	W	1.629	W+			
21.10	532	1.039	1.040	W	1.603	W-			
14.0	213	1.007	1.007	VW	1.339	VW			
11.12	543	1.002	1.002	M	1.258	W			

S = strong; VS = very strong; M = medium strong; W = weak; VW = very weak.

The lines on film 646 were indexed on the basis of an hexagonal unit cell with constants:  $a = 5.367$ ,  $c = 13.43$  Å. With the exception of the (30.7) line, all the indices could be transformed to those of a rhombohedral pseudo-cell, whose dimensions are:  $a = 5.331$ ,  $\alpha = 90^\circ 24'$ .

$+\text{Al(OH)}_3$  and  $\text{PuO}_2 + \alpha\text{-Pu}_2\text{O}_3 + \text{Al(OH)}_3$  in hydrogen yielded different and more complex diffraction patterns (table 2). The patterns tend to differ one from another in the position and number of the weaker lines but the strong lines show good reproducibility and can be indexed by comparison with the indices of the corresponding lines in film 646. Attempts to index the weaker lines, either in conjunction

with the strong lines or by themselves, have been unsuccessful. The fact that no two specimens gave the same diffraction pattern indicates that the "compound" may have a variable composition and structure or that in cooling to room temperature it may undergo a phase transformation which varies in completeness with small changes in experimental procedure.

TABLE 3  
X-ray powder diffraction data for  $\text{PuVO}_3$ ,  $\text{PuCrO}_3$ ,  $\text{PrFeO}_3$

<i>hkl</i>	$\text{PuVO}_3$			$\text{PuCrO}_3$			$\text{PrFeO}_3$		
	<i>d</i> <sub>calc.</sub> ( $\text{\AA}$ )	<i>d</i> <sub>obs.</sub> ( $\text{\AA}$ )	<i>I</i>	<i>d</i> <sub>calc.</sub> ( $\text{\AA}$ )	<i>d</i> <sub>obs.</sub> ( $\text{\AA}$ )	<i>I</i>	<i>d</i> <sub>calc.</sub> ( $\text{\AA}$ )	<i>d</i> <sub>obs.</sub> ( $\text{\AA}$ )	<i>I</i>
110	3.919	3.917	S	3.879	3.880	S	3.915		3.896 M+
002							3.904		
111	3.501	3.508	M	3.469	3.468	M-	3.499	3.485	M
				3.128		W			
020	2.802	2.802	M				2.789	2.790	M+
112	2.762	2.768	VS	2.742	2.743	VS	2.765	2.755	VS
200	2.740	2.745	M				2.747	2.750	M
021	2.638	2.642	M	2.597	2.599	M-	2.627	2.618	W+
103	2.345			2.337			2.353		
		2.352	W		2.336	W-		2.344	W
211	2.347			2.332			2.350		
022	2.275	2.275	M	2.247	2.248	S-	2.270	2.264	M
202	2.241	2.241	M	2.232	2.232	S	2.247	2.244	M
113	2.164	2.167	W+	2.152	2.150	W	2.168	2.163	W
220	1.960	1.960	M+	1.939			1.957	1.956	S
004	1.946	1.948	M	1.940	1.939	S	1.953	1.950	M
023	1.905	1.916	VW				1.903		
221	1.900	1.901	M-	1.820	1.814	W+	1.899	1.897	M
114	1.743	1.743	M	1.734	1.732	M+	1.747	1.745	M
131	1.724	1.724	M	1.699	1.699	W+	1.718	1.716	M+
311	1.695	1.695	VW				1.699	1.697	W
132	1.610	1.609	W	1.589	1.588	W	1.605	1.605	M+
024	1.599	1.599	W				1.599	1.597	M
312	1.587			1.578			1.589		
204	1.587	1.586	S	1.578	1.579	S	1.592	1.589	S+
223	1.564	1.564	W	1.551	1.551	VW	1.564	1.563	W
133	1.462	1.460	W	1.444	1.443	W	1.459	1.459	M
041	1.380			1.371			1.373	1.372	M
224	1.381	1.380	M-	1.372	1.371	M-	1.382	1.382	S+
402	1.292	1.294	W						
314				1.290	1.291	W	1.299	1.299	W+
331	1.288	1.288	W	1.275	1.277	VW	1.287	1.288	W+
116	1.232	1.232	M+	1.227			1.235	1.235	S
241	1.232	1.232	W				1.228	1.228	M
206				1.168	1.169	W	1.176	1.176	W+
135	1.169	1.169	W	1.158	1.158	W	1.169	1.168	W+

3.2. PuVO<sub>3</sub> (TABLE 3)

This pattern was indexed by comparison with the *d*-values for PrFeO<sub>3</sub> as reported by Geller and Wood<sup>7</sup>). The agreement between observed and calculated *d*-values is good and indicates that the assumption of an orthorhombic crystal cell is correct. The close similarity between the intensities of corresponding lines on the diffraction patterns for PuVO<sub>3</sub> and PrFeO<sub>3</sub> suggests that these compounds are isostructural.

PuVO<sub>3</sub> is a light grey-green colour and shows appreciable electrical conductivity. A pellet about 0.5 cm ( $\frac{3}{16}$ ) diameter  $\times$  0.5 cm ( $\frac{3}{16}$ ) long has a resistance of about 100 ohms at room temperature. It appears to be stable up to its melting point, since the diffraction pattern from an arc melted specimen was almost identical with that from a preparation fired at 1500° C.

PuCrO<sub>3</sub> (TABLE 3)

The lines in the PuCrO<sub>3</sub> diffraction patterns were indexed by comparison with those obtained from the PuVO<sub>3</sub> specimens, the two compounds being isostructural. The apparent absence of the (020), (200) and (211) reflections can be attributed to the closeness of these lines to other strong lines.

3.3. PuMnO<sub>3</sub> (TABLE 4)

The diffraction patterns from the PuMnO<sub>3</sub> preparation showed that the structure was of near cubic symmetry but additional weak lines indicated a small departure from the cubic cell. Indexing the pattern by comparison with PrFeO<sub>3</sub> accounts for each line in both position and intensity and suggests that the structure may be orthorhombic.

3.4. BaPuO<sub>3</sub> (TABLE 5)

The lines from the pattern from preparation 1 (1 h 1500° C in air) quoted in table 5 have been indexed in the cubic system. In this preparation a slight excess of PuO<sub>2</sub> was present and line splitting was observed in lines 10, 12 and 16. Preparation 2, which had a slight excess of BaCO<sub>3</sub>, was fired to a higher temperature. This

TABLE 4  
X-ray powder diffraction data for PuMnO<sub>3</sub>

<i>N</i>	<i>d</i> <sub>obs.</sub> (Å)	<i>d</i> $\sqrt{N}$ (Å)	<i>I</i>
1	3.874	3.874	S
	3.462	-	M
2	2.733	3.844	VS
	2.594	-	M
3	2.328	-	W
	2.251	3.857	M+
4	2.227	-	M+
	2.144	-	W
5	2.072	3.867	W
	1.933	-	S-
6	1.878	-	M-
	1.727	3.863	M
8	1.695	-	M-
	1.582	-	M
10	1.575	3.857	M
	1.528	-	S
11	1.441	-	W
	1.367	3.866	W+
9	1.352	-	W
	1.287	3.861	W
12	1.271	-	W
	1.222	3.864	W
13	1.213	-	W+
	1.162	3.854	W
14	1.154	-	W
	1.112	3.853	W
15	1.108	-	W
	1.072	3.865	W
16	1.042	-	W
	1.035	3.858	VW
	1.031	-	M-

Mean = 3.860 Å

still contained PuO<sub>2</sub> but there was no line-splitting. Calculations were made of the intensities of X-ray reflections for BaPuO<sub>3</sub>, on the assumption that it has a BaTiO<sub>3</sub>-type structure, and these have been compared with the observed intensities. This comparison confirmed that BaPuO<sub>3</sub> has a perovskite-type structure.

## 3.5. OTHER PREPARATIONS

Perovskite-type compounds were not formed in those firings intended to produce PuFeO<sub>3</sub>, PuGaO<sub>3</sub>, MgPuO<sub>3</sub>, CdPuO<sub>3</sub>, PbPuO<sub>3</sub> and BePuO<sub>3</sub> although in some cases the tolerance factors are favourable.

TABLE 5  
X-ray powder diffraction data for BaPuO<sub>3</sub>

Preparation 1			Preparation 2		
<i>d</i> <sub>obs.</sub> (Å)	<i>d</i> <sub>obs.</sub> (Å)	<i>I</i>	<i>d</i> <sub>obs.</sub> (Å)	<i>d</i> <sub>obs.</sub> (Å)	<i>I</i>
4.391	4.392	S	4.412	4.412	M
3.118*		VS	3.112	4.406	VS
3.090	4.370	VS	2.717*		W+
2.699*		M-			
2.639		W	2.543	4.404	VVV
2.532	4.386	W	2.198	4.396	M+
2.188	4.376	VS	1.966	4.397	W+
1.954	4.370	M	1.918*		W+
1.908*		M	1.793	4.391	S-
1.787	4.377	VS	1.635*		W+
1.626		M	1.552	4.390	M
1.546	4.373	S	1.464	4.391	W-
1.458	4.375	M	1.388	4.390	M+
1.387		S-	1.354*		
1.381		S-	1.323	4.389	VVV
1.349		VS	1.268	4.393	W
1.321	4.382	W-	1.244*		W
1.265		M-	1.211*		W
1.262		M-	1.714	4.391	M
1.238*		W+	1.105*		W-
1.214	4.376	W-	1.100	4.400	W
1.206*		W			
1.203		W			
1.168		W-			
1.101*		S-			
1.096		W			
1.092		W			
1.062	4.379	W			
1.038*		W+			
1.034		W			
1.030		M-			
0.978	4.373	W+			

\* PuO<sub>2</sub> lines.

Three separate attempts to produce SrPuO<sub>3</sub> yielded specimens which gave almost identical X-ray patterns which were not of cubic symmetry. There were insufficient lines present to determine the structure but the observed *d*-values are listed in table 6.

One "CaPuO<sub>3</sub>" mixture showed some lines in the diffraction pattern besides those from PuO<sub>2</sub> but five further attempts to prepare this substance were unsuccessful. An incidental observation made during these experiments is

that the melting point of 50 m/o PuO<sub>2</sub> 50 m/o CaO is probably between 1500°C and 1550°C.

The last experiment referred to in section 2, intended to produce K<sup>+</sup>Pu<sup>5+</sup>O<sub>3</sub>, gave a product whose X-ray diffraction pattern showed only PuO<sub>2</sub> lines.

A summary of the crystallographic data for those plutonium compounds with perovskite-type structures is included in table 7 together with data for some isostructural compounds for comparison.

#### 4. Discussion of Results

The most recent classification of perovskite-type compounds according to the ionic radii of their constituents is that of Roth<sup>8</sup>. Fig. 2 shows the structure fields suggested by Roth for A<sup>3+</sup>B<sup>3+</sup>O<sub>3</sub> compounds and fig. 3 the structure fields for A<sup>2+</sup>B<sup>4+</sup>O<sub>3</sub> compounds.

The area of fig. 2 which is of direct interest to this investigation is in the lower part of the rhombohedral field and the adjacent ortho-

TABLE 6  
X-ray powder diffraction data for SrPuO<sub>3</sub>

<i>d</i> <sub>obs.</sub> (Å)	<i>I</i>
6.161	W+
5.013	VW
4.302	M-
3.848	VW
3.422	S
3.251	S
3.130*	S
3.073	M+
3.039	S
2.772	M+
2.713	S-
2.145*	VVV
2.093	W-
1.915	S
1.763	W
1.740	M-
1.705	VW
1.675	W
1.633*	M
1.564*	W
1.516	VVV

\* PuO<sub>2</sub> lines.

TABLE 7

A summary of crystallographic data for plutonium perovskite-type compounds with data for some corresponding praseodymium compounds

Compound	Structure of simplest cell	Lattice constants (Å)	Vol. of simplest cell (Å) <sup>3</sup>	X-ray density (g/cm <sup>3</sup> )	Pseudo-cell dimensions
					<i>a</i> (Å) <i>a'</i> (Å) $\alpha$
BaPuO <sub>3</sub>	Cubic	4.39	84.8	8.3	
BaUO <sub>3</sub>	Cubic	4.40	85.2	8.25	
PuMnO <sub>3</sub>	Pseudo-Cubic	3.86	57.5	9.89	
PuVO <sub>3</sub>	Orthorhombic	5.48 5.61 7.78	239	9.41	3.92 3.89 91°31'
PrVO <sub>3</sub>	Orthorhombic	5.48 5.59 7.76	236	6.70	3.89 3.88 90°7'
PuCrO <sub>3</sub>	Orthorhombic	5.46 5.51 7.76	233	9.65	3.88 3.88 90°6'
PrCrO <sub>3</sub>	Orthorhombic	5.44 5.48 7.71	230	6.95	3.86 3.85 90°4'
PrFeO <sub>3</sub>	Orthorhombic	5.49 5.58 7.81	239	6.79	3.91 3.90 90°42'
PuAlO <sub>3</sub>	Rhombohedral	5.33 56°4'	97.4	9.28	3.78 90°24'
PrAlO <sub>3</sub>	Rhombohedral	5.31 60°20'	106	6.73	3.76 90°17'

rhombic field. Recent work by Geller and his co-workers<sup>9</sup>) has confirmed the correct siting of the rhombohedral-orthorhombic boundary. Of some 30 compounds reported by Geller with  $R_A$  between 0.90 Å and 1.10 Å and  $R_B$  between 0.50 Å and 0.85 Å only three, NdAlO<sub>3</sub>, PrAlO<sub>3</sub> and LaAlO<sub>3</sub>, are rhombohedral. The remainder are all orthorhombic.

From fig. 2 it would be predicted that the structures of PuMnO<sub>3</sub>, PuCrO<sub>3</sub> and PuVO<sub>3</sub> should be orthorhombic and that PuAlO<sub>3</sub> should be rhombohedral. Our results show that the first three compounds are orthorhombic and

that at least one sample of PuAlO<sub>3</sub> was rhombohedral. Geller and Bala<sup>10</sup>) showed that PrAlO<sub>3</sub>, like NdAlO<sub>3</sub> and LaAlO<sub>3</sub>, is rhombohedral at room temperature. However, with increase of temperature these aluminates have a tendency to transform to cubic structures, e.g. LaAlO<sub>3</sub> becomes cubic between 350° and 450° C. Geller proposes that if the melting point of PrAlO<sub>3</sub> is greater than 1800° C it might be expected that it would become cubic at about 1800° C. The

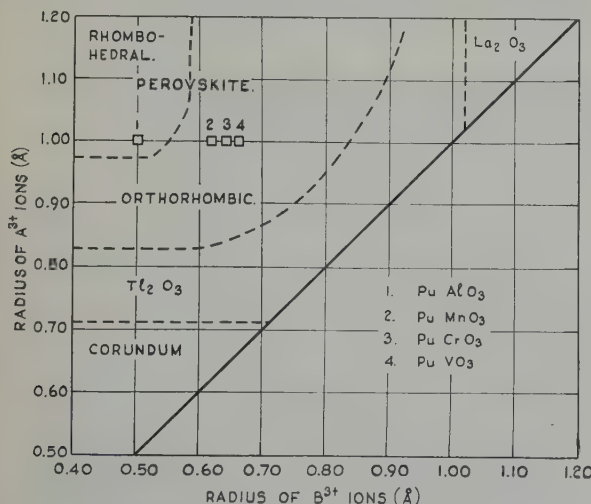


Fig. 2. Structure fields for  $A^{3+} B^{3+} O_3$  compounds.  
(After Roth.)

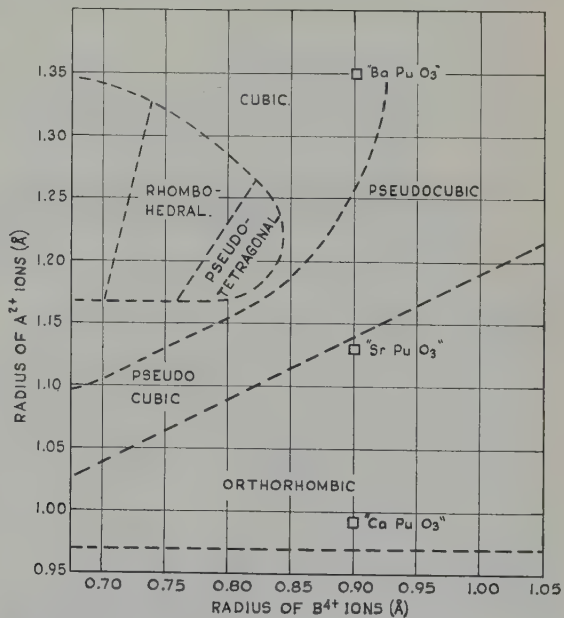


Fig. 3. Structure fields for  $A^{2+} B^{4+} O_3$  compounds.  
(After Roth.)

TABLE 8

Interionic distances and ionic radii in plutonium and praseodymium perovskite-like compounds

Compound	$R_A$ (Å) (C.N.=12)	$R_A+R_O$ (Å)	A-O observed (Å)	$R_A$ from A-O (Å)	$R_B$ (Å) (C.N.=6)	$R_B+R_O$ (Å)	B-O observed (Å)	$R_B$ from B-O (Å)
BaPuO <sub>3</sub>	1.47	3.00	3.10	1.70	0.90	2.30	2.20	0.80
BaUO <sub>3</sub>	1.47	3.00	3.11	1.71	0.93	2.33	2.20	0.80
PuMnO <sub>3</sub>	1.09	2.49	2.73	1.33	0.62	2.02	1.93	0.53
PuVO <sub>3</sub>	1.09	2.49	2.76	1.36	0.66	2.06	1.95	0.55
PrVO <sub>3</sub>	1.09	2.50	2.75	1.35	0.66	2.06	1.94	0.54
PuCrO <sub>3</sub>	1.09	2.49	2.75	1.35	0.64	2.04	1.94	0.54
PrCrO <sub>3</sub>	1.09	2.50	2.73	1.33	0.64	2.04	1.93	0.53
PrFeO <sub>3</sub>	1.09	2.50	2.76	1.36	0.60	2.00	1.95	0.55
PuAlO <sub>3</sub>	1.09	2.49	2.67	1.27	0.50	1.90	1.89	0.49
PrAlO <sub>3</sub>	1.09	2.49	2.66	1.26	0.50	1.90	1.88	0.48

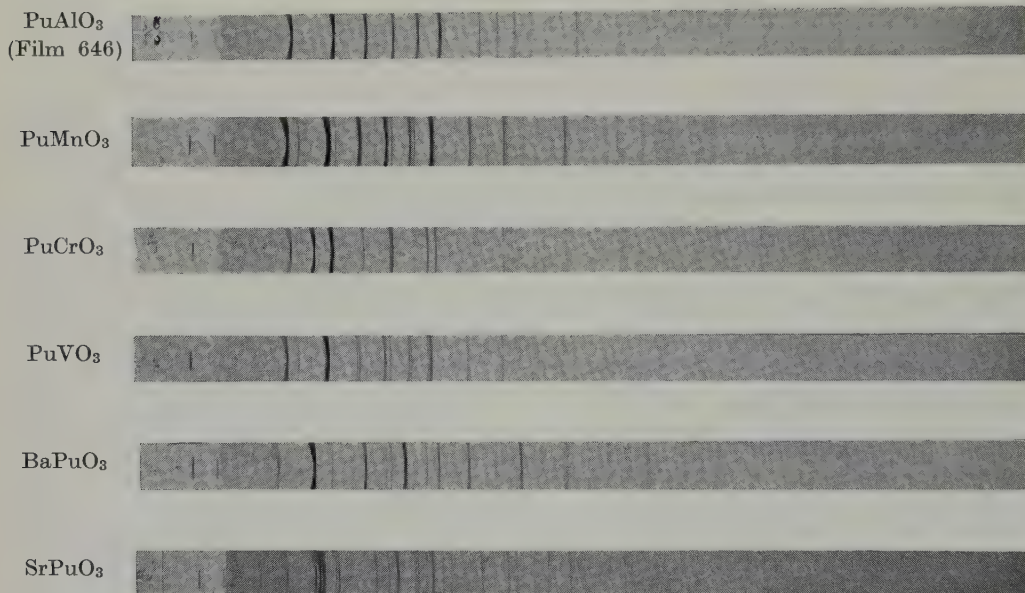


Fig. 4. X-ray powder diffraction patterns of some perovskite-type plutonium compounds.

present investigation indicates that PuAlO<sub>3</sub> is rhombohedral at room temperature, see table 2, and by analogy with PrAlO<sub>3</sub> the various structures of the different PuAlO<sub>3</sub> preparations may have resulted from different firing temperatures and cooling rates.

The striking similarity between corresponding praseodymium and plutonium compounds has been referred to already when the structure of PuVO<sub>3</sub> was solved by comparison with PrFeO<sub>3</sub>. Table 7 compares the cell dimensions of the Pr

and Pu aluminates, vandates and chromates and shows them to be very nearly the same. This is to be expected since the ionic radii of Pr<sup>3+</sup> and Pu<sup>3+</sup> ions are 1.00 Å and 1.013 Å respectively<sup>11</sup>). The dimensions of the pseudo-cubic cell in the orthorhombic compounds<sup>12</sup>) are listed.

In table 8 the lattice parameters of the cubic or pseudo-cubic perovskites are presented for comparison together with the cell sides of the ideal perovskite structures derived from those compounds having orthorhombic symmetry.

Geller<sup>12)</sup> has discussed in detail the relations between the perovskite-like pseudo-cell and the orthorhombic unit cell in similar compounds and in particular in  $\text{GdFeO}_3$ . The edges of the four pseudo-cells which comprise one orthorhombic cell are aligned along the (110), (110) and (001) directions of the orthorhombic cell. The theoretical cell side of the cubic perovskite is calculated as the cube root of the volume of the pseudo-cell.

From these dimensions the effective cationic radii,  $R_A$  and  $R_B$ , and the interionic distances, A-O and B-O, have been computed and these may be compared with the radii quoted by Pauling<sup>4)</sup> and the interionic distances calculated from his figures (table 8). In all cases the observed  $R_A$  and A-O values are larger than the calculated ones and the  $R_B$  and B-O values are slightly smaller. This effect, noticed in many perovskites, may be explained as follows.

The electrostatic bond strengths for A-O and B-O are  $\frac{1}{4}$  and  $\frac{1}{2}$  respectively in  $\text{Pu}^{3+}\text{B}^{3+}\text{O}_3$  and  $\frac{1}{6}$  and  $\frac{2}{3}$  respectively in  $\text{A}^{2+}\text{Pu}^{4+}\text{O}_3$ . Thus the strong bonds here are always the B-O bonds. Now the oxygen ions are in the force fields of both the A and the B ions and consequently the oxygen ions will distribute themselves between these ions such that they occupy the positions of lowest energy. The ions of highest polarizing power, the B ions, will tend to displace the oxygens towards themselves thereby increasing the A-O separation and shortening the B-O distance.

In the calculations of interionic distances and ionic radii for the data in table 8 the figure 1.40 Å was used throughout as the radius of the oxygen ion<sup>4)</sup>. This ion is, in fact, highly polarizable and the assumption of constant radius is purely for purposes of comparison. The minimum O-O distance is actually equal to the A-O distance in the  $\text{Pu}^{3+}\text{B}^{3+}\text{O}_3$  compounds and thus corresponds to oxygen radii which vary from 1.38 Å in  $\text{PuVO}_3$  to 1.34 Å in  $\text{PuAlO}_3$ .

In order to obtain average ionic sizes in perovskite-like compounds Geller<sup>10)</sup> took as a standard the distances in cubic  $\text{LaAlO}_3$  at its transition, which gave a value of 1.346 Å for the radius of the  $\text{O}^{2-}$  ion. When this value is

used, instead of the assumed value of 1.40 Å, the ionic sizes for  $\text{V}^{3+}$ ,  $\text{Cr}^{3+}$  and  $\text{Al}^{3+}$  are found to be 0.60 Å, 0.59 Å and 0.54 Å respectively. These radii are all within 0.025 Å of those reported by Geller<sup>10)</sup>, namely 0.625 Å, 0.608 Å and 0.558 Å.

Using this value for the oxygen ion radius we may obtain a value for the effective radius of  $\text{Pu}^{3+}$  (C.N.=12) in perovskite-type compounds by subtracting this radius from the mean  $\text{Pu}^{3+}\text{-O}^{2-}$  distance in the trivalent compounds. The mean  $\text{Pu}^{3+}\text{-O}^{2-}$  distance is then found to be 2.73 Å and hence the effective radius for  $\text{Pu}^{3+}$  may be taken as 1.38 Å.

The physical and chemical properties of these compounds have not been investigated but some of them may be worthy of consideration as potential reactor fuels. The irradiation behaviour of cubic oxides in general appears to be good and at least one perovskite-type compound,  $\text{BaTiO}_3$ , has satisfactory irradiation characteristics. Crawford and Wittels<sup>14)</sup> found that after an exposure of  $1.8 \times 10^{20}$  nf/cm<sup>2</sup> the cubic perovskite structure had become stabilised in  $\text{BaTiO}_3$ . Thirty minutes anneals at 500°C and 1000°C produced lattice contractions but the cubic structure was retained. It is possible that some of the pseudo-cubic compounds reported here, especially those showing very small deviations from the cubic lattice, would also behave quite satisfactorily under irradiation.

With the exception of "PuMnO<sub>3</sub>" all of the compounds reported here have low neutron absorption cross-sections. They can be prepared by reactions at reasonable temperatures and their melting points are probably in excess of 1500°C. At least one compound,  $\text{BaPuO}_3$ , is stable in oxidising atmospheres up to 1500°C and being isostructural with  $\text{BaUO}_3$ <sup>13)</sup> would probably form a continuous series of solid solution with it.

## 5. Conclusions

1. Perovskite-type compounds based on  $\text{Pu}^{3+}$  and  $\text{Pu}^{4+}$  can be prepared by reacting mixed oxides under reducing and oxidising conditions respectively.

2. The compounds  $\text{PuVO}_3$  and  $\text{PuCrO}_3$  are orthorhombic and isostructural with  $\text{PrFeO}_3$ .  $\text{PuAlO}_3$  is probably rhombohedral at room temperature and  $\text{BaPuO}_3$  is cubic. The  $\text{PuMnO}_3$  structure has not been solved but it appears to deviate very little from cubic.

3. The structures of these compounds fall in the correct fields of the diagrams produced by Roth.

4. The effective oxygen ion radius in plutonium compounds having a perovskite-type structure is about 1.38 Å.

### Acknowledgements

The authors wish to acknowledge their debt to those members of the Metallurgy and Chemistry Divisions at AERE who helped them with the interpretation of the X-ray patterns and to R. G. Taylor, A. L. Bailey and K. D. W. Smith who assisted in the preparation of the compounds.

### References

- 1) H. D. Megaw, *Ferroelectricity in Crystals* (Methuen & Co. Ltd., 1957)
- 2) H. D. Megaw, *Proc. Phys. Soc.* **58** (1946) 133
- 3) A. F. Wells, *Structural Inorganic Chemistry* 2nd Ed. (Clarendon Press, Oxford, 1950)
- 4) L. Pauling, *Nature of the Chemical Bond* 2nd Ed. (Cornell Univ. Press, 1945)
- 5) W. H. Zachariasen, Chapter 18 in *The Actinide Elements*. (National Nuclear Energy Series), Div. IV, 14A (1954)
- 6) G. K. Williamson, D. M. Poole and J. A. C. Marples, UKAEA (Harwell) Report, AERE M/R 1390 (1956)
- 7) S. Geller and E. A. Wood, *Acta Cryst.* **9** (1956) 563
- 8) R. S. Roth, *J. Res. Nat. Bur. Stand.* **58** (1957) 75
- 9) S. Geller, *Acta Cryst.* **10** (1957) 243
- 10) S. Geller and V. B. Bala, *Acta Cryst.* **9** (1956) 1019
- 11) D. H. Templeton and C. H. Dauben, *J. Am. Chem. Soc.* **76** (1954) 5237
- 12) S. Geller, *J. Chem. Phys.* **24** (1956) 1236
- 13) S. M. Lang, F. P. Knudsen, C. L. Fillmore and R. S. Roth, *National Bureau of Standards, Circular* **568** (1956)
- 14) J. H. Crawford and M. C. Wittels, 2nd Geneva Conference, P/679 (1958)

## HYDROGEN IN ZIRCALOY-2: ITS DISTRIBUTION AND HEAT OF TRANSPORT

A. SAWATZKY

*Atomic Energy of Canada Limited, Chalk River, Ontario, Canada*

Received 19 April 1960

Two determinations of the heat of transport for hydrogen in zircaloy-2 have been made under steady-state conditions over the temperature range 300° to 500° C. Values of 4.7 and 6.1 kcal/mole were obtained.

Similar experiments on deuterium gave values of 6.2 and 6.8 kcal/mole.

An equation has been developed giving the hydrogen concentration in the two-phase (alpha plus hydride) region as a function of time and temperature. On the basis of this equation, a model for the over-all hydrogen distribution under the influence of a temperature gradient is proposed. The model has been fitted to several experimental curves and the agreement found to be very good. The model predicts that for hydrogen pickup on the hot surface (as in a failure of a fuel-rod sheath) maximum hydriding will occur at some position displaced from the cold surface. This prediction is supported by observations made on a failed zircaloy-2-clad UO<sub>2</sub> fuel element.

Deux déterminations de la chaleur de transport pour l'hydrogène dans le zircaloy-2 ont été effectuées dans l'intervalle de températures 300-500° C dans des conditions de régime permanent. Les valeurs de 4,7 et 6,1 kcal/mol ont été trouvées.

Des expériences similaires avec le deutérium donnèrent des valeurs de 6,2 et 6,8 kcal/mol.

Une équation a été déterminée reliant la concentration en hydrogène dans le domaine biphasé ( $\alpha$  + hydrure) au temps et à la température. En se basant sur cette équation, on propose un modèle représentant la distribution de l'hydrogène total sous l'influence

d'un gradient de température. Le modèle a été appliqué à plusieurs courbes expérimentales et l'accord trouvé très satisfaisant. Ce modèle prédit que dans le cas de l'absorption d'hydrogène sur une surface chaude (cas de la rupture d'une gaine) l'hydratation maximum se produira dans une position déplacée vis-à-vis de la surface froide. Cette prévision est confirmée par les observations faites sur des ruptures de gaine d'éléments combustibles UO<sub>2</sub> gainés au zircaloy-2.

Im Temperaturbereich von 300 bis 500° C wurden zwei Bestimmungen der Transportwärme von Wasserstoff in Zircaloy-2 durchgeführt, wobei Werte von 4,7 und 6,1 kcal/mol erhalten wurden. Gleichtartige Messungen an Deuterium ergaben Werte von 6,2 und 6,8 kcal/mol.

Eine abgeleitete Gleichung gibt den Zusammenhang zwischen der Wasserstoffkonzentration im Zweiphasenbereich ( $\alpha$  + Hydrid) und Temperatur und Zeit an. Hierzu ausgehend wird ein Modell für die gesamte Wasserstoffverteilung unter dem Einfluss eines Temperaturgradienten entwickelt. Das Modell wurde verschiedenen Messkurven angepasst, wobei sich eine sehr gute Übereinstimmung erzielen liess. Nach diesem Modell liegt bei Aufnahme von Wasserstoff an einer heißen Oberfläche (etwa an einer Schadenstelle in der Hülle eines Brennelementes) die höchste Wasserstoffkonzentration in einigem Abstand von der kalten Oberfläche vor. Diese Voraussage wird durch Beobachtungen gestützt, welche an UO<sub>2</sub>-Brennelementen mit beschädigten Hüllen aus Zircaloy-2 zu machen waren.

### 1. Introduction

One of the problems associated with the use of zircaloy-2-clad UO<sub>2</sub> fuel elements in pressurized-water power reactors is that zircaloy-2 picks up hydrogen during operation. Because precipitates of zirconium hydride in zircaloy-2 can have pronounced effects on the mechanical

properties it is important to know how the hydrogen redistributes itself during operation.

It has been shown<sup>1)</sup> that under the influence of a temperature gradient, hydrogen in zircaloy-2 will tend to move to the colder regions until a steady-state distribution, determined by the so-called heat of transport, is attained. Shew-

mon<sup>2</sup>) has qualitatively discussed thermal diffusion and arrived at an expression for the hydrogen current in the two-phase region. From this he was able to calculate the time to steady state. The hydrogen distribution as a function of time and position, however, has never been carefully considered.

In the present investigation the heat of transport for both hydrogen and deuterium has been determined. An expression for the hydrogen distribution has been developed and applied to several experimental curves. The practical case of hydrogen pickup at a hot surface, as in a fuel-sheath failure, is treated mathematically and the result used to explain the hydride distribution found in an actual sheath failure.

## 2. The Distribution Equation

The model used for thermal diffusion in the two-phase region is basically the one proposed by Shewmon<sup>2</sup>). The assumptions made are as follows:

1. Hydrogen is the only component diffusing.
2. The hydride is in equilibrium with the solid solution at every point in the two-phase region. As the diffusing current increases, this assumption becomes less reliable.
3. Diffusion is predominantly in the solid-solution (alpha) phase. This implies a large ratio of hydrogen diffusivity in the alpha phase to that in the hydride as well as a small ratio of hydride volume to alpha-phase volume.

With these assumptions, thermal diffusion in the two-phase region can be treated as diffusion in the single phase with the concentration fixed at each point, the hydride serving merely as a source or sink for hydrogen.

In the presence of a temperature gradient the atomic diffusion flux in the single-phase region  $J$ , is given by Denbigh<sup>3</sup>) as

$$J = \frac{-DN}{RT} \left\{ RT \frac{d \ln N}{dx} + \frac{Q^*}{T} \frac{dT}{dx} \right\} \quad (1)$$

where  $D$  is the diffusion coefficient,  $N$  the hydrogen concentration,  $T$  the temperature in °K,  $R$  the gas constant, and  $Q^*$  the heat of transport.

Since the solid solution at every point in the

two-phase region is assumed to be in equilibrium with the hydride at the corresponding temperature

$$N = N_s = N_0 \exp(-\Delta H/RT) \quad (2)$$

where  $N_s$  is the terminal solid solubility,  $N_0$  a constant, and  $\Delta H$  the heat of mixing.

Substituting (2) into (1) leads to

$$J = \frac{-DN_s}{RT^2} (\Delta H + Q^*) \frac{dT}{dx} \quad (3)$$

the flux equation originally obtained by Shewmon<sup>2</sup>).

The diffusion coefficient is given by the Arrhenius-type expression

$$D = D_0 \exp(-Q/RT) \quad (4)$$

where  $D_0$  is the frequency factor and  $Q$  the activation energy for diffusion.

For the case of a constant temperature gradient

$$dT/dx = K. \quad (5)$$

Eqs. (2), (4) and (5) substituted in (3) lead to

$$J = \frac{-D_0 N_0 K}{RT^2} (\Delta H + Q^*) \exp - \left( \frac{\Delta H + Q}{RT} \right). \quad (6)$$

In one-dimensional flow, which is considered here, the continuity equation is given by

$$\frac{\partial N}{\partial t} = -\frac{\partial J}{\partial x} = -\frac{K \partial J}{\partial T} \quad (7)$$

where  $\partial N/\partial t$  is the variation with time of the total hydrogen concentration at point  $x$ . Since the hydrogen concentration in the solid solution is independent of time,  $\partial N/\partial t$  is the rate of change of the hydride concentration.

Differentiating (6) with respect to  $T$  and substituting into (7) leads to

$$\frac{\partial N}{\partial t} = \frac{K^2 D_0 N_0 (\Delta H + Q^*)}{RT^4} \left. \left( \frac{(\Delta H + Q)}{R} - 2T \right) \exp - \left( \frac{\Delta H + Q}{RT} \right) \right\} \quad (8)$$

which on integration becomes

$$N - N_I = \frac{K^2 D_0 N_0 (\Delta H + Q^*)}{RT^4} \left. \left( \frac{(\Delta H + Q)}{R} - 2T \right) \cdot t \cdot \exp - \left( \frac{\Delta H + Q}{RT} \right) \right\} \quad (9)$$

where  $N_I$  is the initial hydrogen concentration.

### 3. Hydrogen Redistribution

#### 3.1. NO HYDROGEN PICKUP

If hydrogen is uniformly distributed throughout the material and a temperature gradient applied such that the hydrogen concentration over at least part of the system is greater than terminal solid solubility, the initial situation is represented by fig. 1a. The temperatures at the cold and hot surfaces are  $T_c$  and  $T_h$  respectively.  $T_0$  is the temperature at the initial position of the interface between the single-phase region and the two-phase region (hereafter simply stated as interface).  $N_I$  is the initial uniform hydrogen concentration and  $N_s$  the terminal solid solubility, so that the hydride concentration is given by the shaded area.

According to eq. (9) the hydride concentration at any point within the two-phase region increases linearly with time, the rate of hydriding being greater the higher the temperature. Singularities in  $J$  exist at the cold surface and at the interface as shown by the discontinuities in the alpha-phase concentration gradient at these points. Eq. (9) therefore does not apply at these points and a separate treatment must be given.

The hydrogen flow into the cold surface is given by  $J(T_c)$  in (6). Since no hydrogen leaves the surface a layer of zirconium hydride is formed, whose thickness is given by

$$X = \frac{J(T_c) \cdot t}{N_H} \quad (10)$$

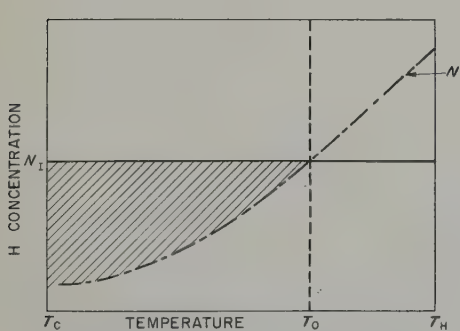


Fig. 1a. Initial hydrogen distribution, showing single-phase and two-phase regions.

where  $N_H$  is the hydrogen concentration in zirconium hydride.

The time to steady state is given approximately as the time required for all the hydrogen to be precipitated out as hydride at the cold surface, namely

$$t_E = \frac{N_I \cdot l}{J(T_c)} \quad (11)$$

where  $l$  is the thickness of the specimen. This is the limiting case of the more general expression due to Shewmon<sup>2</sup>.

The diffusion rate is greater the higher the temperature, so that in the single-phase region a "near" steady state hydrogen distribution will first be achieved in the hotter regions. To conserve hydrogen a maximum in hydrogen concentration must be built up somewhere in the single-phase region. The position of the maximum will determine the slope of the single-phase hydrogen distribution at the interface. This slope can be either less or slightly greater than the slope of the terminal solid solubility curve at this point.

Since hydrogen is conserved, the application of equation (1) to both sides of the interface will indicate the direction in which the interface moves. It can move either towards the hot or cold surface depending on whether the hydrogen concentration gradient in the single-phase region is greater or less than that in the alpha phase of the two-phase region.

On the basis of the preceding discussion the interface initially moves toward the colder surface. As hydrogen redistribution in the

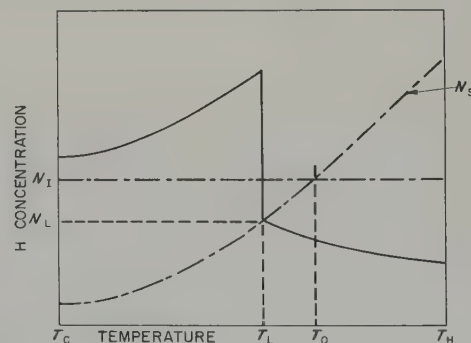


Fig. 1b. Hydrogen distribution sometime before steady state has been achieved.

single-phase region proceeds the hydrogen concentration peak moves toward the interface. This could lead to, although not necessarily, an interface movement toward the hotter surface. Eventually, however, as the concentration maximum disappears at the interface, the latter must again move towards the colder surface.

Since every point in the two-phase region gains hydrogen at a constant rate and the hydrogen concentration in the single-phase region at the interface decreases as it moves toward the colder surface, a sharp discontinuity in concentration will result as shown in fig. 1b.

The diffusion coefficient at every point in the single-phase region is higher than at any point in the two-phase region so that one might expect near steady-state conditions to exist in the single-phase region before the interface reaches the colder surface. The hydrogen distribution in the single-phase area may then be obtained by setting  $J=0$  in eq. (1) and integrating. This leads to

$$N = C_0 \exp \frac{Q^*}{RT} \quad (12)$$

where  $C_0$  a constant.

### 3.2. HYDROGEN PICKUP AT THE COLD SURFACE

For the case under consideration, namely a two-phase region over part of the system, hydrogen pickup at the cold surface, as in a fuel sheath during normal reactor operation, will lead to a more rapid growth of the surface hydride layer. It will not, however, affect the distribution in either the single- or two-phase regions.

### 3.3. HYDROGEN PICKUP AT THE HOT SURFACE

Hydrogen pickup at the hot surface, as in the case of a defected fuel-rod sheath, will in general result in a decrease of the rate at which the interface moves to the cold surface. It may be shown, however, that for a range of rate of hydrogen pickup the interface will remain fixed in position. If the interface is fixed and  $J_0$  is the hydrogen current, constant throughout the

single-phase region, then (6) leads to

$$J_0 = \frac{-D_0 N_0 K (\Delta H + Q^*)}{RT_L^2} \exp - \left( \frac{\Delta H + Q^*}{RT_L} \right). \quad (13)$$

$J_0$  must have a value such that in the above equation  $T_C < T_L < T_H$ . It may also be seen from (13) that for a given temperature gradient the interface is found closer to the hot surface as  $J_0$  increases.

### 4. Experimental Technique

The thermal diffusion specimens were cylinders of reactor grade zircaloy-2, 1.2 cm in diameter and 2.5 cm in length. Hydrogen was introduced into the specimen by heating at 900°C in a closed system containing the required amount of hydrogen. A six hour anneal led to a homogeneous hydrogen distribution. The specimen was removed from the system and heated in air for several minutes to form an oxide layer relatively impermeable to hydrogen. It was then bolted into position between a stainless steel cylinder and a brass plate. The stainless steel cylinder was heated in a nichrome wound tube furnace and served as heat source for the specimen. The brass plate had brazed to it on the side opposite to the specimen, a brass rod coaxial to the latter. A watercooled coil could be slid along the rod permitting the cold-end temperature of the specimen to be adjusted to the desired value. Glass wool was wrapped around the specimen to reduce heat losses through the surface. The temperatures at each end of the specimen were continuously monitored and showed a maximum variation of  $\pm 3^\circ\text{C}$ . A preliminary run with five chromel-alumel thermocouples equally spaced along the specimen indicated a constant temperature gradient.

After sufficient time (several weeks) at temperature to give the desired hydrogen distribution, the specimen was removed and cut into discs 0.1 cm thick. These were analyzed for hydrogen by the hot-extraction method, and the hydrogen distribution determined.

## 5. Experimental Results

Two thermal-diffusion runs were made to determine the heat of transport for hydrogen in zircaloy-2. The hot and cold ends of the specimens were held at 500° and 300° C. An initial uniform hydrogen concentration of 60 ppm by weight left the specimens completely in the solid solution (alpha) phase. Each experiment was continued for 44 days, this being calculated as sufficient time to arrive at the steady-state hydrogen distribution. The data for the two runs are plotted in fig. 2.

According to eq. (1), for  $J=0$  (i.e. steady state)

$$\frac{d \ln N}{d(1/T)} = \frac{Q^*}{R}. \quad (14)$$

Values for  $Q^*$  of 4.7 and 6.1 kcal/mole were obtained from the slopes of curves A and B respectively, using the method of least squares.

The heat of transport for deuterium in

zircaloy-2 was also measured. Two 62-day runs were made on specimens having an initial deuterium concentration of approximately 120 ppm by weight. The hot and cold ends of the specimen were held at 460° and 300° C. The data for the two runs are plotted in fig. 3. Values for  $Q^*$  of 6.2 and 6.8 kcal/mole were obtained from the slopes of curves C and D.

The scatter in curve B fig. 2, is believed to be due to the fact that the oxide skin was left on the specimen during hydrogen analysis. A comparison of the total hydrogen present in the specimen before and after the thermal diffusion anneal, showed that a small amount of hydrogen (about 2 percent of the initial concentration) had been picked up. Based on uncertainties in concentration, temperature, and thermocouple position, an observational error in the heat of transport of  $\pm 15\%$  is considered a reasonable estimate.

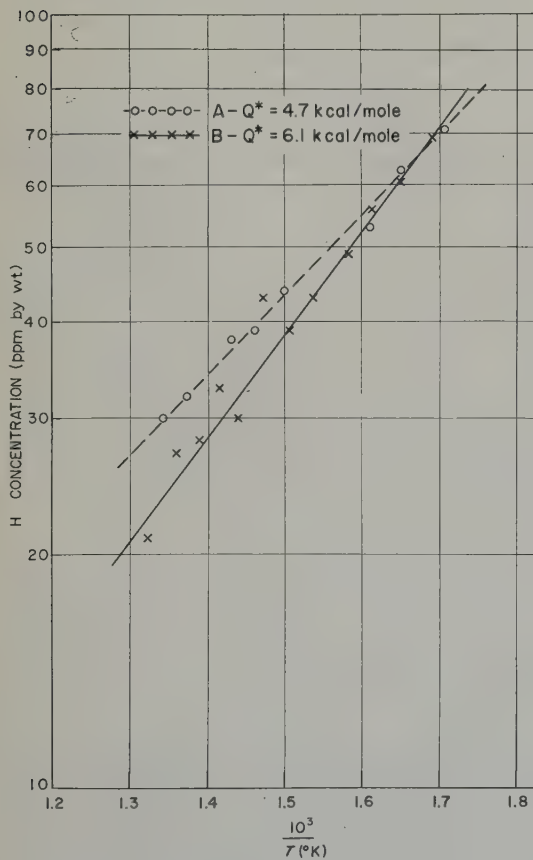


Fig. 2.  $\ln$  hydrogen concentration vs  $1/T$ .

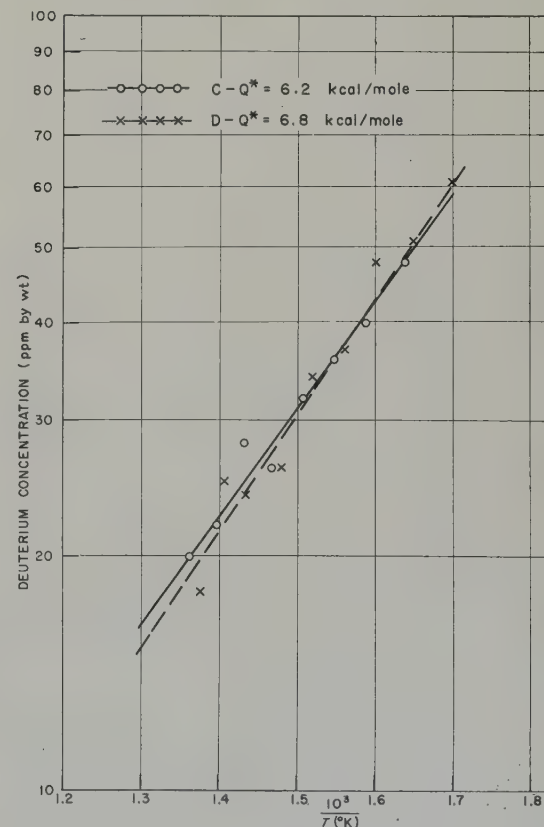


Fig. 3.  $\ln$  deuterium concentration vs  $1/T$ .

Two further thermal-diffusion runs for hydrogen in zircaloy-2 were made for times too short to allow the hydrogen to reach a steady-state distribution. One specimen, having an initial uniform hydrogen concentration of 130 ppm by weight, had hot and cold ends at 477° and 130° C. The points in fig. 4 give the experimental hydrogen distribution after a 34-day anneal. The other specimen had an initial hydrogen concentration of 64 ppm with hot and cold ends at 454° and 157° C. The hydrogen distribution after a 41-day anneal is given by the points in fig. 5. A heat of transport

of 4.3 and 3.8 kcal/mole was estimated from the single-phase regions of figs. 4 and 5 respectively.

## 6. Discussion of the Results

The heat of transport for hydrogen in zircaloy-2, as obtained in the present investigation, varies between 3.8 and 6.1 kcal/mole. Values ranging from 1.6 to 6.5 kcal/mole have been reported by Markowitz<sup>4</sup> and a value of 6.4 kcal/mole has been reported by Johnston *et al.*<sup>5</sup>. The range of values found in the present work and in that of Markowitz<sup>4</sup> is greater than

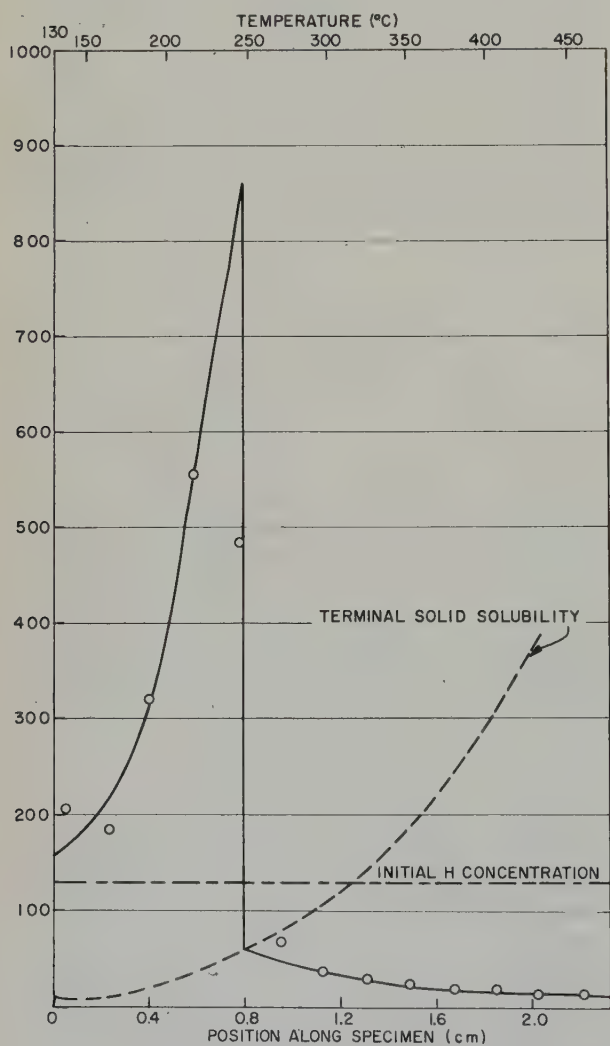


Fig. 4. Hydrogen distribution in zircaloy-2 after a 34-day anneal under a temperature difference 130°-477° C.

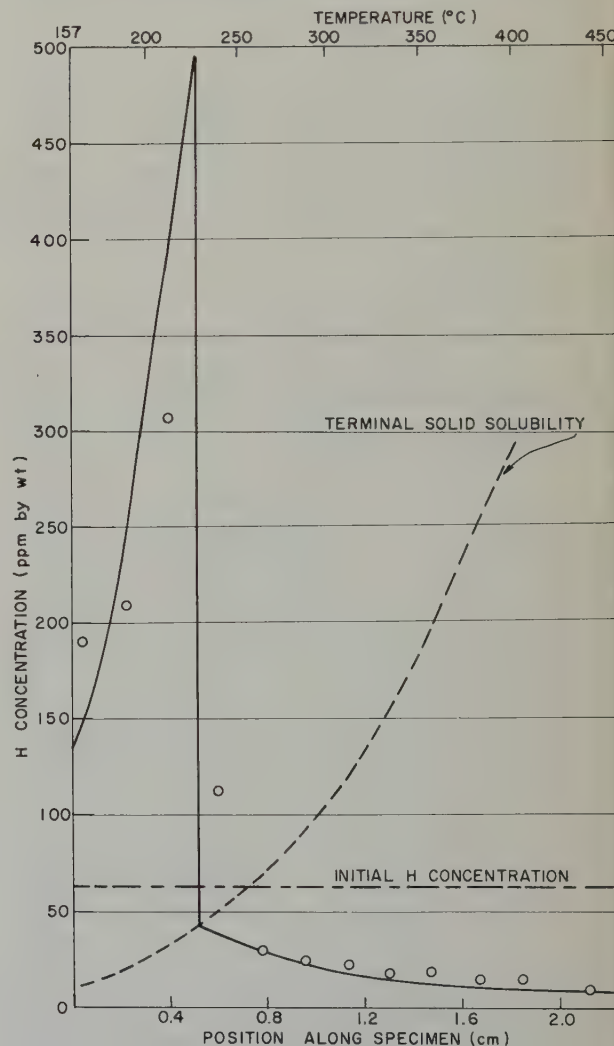


Fig. 5. Hydrogen distribution in zircaloy-2 after a 41-day anneal under a temperature difference 157°-454° C.

that which could be attributed to errors in measurement alone. It is suggested that a large contributing factor to the spread in values is insufficient time at temperature to arrive at the steady-state hydrogen distribution. This contention is supported by the fact that the short anneals (figs. 4 and 5) led to lower values for the heat of transport than long anneals (fig. 2). Hydrogen pickup during the experiment could also lead to a hydrogen distribution different from that of the true steady-state distribution. Both of these effects would in general result in an apparent  $Q^*$  smaller than the true value. It may be significant that the maximum values for the heat of transport obtained in the three independent investigations (6.1, 6.4 and 6.5 kcal/mole) fall well within the experimental error. On the basis of the foregoing, it is therefore felt that the heat of transport for hydrogen in zircaloy-2 is about 6.0 kcal/mole.

The heat of transport for deuterium in zircaloy-2, taken as the average of the two results from fig. 3, is 6.5 kcal/mole. Since the activation energies for the diffusion of hydrogen and deuterium are equal<sup>6</sup>, one might expect the heats of transport to be the same; this seems to be the case. Because of experimental error, however, differences of less than about 20 % in the heats of transport would not be detected.

In figs. 4 and 5 the experimental hydrogen distributions are compared with the theoretical ones as obtained from eqs. (9) and (12). The experimental hydrogen concentration is given by the points, the theoretical distribution by the solid line, and the terminal solid solubility by the dotted curve. The theoretical hydrogen distribution in the two-phase region was determined from eq. (9) using  $D_0 = 2.17 \times 10^{-3}$  cm<sup>2</sup>/sec;  $N_0 = 8.5 \times 10^4$  ppm by wt;  $\Delta H = 7.6$  kcal/mole;  $Q = 8.3$  kcal/mole; and  $Q^* = 6.0$  kcal/mole. The first four quantities are those found from measurements of the terminal solid solubility and diffusion of hydrogen in zircaloy-2<sup>7</sup>. The theoretical hydrogen distribution in the single-phase region was obtained by choosing an experimental point near the concentration discontinuity and adjusting  $C_0$  in eq. (12) to

pass through it. The point at which the concentration on this curve corresponded to terminal solid solubility was taken as the position of the discontinuity. This treatment accounted for any hydrogen picked up during the experiment.

The agreement between experiment and theory is seen to be good in both figs. 4 and 5, implying that within the range of hydrogen concentration encountered in the experiments the assumptions made in the model are valid. Since no normalization factor was employed in fitting the theoretical curve to the experimental points in the two-phase region, the good agreement, not only in the shape of the curve but also in absolute value, attests to the accuracy of the diffusivity and solubility values used in the calculation.

Markowitz<sup>1</sup>) has reported a thermal-diffusion experiment with hydrogen in zircaloy-2 where the colder portion of the specimen was in the alpha-hydride region. The hydrogen-distribution curve obtained by Markowitz (fig. 6) is relatively

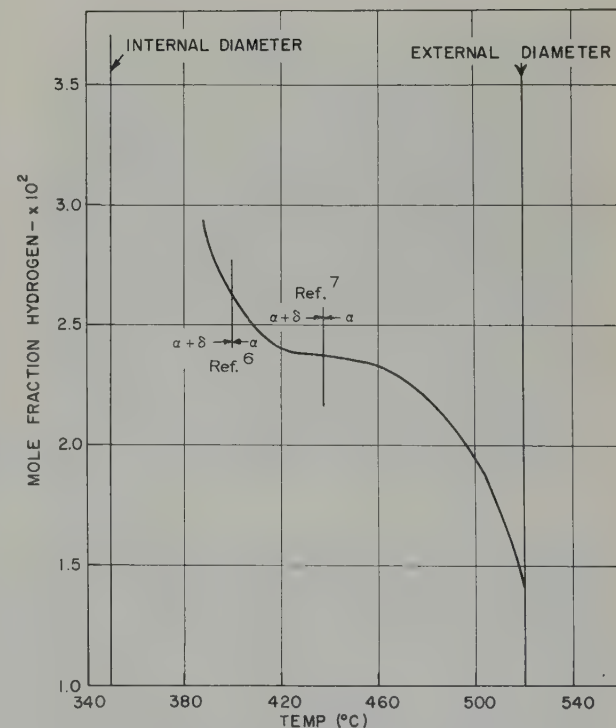


Fig. 6. Hydrogen distribution in internally cooled zircaloy-2 cylinder under a thermal gradient.  
(J. M. Markowitz.)

smooth with an indication of a sharp increase in hydrogen concentration near the cold surface of the specimen. However, in contrast to the results presented in figs. 4 and 5, the interface between the single- and two-phase regions, using Gulbransen's<sup>8</sup> results for the terminal solubility of hydrogen in pure zirconium, falls on the smooth portion of the curve of concentration vs temperature. If the latest values for the terminal solid solubility of hydrogen in zircaloy-2<sup>7</sup>) are used to establish the position of the interface, it is seen (fig. 6) to fall at the point of sharply increasing hydrogen concentration; this is in agreement with the results of the present investigation.

In section 3.3 it was predicted that in the case of a defected zircaloy-2 fuel element, where corrosion on the hot inner sheath surface can occur, the position of maximum hydriding may be fixed at a distance from the cold surface depending on the rate of hydrogen pickup. This effect is illustrated in fig. 7 which is a photo-

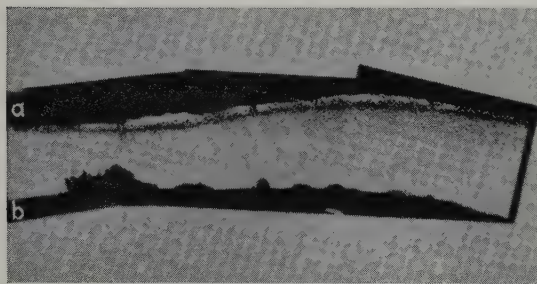


Fig. 7. Section through X-2-g sheath failure after 40 days' testing under a heat flux of 100 watt/cm<sup>2</sup>.

Coolant water at 965 psi and 250°–277° C.

(T. J. Kisiel.)

(a) External cool surface. (b) Internal hot surface.

micrograph of a section near a defect in the zircaloy-2 cladding of a UO<sub>2</sub> fuel element which had been irradiated in a high-pressure, high-temperature loop<sup>9</sup>). The maximum sheath thickness was 0.070 cm with the inner and outer surface temperatures being approximately 270° and 330° C respectively. The region of heaviest hydriding is roughly 0.01 cm from the cold surface opposite the area of maximum

corrosion on the hot surface. As predicted in section 3.3 this region moved toward the cold surface with increasing distance from the area of heaviest corrosion and presumably maximum rate of hydrogen pickup. It should be pointed out that the photomicrograph was taken from a polished section after cooling to room temperature. Since the cooling rate of the specimen was relatively slow (several hours to reach room temperature), a lot of the hydrogen in the single-phase region would have precipitated out. This accounts for the hydride platelets between the heavily hydrided band and the inner sheath surface.

### Acknowledgments

Thanks are due to Mrs. M. Rees who assisted with the experimental work. The author is also indebted to various members of the Research Metallurgy Branch and to Dr. E. Vogt of the Theoretical Physics Branch for helpful discussions during the course of the work. Acknowledgment is gratefully given to Mr. E. C. W. Perryman for suggesting the problem and for his guidance during the course of the investigation.

### References

- 1) J. M. Markowitz, *Westinghouse Atomic Power Division* (USA) Report, WAPD-TM-104 (1958)
- 2) P. G. Shewmon, *Trans. Met. Soc. AIME* 212 (1958) 642
- 3) K. G. Denbigh, *The Thermodynamics of the Steady State* (Methuen & Co. Ltd., London, 1951)
- 4) J. M. Markowitz, *Westinghouse Atomic Power Division* (USA) Report, WAPD-TM-171 (1959)
- 5) W. V. Johnston, W. R. Jacoby, J. S. Wallam and A. H. Alberts, *Knolls Atomic Power Laboratory*, (USA) Report, KAPL-2000-5 (1959)
- 6) E. A. Gulbransen and K. F. Andrew, *J. Electro-chem. Soc.* 101 (1954) 560
- 7) A. Sawatzky, *Atomic Energy of Canada Ltd. publication*, AECL Report CRMet-826 (1959)
- 8) E. A. Gulbransen and K. F. Andrew, *Trans. Met. Soc. AIME* 203 (1955) 136
- 9) T. J. Kisiel, *Westinghouse Atomic Power Division*, (USA) Report, WAPD-PWR-PMM-1149 (1957)

## ON THE LOCATION AND MOTION OF RARE GAS ATOMS IN METALS

C. W. TUCKER, Jr. and F. J. NORTON

*General Electric Research Laboratory, Schenectady, N.Y., USA*

Received 13 April 1960

Using potentials of about 40 kV, rare gas ions were accelerated into metal films and foils. In spite of the fact that as much as 2 at % argon was loaded into the metal lattice, little or no X-ray effect due to lattice distortion was observed. This result suggests that rare gas atoms coming to rest in a metal lattice capture vacancies. When rare gas loaded metal foils are heated in a vacuum system connected to a mass spectrometer, the evolution of the gas can be measured. The evolution of argon from foils of silver, gold, aluminum, and lead and krypton from uranium has been studied with interesting variations from metal to metal. Exploratory experiments with other rare gases indicate similar results. The combination of the ion bombardment and mass spectrometer techniques appears very promising for the study of the behaviour of rare gases in crystals.

---

En utilisant des potentiels d'environ 40 kV, des ions de gaz rares ont été accélérés dans des films et des feuilles métalliques.

Bien qu'il y ait alors au moins deux atomes % d'argon fixés dans le réseau du métal, on n'a observé peu ou aucun effet sur le diagramme de R.X. dû à une déformation du réseau. Ce résultat suggère que les atomes de gaz rare qui viennent se fixer dans le réseau du métal capturent des lacunes.

On peut mesurer la désorption des gaz quand les feuilles de métal chargées en gaz rare sont chauffées dans une enceinte sous vide, reliée à un spectromètre de masse. La désorption de l'argon a été étudiée avec

des lames d'argent, d'or, d'aluminium et de plomb et celle du krypton avec l'uranium: les résultats diffèrent d'une façon intéressante d'un métal à l'autre.

Des résultats identiques ont été obtenus au cours de quelques expériences avec d'autres gaz rares. L'association des techniques de bombardement ionique et du spectromètre de masse apparaît encourageante pour l'étude du comportement des gaz rares dans les cristaux.

Mit einer Beschleunigungsspannung von etwa 40 kV wurden Edelgasatome in Metallfilme und -folien eingeschossen. Obwohl dabei das Metallgitter mit einer Konzentration von 2 At % Argon beladen wurde, konnten durch Röntgenstrahlen nur geringe oder gar keine Effekte festgestellt werden, welche auf eine Gitterdeformation hinweisen. Daraus ist zu schliessen, dass die Edelgasatome von Leerstellen des Metallgitters eingefangen werden.

Die Entgasung der Metallfolien konnte gemessen werden, indem zuvor begastete Folien in einer Vakuumapparatur aufgeheizt wurden, an welche ein Massenspektrometer angeschlossen war. Beim Studium der Abgabe von Argon aus Silber-, Gold-, Aluminium- und Bleifolien und von Krypton aus Uran ergaben sich interessante Unterschiede zwischen den einzelnen Metallen. Orientierende Experimente mit anderen Edelgasen führten zu ähnlichen Ergebnissen. Die gemeinsame Anwendung von Ionenbeschuss und Massenspektrometrie scheint sehr aussichtsreich für das Studium des Verhaltens von Edelgasen in Kristallen zu sein.

### 1. Introduction

The X-ray effects reported by Tucker and Senio <sup>1,2)</sup> caused by point defects in neutron irradiated high melting point crystals such as boron carbide and diamond led one of us (C.W.T.) to an attempt to produce and study similar X-ray effects in metals using rare gas atoms as atomic sites of high distortion. Such

X-ray effects have not been observed in metals except in the solid solution case <sup>3,4)</sup>. In this case the diffuse scattering effect, which contains most of the information of interest, is very weak due to the relatively low distortion of atoms which can be put in solid solution. With high distortion defects such as interstitials there is difficulty in building up large concentrations (1 to 2 at %)

due to their high mobility in metals at room temperature. The idea behind the present work was that a single-crystal metal film formed by epitaxial growth might be loaded with 1 to 2 at % of atomically dispersed rare gas atoms by ion bombardment using energies of the order of 50 kV. The range of such ions depends, of course, on the bombarding and matrix species, but within a factor of two is about 300 Å in typical cases<sup>5,6</sup>). Since X-ray work can be conducted on metal films as thin as 500 Å, it was clear that, provided the rare gas atoms did not agglomerate or capture vacancies as they came to rest, it was likely that the desired X-ray effects would be observed for those rare gases for which size mismatches of the order of 35 % obtain.

## 2. Experimental Procedure

Equipment was built for the experiment, the main item of interest probably being the ion accelerator shown in fig. 1. It was fashioned after one described by Heinz, Gyorgy and Ohl<sup>7</sup>). The sample, either a deposited metal film on its substrate or in the later work a 2 mil metal foil, was placed on the stand which was grounded. Underneath the stand is a spiral filament for heating during outgassing prior to a bombardment. The two grids and filaments of the anode assembly were all maintained at high positive potential by means of a high voltage power supply to cover the range of 5 to 50 kV. The grids were about 16 mesh. The filaments were heated by current from storage batteries and the biasing potentials for the two grids were supplied by dry cells. Best operation was obtained when the upper grid was maintained at +135 volts and the lower at -90 volts. The batteries for the filaments and grids floated at the potential of the supply through 300 megohms. During a bombardment the system was continuously pumped and a rare gas flow established which would maintain a pressure of 1.0 to  $1.5 \times 10^{-4}$  mm of Hg. Under these conditions a net current was established of about  $2\mu$  A/cm<sup>2</sup>. Of course this current includes both the positive ion current and the secondary electron current.

From the amount of gas imbedded by the bombardment, it is estimated that the positive ion current due to the retained ions was approximately  $0.02 \mu$  A/cm<sup>2</sup>.

There were two limiting cases for which the ion accelerator did not operate. When the rare gas flow was too small, the gas was cleaned up and when the gas flow was too high, a gaseous discharge resulted. Between these two extremes the system could be operated stably for periods of the order of 30 minutes to an hour by monitoring the gas flow with the total current to ground. The stable operation was further

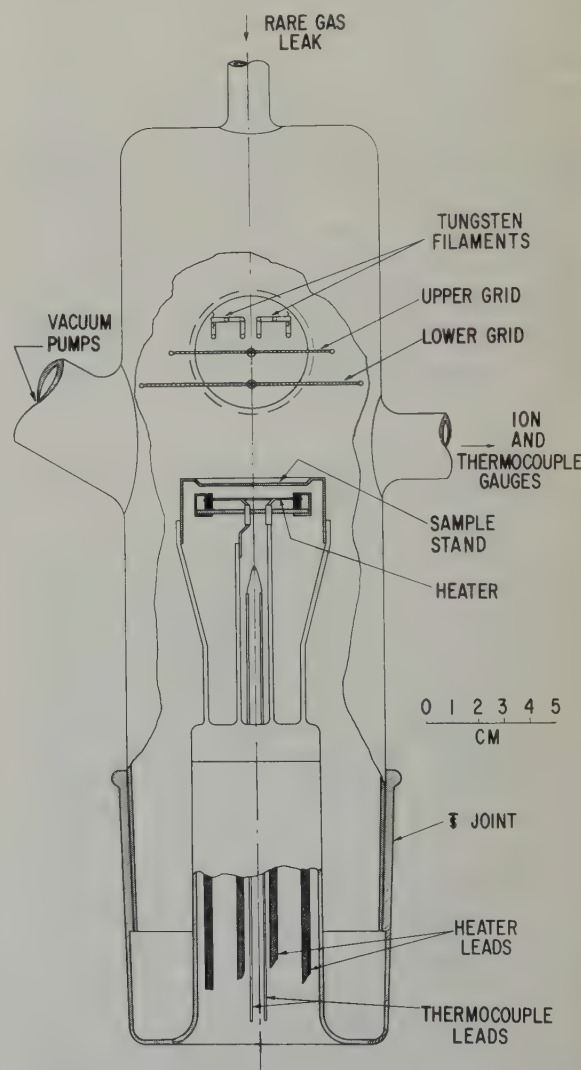


Fig. 1. Arrangement of ion accelerator for loading metals with rare gas atoms.

checked by a very convenient monitor in the form of a survey meter placed about six inches from the anode assembly. Proper conditions were established when the accelerator operated essentially as a gas type X-ray tube. That is, ions from the grid assembly were accelerated through the full potential giving rise to secondary electrons at the sample. The secondary electrons then fell through the full potential causing the emission of X-rays when they struck the anode assembly. Measurement of these X-rays with a survey meter was actually the best criterion for satisfactory operation of the accelerator.

Bombardments were done at about 25°C and there was no evidence for a significant sample temperature rise. After the bombardment was finished, dry nitrogen was admitted and the sample transferred to the mass spectrometer system for study of rare gas evolution on heating. This was done by the technique described by Norton<sup>8</sup>). The sample was placed in the side arm of an evacuated quartz glass tube which has been previously degassed above the temperatures to be used later. A thermocouple was at the central hot zone. The tube led directly to the mass spectrometer with no admission leak intervening. The mass spectrometer was set on the rare gas peak to be studied. From previous calibration through a leak system of known volume and known pump-out half-time, the height of the peak yielded directly the rate of rare gas evolution from the sample in absolute units of  $\text{cm}^3$  (NTP)/sec. This gave a very sensitive measure of rate at each instant, and later the integration under the rate-time plot gave the total amount. The temperature of the sample in the quartz glass evolution tube was gradually raised over a 2 to 4 hour period at 8 to 10°C/min and the rare gas evolution rate continuously measured and recorded.

### 3. Results

Results using the ion accelerator and the mass spectrometer techniques were of two types. First, the results searching for the desired X-ray

effects were negative, even though it was possible to load single crystal evaporated films with approximately 2 at % rare gas atoms. This result, though negative, is very interesting. Second, the subsequent evolution of gas on heating, as measured by the mass spectrometer technique, showed unusual behavior from metal to metal. These results will now be described in turn.

Approximately 1000 Å films of silver and gold were deposited from the vapor onto heated rocksalt crystals. These films could be prepared for X-ray study by coating with an epoxy resin and then dissolving the rocksalt. While the resultant specimen gave some diffuse X-ray scattering around the central beam, due to the resin, the diffraction pattern of the metal crystal was easily observed. Detailed study of both silver and gold single crystal films loaded with approximately 2 at % argon failed to reveal any diffuse scattering attributable to defect distortions around the metal lattice Bragg reflections. Careful lattice parameter measurements on loaded and non-loaded gold films revealed a lattice expansion of only  $0.011 \pm 0.005$  % of the lattice due to the gas. A Vegard's law type calculation based on substitutional solution of the gas and a lattice parameter of 5.31 Å for argon predicts a lattice expansion of 0.61 %. Moreover, the size of the argon atom in a metal lattice has been estimated using two different functions<sup>9</sup>). In neither case was a reduction of the lattice expansion more than 17 % from the Vegard's law value found. Thus, even allowing for the fact that the range of the argon is a fraction of the total film thickness, it is seen that the lattice expansion is lower by an order of magnitude than a reasonable estimate of the expected expansion. These results raise the question of the actual state of the gas in the metal film. It seems to us that there are at least two possibilities: First, that the rare gas atom captures one or more vacancies, formed by bumping collisions, as it comes to rest or, second, that either due to the high concentration of the rare gas or to migration with captured vacancies

at room temperature, there is considerable agglomeration of the gas even at room temperature. There are undoubtedly other possibilities, but in any case the results are of significance in connection with the behavior of fission gases in nuclear fuels. Since present techniques are applicable to other metals and gases, and the

were conducted on annealed foils 2 mils thick of various metals using a sample about  $1 \text{ cm}^2$  in area which had been loaded with rare gas on one side. The results using argon gas with silver, gold, aluminum, and lead are shown in figs. 2, 3, 4 and 5, in which the evolution rate in  $\text{cm}^3$  (NTP)/sec is plotted against temperature.

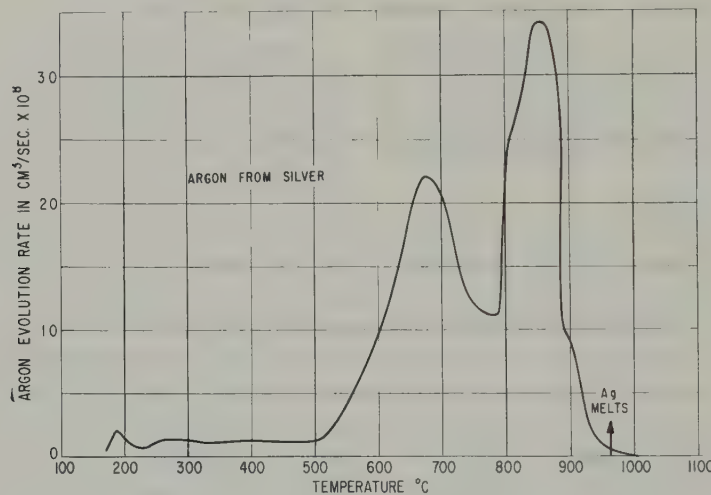


Fig. 2. Argon evolution from silver foil.

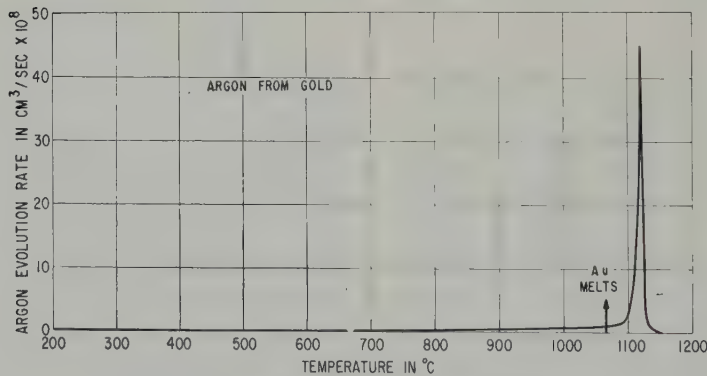


Fig. 3. Argon evolution from gold foil.

thin films are suited to electron microscope examination, it is clear that these techniques might well be of assistance in the study of nuclear fuel systems.

The second interesting feature of the present work was the evolution rate of the rare gas as the sample was heated at a constant rate of approximately  $8^\circ \text{C}/\text{min}$  in the mass spectrometer gas evolution system. These experiments

The total amount of gas evolved was determined by integration of the evolution rate vs. time curve giving  $0.7$ ,  $1.0$ ,  $9.2$  and  $0.3 \times 10^{-4} \text{ cm}^3$  at NTP for silver, gold, aluminum and lead, respectively.

There are three striking features of these rate-time curves: (1) the occurrence of two large peaks for silver and aluminum, compared to a single peak for gold and lead, (2) the fact that

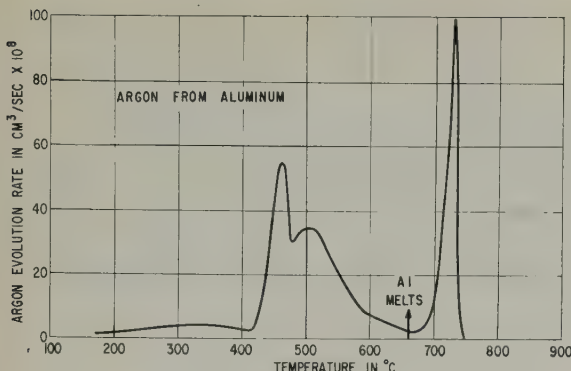


Fig. 4. Argon evolution from aluminum foil.

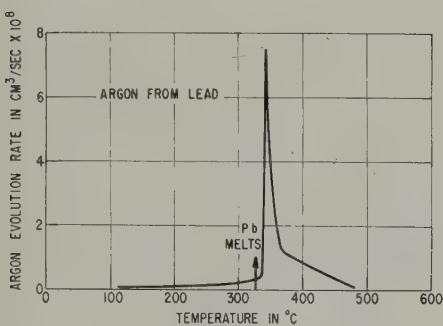


Fig. 5. Argon evolution from lead foil.

for aluminum and silver there is a low but definite and steady rate of argon evolution in the 200–400  $^{\circ}\text{C}$  range. For gold and lead the rate in the lower temperature range is lower than for aluminum and silver, but nevertheless real, and (3) the burst of argon release from gold and lead comes only just after melting; with

aluminum some before and some after melting, and with silver all of the release comes well before melting occurs.

With this difference in behavior from metal to metal, it is not difficult to see why there should be so much controversy over the question whether rare gases diffuse with normal ease or with difficulty in metals. The low temperature peaks in silver and aluminum suggest normal mobility whereas the single peak at or near the melting point for gold and lead might suggest very low mobility. Actually the low temperature rates are not negligible so that at least some of the gas can escape at relatively low temperatures in every case. The first natural explanation for the two peaks is that the low temperature peak represents the onset of high mobility at which time some of the gas escapes and some forms bubbles which are released only when they are uncovered at higher temperatures when the evaporation rate becomes high (case of silver) or the metal melts (case of aluminum). The fact that gold and lead show only one peak may be due to the possibility, suggested to us by D. Turnbull, that these metals might contain a very high density of nucleation sites for bubbles, thereby trapping a very high percentage of the gas.

Other experiments have been performed using various metals and neon, krypton, and xenon as the bombarding gases. The loading portion

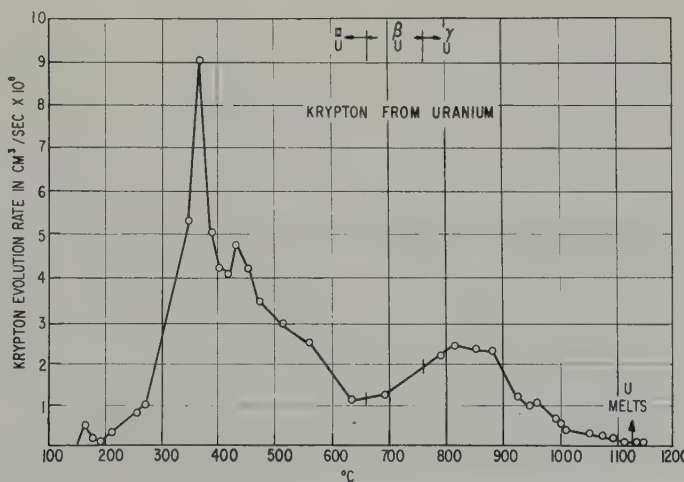


Fig. 6. Krypton evolution from uranium foil.

of the experiments proceeded without difficulty. Gas evolution measurements with the mass spectrometer have been limited, thus far, but it is clear that the gas was embedded in the metals and results similar to those in figs. 2 to 5 were obtained. An additional experiment was performed loading uranium † with krypton. The gas evolution curve for this case is shown in fig. 6. It is clear that in this case there are low and high temperature peaks. Integration of the evolution vs. time curve gave a total of  $1.5 \times 10^{-4}$  cm<sup>3</sup> of krypton. In spite of some uncertainty with respect to oxide film, the value of the method in the study of the behavior of rare gases in uranium seems well demonstrated.

#### 4. Conclusions

From the present work the following is concluded:

1. Energetic rare gas atoms coming to rest in a metal lattice apparently capture vacancies and so do not distort the lattice to an appreciable extent.

2. Wide variations occur in the evolution rates of rare gases from metal to metal. This

† We are indebted to Dr. D. R. Green of the Hanford Laboratories Operation for the sample of uranium.

may well account for the disparity of opinion regarding the ease of migration of rare gases in metals.

3. The ion bombardment coupled with the mass spectrometer technique provides a powerful tool for the study of rare gas-metal systems. In this connection the tracer method of Koch<sup>10</sup> and Thulin<sup>11</sup> might also be of interest.

#### References

- 1) C. W. Tucker, Jr. and P. Senio, *Acta Cryst.* **8** (1955) 371
- 2) C. W. Tucker, Jr. and P. Senio, *Phys. Rev.* **99** (1955) 1777
- 3) R. A. Coyle and B. Gale, *Acta Cryst.* **8** (1955) 105
- 4) B. Borie, *Acta Cryst.* **10** (1957) 89
- 5) K. O. Nielsen, *Electromagnetically Enriched Isotopes and Mass Spectrometry*, edited by M. L. Smith (Butterworths, London, 1956) p. 68-81
- 6) R. A. Schmitt and R. A. Sharp, *Phys. Rev. Letters* **1** (1958) 445
- 7) O. Heinz, E. M. Gyorgy and R. S. Ohl, *Rev. Sci. Instr.* **27** (1956) 43
- 8) F. J. Norton, *J. Amer. Cer. Soc.* **36** (1953) 90
- 9) a) Dobbs and Jones, *Rep. Prog. Phys.* **20** (1957) 516  
b) A repulsive Born-Mayer interaction of the type used by Huntington for Cu, *Phys. Rev.* **91** (1953) 1092; adjusted for the gold atom by the method of Zener, *Acta Cryst.* **3** (1950) 346 (Eq. (10))
- 10) J. Koch, *Nature* **161** (1948) 566
- 11) S. Thulin, *Ark. f. Fys.* **9** (1955) 107

## PHASE TRANSFORMATION, TWINNING AND ANELASTIC PHENOMENON ASSOCIATED WITH ZIRCONIUM DIHYDRIDE †

ROGER CHANG

*Atomics International, A Division of North American Aviation, Inc., Canoga Park, California, USA*

Received 23 May 1960

The atom movements and crystallography of cubic to tetragonal transformation in  $ZrH_2$  are studied and discussed according to the phenomenological theories of Bowles and MacKenzie and of Wechsler, Lieberman, and Read. The large internal friction peak found in  $ZrH_{1.92}$  (but absent in  $ZrH_{1.6}$ ) suggests that it is associated with a stress induced twin interface motion. The relaxation phenomenon appears to be controlled by a diffusion process, presumably that of hydrogen, with an activation energy of about 20 000 calories per mole.

Les mouvements des atomes et la cristallographie du changement de phase de  $ZrH_2$  cubique à  $ZrH_2$  tétragonale sont étudiés et discutés en tenant compte des théories de Bowles et Mackenzie et de Wechsler, Lieberman et Read. La présence du pic important de frottement interne trouvé dans  $ZrH_{1.92}$  (mais absent dans  $ZrH_{1.6}$ ) suggère que cette transformation est associée à un déplacement de l'interface de macle

induit par des tensions. Le phénomène de relaxation semble contrôlé par un processus de diffusion, probablement de l'hydrogène, avec une énergie d'activation d'environ 20 000 kcal/mole.

Die Atombewegungen und die Kristallographie bei der Umwandlung von  $ZrH_2$  vom kubischen zum tetragonalen Gitter wurde studiert und mittels der phänomenologischen Theorien von Bowles und MacKenzie und von Wechsler, Lieberman und Read diskutiert. In  $ZrH_{1.92}$ , nicht aber in  $ZrH_{1.6}$  wurde ein ausgeprägtes Maximum der inneren Reibung gefunden. Es ist naheliegend, dass dieses Maximum mit einer Wanderung von Zwillingsgrenzen zusammenhängt, die durch die Spannung hervorgerufen wird. Die Relaxationserscheinung dürfte von einem Diffusionsvorgang, vornehmlich der Diffusion von Wasserstoff beherrscht werden. Hierfür wurde eine Aktivierungsenergie von etwa 20 kcal/mol ermittelt.

### 1. Introduction

Many fundamental studies of solid metallic hydrides have been stimulated by the chemical nature of these materials, which seemingly is intermediate between that of interstitial alloys and inorganic compounds. This interest has recently been augmented by practical applications of solid hydrogen materials in the field of nuclear engineering as moderators.

The crystal structures of the hydride "compounds" which exist at compositions between  $MH$  and  $MH_2$ , where  $M$  is a Group IV-A metal, have been studied using X-ray diffraction and neutron diffraction by many investigators. The results of X-ray analysis<sup>1)</sup>

indicate that the changes in crystal structure in the  $Zr$ -H and  $Ti$ -H systems on addition of hydrogen are analogous. With high hydrogen content a homogeneous range of cubic phase is observed, which becomes tetragonally distorted near the limiting composition  $ZrH_2$  and  $TiH_2$ . The limits of this range do not correspond to a simple stoichiometric ratio between the components. Neutron diffraction investigations have shown that the hydrogen atoms are located in the tetrahedral holes of the near face-centered metal-atom lattice in both  $ZrH_2$  and  $TiH_2$ <sup>2,3)</sup>.

The lattice parameters of  $TiD_{1.98}$  and  $ZrH_{1.92}$  measured by Yakel<sup>4)</sup> at various temperatures are reproduced in fig. 1. The critical temperature

† This work was supported by the United States Atomic Energy Commission.

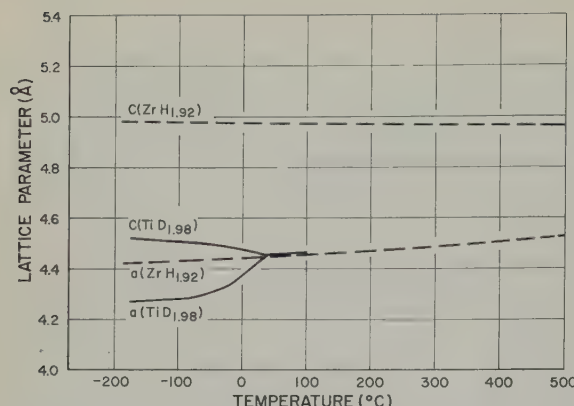


Fig. 1. Lattice parameters of  $\text{TiD}_{1.98}$  and  $\text{ZrH}_{1.92}$  versus temperature.

for the cubic to tetragonal transition in  $\text{TiD}_{1.98}$  is  $37 \pm 4^\circ \text{C}$ . The data for  $\text{ZrH}_{1.92}$  suggest definitely a similar cubic to tetragonal transition which cannot be investigated without high-pressure and high-temperature X-ray diffraction apparatus. The cause of the distortional transformation in the hydrides is not clear. Ordering of an atomic or magnetic nature is eliminated by the close approach of the compounds to stoichiometric compositions and by the results of neutron diffraction experiments. A ferroelectric ordering process is also unlikely in view of the symmetric positions of the atoms in the tetragonal lattice. There is the possibility of a gradual change in bond character between metal-hydrogen or metal-metal neighbors with decreasing temperature which might lead to the observed lattice distortions. An alternate explanation, based on the band theory of metals rather than a chemical bond theory, may be advanced. The transition from a cubic to a tetragonal lattice would then be considered as arising from an overlapping of Brillouin zone boundaries caused by small variations in electron density with temperature. The cubic to tetragonal transformation in  $\text{AuCd}$ ,  $\text{AgCd}$ ,  $\text{InTl}$ , etc., has also been interpreted in terms of the zone overlapping hypothesis, especially in view of the fact that small additions of a third component may influence tremendously the transformation behavior.

It is the purpose of the present study to

evaluate the mechanism and atom movements involved in the cubic to tetragonal transformation in  $\text{ZrH}_2$ . Although X-ray studies of  $\text{ZrH}_2$  near the transformation temperature have yet to be carried out, the similarity between  $\text{ZrH}_2$  and  $\text{TiH}_2$  and the microstructural aspects of  $\text{ZrH}_2$  indicate beyond any doubt that a cubic to tetragonal transformation exists in  $\text{ZrH}_2$ . The paper discusses also the anelastic behavior of tetragonal  $\text{ZrH}_2$ . The presence of a relaxation peak in the heavily twinned tetragonal state and the absence of a similar peak in the cubic state suggest convincingly that the relaxation peak is associated with stress induced motion of twin interfaces in the material.

## 2. Crystallography of Transformation and Microstructures of the Transformed Product

The phenomenological theories of the crystallography of cubic to tetragonal transformation have been discussed by Christian<sup>5</sup>). It was pointed out that the theories of Bowles and MacKenzie<sup>6</sup>) and of Wechsler, Lieberman and Read<sup>7</sup>) are essentially equivalent, although they differ in mathematical formulation. The fundamental idea on which the theory is based is that the total transformation distortion is such that at least one plane (the habit plane) is undistorted and unrotated. An undistorted plane is not produced if the total distortion consists solely of the pure lattice distortion. However, the pure lattice distortion may be combined with a slip shear or a twinning shear (over a fraction of the crystal) which does not affect the lattice structure but produces a microscopic change in shape. In the case of cubic to tetragonal transformation in  $\text{Au-Cd}$ <sup>8</sup>) and  $\text{In-Tl}$ <sup>9,10</sup>), the second distortion was invariably shown to be a twinning shear such that the tetragonal phase is twinned and that for an appropriate ratio of twin thicknesses, the average misfit strain between the twinned tetragonal phase and the cubic phase is zero. An exact calculation by Wechsler, Lieberman and Read<sup>7</sup>) yields the following expressions for the habit plane indices ( $hkl$ ) referred to the cubic phase:

$$\left. \begin{aligned} h &= \frac{1}{2\eta_1} \left\{ \sqrt{\frac{2\eta_1^2\eta_2^2 - \eta_2^2}{\eta_2^2 - 1}} - \sqrt{\frac{\eta_1^2 + \eta_2^2 - 2}{\eta_2^2 - 1}} \right\} \\ k &= \frac{1}{2\eta_1} \left\{ \sqrt{\frac{2\eta_1^2\eta_2^2 - \eta_2^2}{\eta_2^2 - 1}} + \sqrt{\frac{\eta_1^2 + \eta_2^2 - 2}{\eta_2^2 - 1}} \right\} \\ l &= \frac{1}{\eta_1} \sqrt{\frac{1 - \eta_1^2}{\eta_2^2 - 1}} \end{aligned} \right\} \quad (1)$$

where  $\eta_1 = a/a_0$  and  $\eta_2 = c/a_0$ ,

$a_0$ ,  $a$ , and  $c$  being lattice parameters of the cubic and tetragonal phases, respectively. The same authors also obtained the following equation for the relative amounts of the two twins ( $x$ ,  $1-x$ ):

$$x = \frac{1}{2} \pm \frac{1}{2} \frac{(1 - \eta_1^2\eta_2^2)}{(\eta_1^2 - \eta_2^2)} \sqrt{1 - \left[ \frac{(\eta_1^2 - 1)(\eta_2^2 - 1)}{1 - \eta_1^2\eta_2^2} \right]^2}. \quad (2)$$

Using the room temperature lattice parameter data of Softina and co-workers<sup>1</sup> for the high-hydrogen side of the Zr-H system:

$$a_0 = 4.76 \text{ \AA}$$

$$a = 4.44 \text{ \AA}$$

$$c = 4.97 \text{ \AA}$$

eq. (1) and (2) yield a habit plane of indices (0.067, 1.00, 1.15), which is about 3 degrees from (011), and 0.51, 0.49 for the relative amounts of the two twins, in agreement with our experimental data.

The microstructures of a tetragonal specimen ( $ZrH_{1.85}$ ) at room temperature at  $70 \times$  and  $350 \times$  are shown in fig. 2 †. Both the fine twin bands and the gross twin bands are approximately parallel to the (011) type plane of the high-temperature cubic phase. The X-ray back reflection Laue photograph of a typically twinned region is analyzed and stereographically plotted in fig. 3, showing the orientation relationship of the twins with respect to themselves, the twin interface being the (101) type plane of the tetragonal lattice.

### 3. Anelastic Phenomenon Associated with Twin Interface Motion

The twin interfaces formed as a result of cubic to tetragonal transformation are very mobile, and their motion requires only very small movements of the atoms. If, for example, the twin interfaces are locked by impurities or defects, motion of these interfaces under an applied shear stress will be controlled by the diffusion rates of the impurity or defect. Furthermore, twin interface motion in an

† Similar investigation revealed the absence of both coarse and fine twin bands in a cubic specimen ( $ZrH_{1.63}$ ).

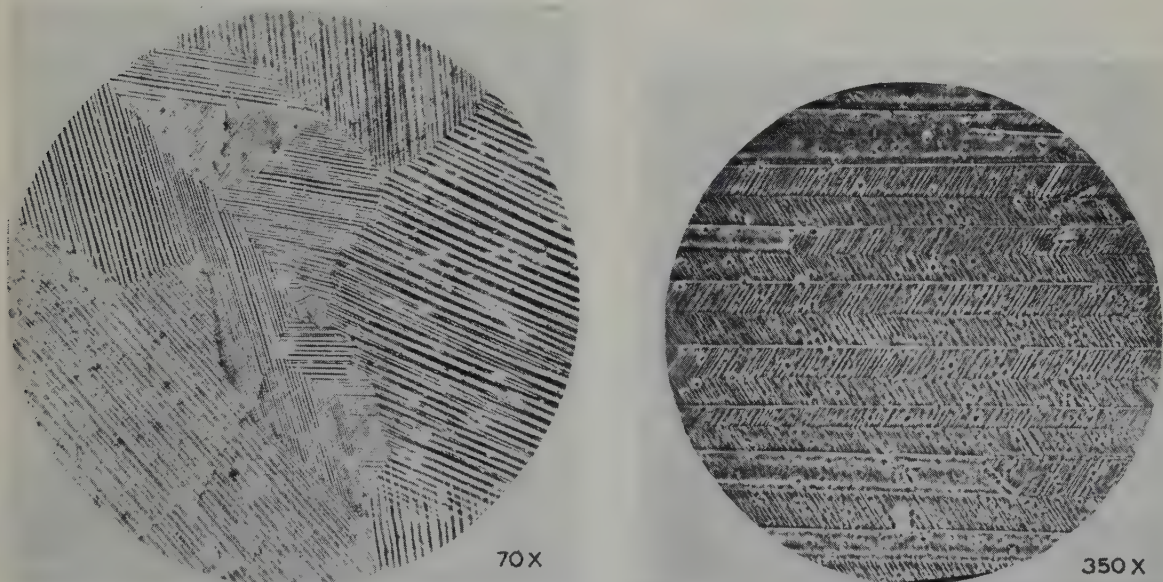


Fig. 2. Microstructure of  $ZrH_{1.85}$  at room temperature, magnified 70 and 350 times.

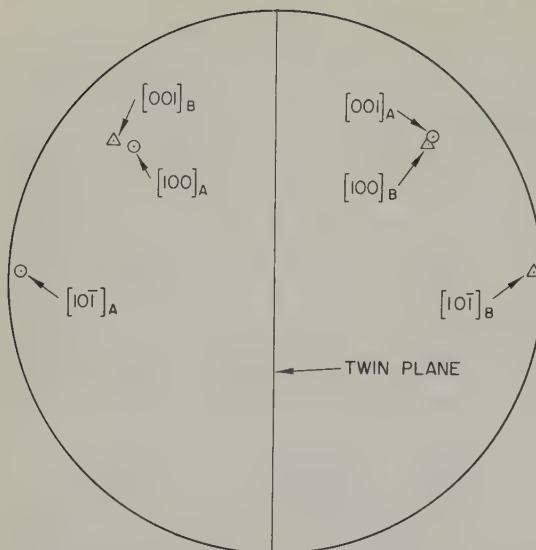


Fig. 3. Stereographic projection of back reflection Laue zones of a twinned crystal ( $\text{ZrH}_{1.85}$ ).

ordered two-component system may require the synchronized movement of both atom species the rate of which may be controlled by diffusion of one of the two atom species. At low temperatures the motion of the twin interface under dynamic conditions is so slow that no appreciable displacement occurs during a half-cycle of vibration, and the internal friction is low. On the other hand, the twin interfaces at high temperatures are so mobile that the shear stress is completely relieved at all times, so the internal friction is again very low. Only in the intermediate temperature range where both the displacement and the net shear stress are appreciable, is the internal friction large. The internal friction peak of Cu-Mn alloys ( $\approx 90$  percent Mn) found by Worrell<sup>11</sup> is thus interpreted by Zener<sup>12</sup> to arise from stress induced movement of the twin interfaces of this alloy.

Internal friction measurements were used to study twin interface motion in zirconium hydride. The most recent phase diagram for the Zr-H system is shown in fig. 4<sup>13</sup>. At room temperature the material is completely cubic at  $\text{H/Zr} < 1.65$  and completely tetragonal at  $\text{H/Zr} > 1.75$ . The internal friction data of two hydrides  $\text{ZrH}_{1.92}$  and  $\text{ZrH}_{1.6}$  are reproduced in

figs. 5 and 6. Indeed, a large internal friction peak is present in the hydride  $\text{ZrH}_{1.92}$  but is absent in the hydride  $\text{ZrH}_{1.6}$ . The results are very convincing that the internal friction peak in  $\text{ZrH}_{1.92}$  is associated with a stress induced motion of the twin interfaces in the material. The shift of peak temperature with frequency yields an activation energy of approximately 20 000 calories per mole.

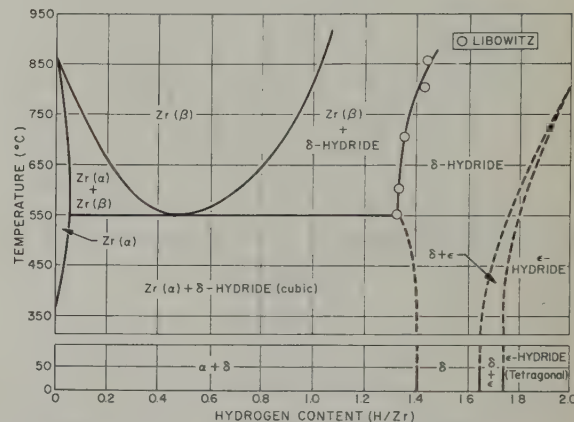


Fig. 4. Phase diagram of the Zr-H system.

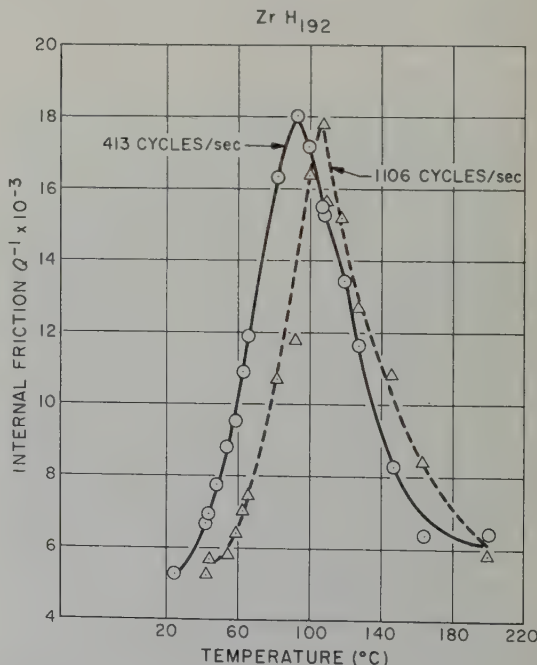


Fig. 5. Internal friction versus temperature for  $\text{ZrH}_{1.92}$  at two frequencies.

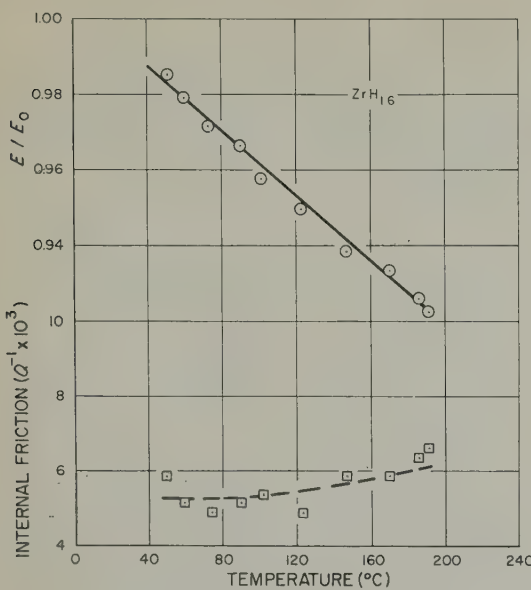


Fig. 6. Young's modulus and internal friction versus temperature for  $ZrH_{1.6}$ .

#### 4. Discussion

The X-ray diffraction and metallographic studies presented here indicate beyond doubt the presence of a cubic to tetragonal distortional transformation in the Zr-H system. Such transformation is indicated by the dotted lines of fig. 4. Further verification of the transformation using high-temperature high-pressure X-ray diffraction is needed.

An important result of this study is the internal friction peak associated with stress-induced twin interface motion. The activation energy associated with the relaxation process,  $\approx 20\,000$  calories per mole, is believed to be associated with that for the diffusion of hydrogen in the material.

A closer look at the crystal structure of  $ZrH_2$  suggests that the twin interface cannot be one atomic layer thick and must be composed of arrays of edge or screw type twinning dislocations. The paths taken by atoms during twin interface motion will most likely be defined by the geometry of dislocations or partial dislocations in the lattice in a manner suggested by Kronberg for slip and twinning in sapphire<sup>14</sup>). Although the details of atom movements have yet to be worked out, it is

likely that such movements may require the synchronized motion of both atom species. If twinning is to be described by the shearing of Zr atoms (or ions), the synchronized motion of H atoms (or ions) from tetrahedral to octahedral and back to tetrahedral sites is required and it is not unreasonable to suggest that twin interface motion is controlled by the rate of hydrogen diffusion in the lattice.

A schematic drawing showing two edge-type twinning dislocations in a (101) <sup>†</sup> twin boundary of a face-centered tetragonal lattice is shown in fig. 7<sup>15</sup>). The plane of figure is perpendicular to [010]. Applying the diagram to  $ZrH_2$  (the  $c/a$  ratio being slightly exaggerated): open circles are Zr atoms (or ions) in the plane of the figure; filled circles are the projection of the next atomic layer of Zr atoms on this plane; squares are the projection of a layer of H atoms (or ions) located between the two layers of Zr atoms, each H being "tetrahedrally" sur-

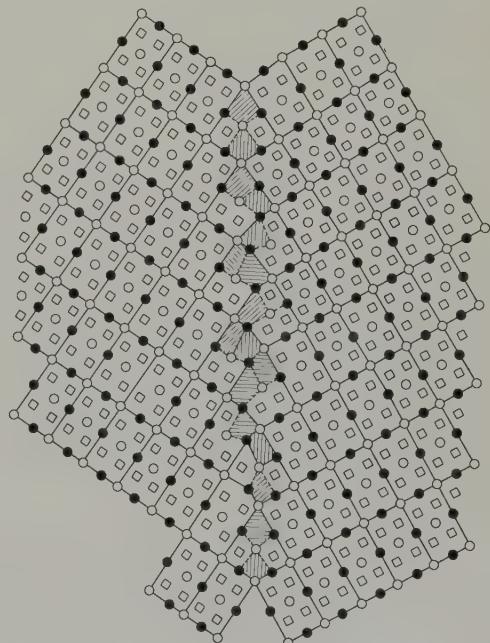


Fig. 7. Schematic drawing showing two edge type twinning dislocations of a (101) twin boundary of a face-centered tetragonal lattice.

<sup>†</sup> Numbers in parentheses are Miller indices of a plane; those in square brackets are Miller indices of a direction.

rounded by 4 Zr. The shaded regions are those where the "tetrahedral" sites are badly distorted. Two possibilities exist: (1) the H atoms could stay in the distorted tetrahedral sites; (2) the H atoms are relocated to nearby interstitial octahedral sites. The first possibility is unlikely, and it is conceivable according to the second alternative that twin boundary motion will be impeded by the relocation of hydrogen atoms and controlled by the rate of diffusion of hydrogen. Further studies are needed to substantiate the hypothesis.

### Acknowledgement

The author is grateful to L. L. Bienvenue, Atomics International, who obtained the internal friction data for both  $\text{ZrH}_{1.92}$  and  $\text{ZrH}_{1.6}$ , and to C. G. Rhodes, Atomics International, who obtained the micrographs for  $\text{ZrH}_{1.85}$  (fig. 2).

### References

- 1) V. V. Softina, Z. M. Azarkh and N. N. Orlova, *Crystallography* (Soviet Physics) 3 (1959) 544
- 2) S. S. Sidhu, L. Heaton and D. D. Zauberis, *Acta Cryst.* 9 (1956) 607
- 3) R. E. Rundle, C. G. Shull and E. O. Wollan, *Acta Cryst.* 5 (1952) 22
- 4) H. L. Yakel, Jr., *Acta Cryst.* 11 (1958) 46
- 5) J. W. Christian, *J. Inst. Met.* 84 (1955) 386
- 6) J. S. Bowles and J. K. MacKenzie, *Acta Met.* 2 (1954) 129, 224
- 7) M. S. Wechsler, D. S. Lieberman and T. A. Read, *Trans. AIME* 197 (1953) 1503
- 8) L. C. Chang and T. A. Read, *Trans. AIME* 191 (1951) 47
- 9) M. W. Burkart and T. A. Read, *Trans. AIME* 197 (1953) 1516
- 10) Z. S. Basinski and J. A. Christian, *Acta Met.* 2 (1954) 148
- 11) F. Worrell, *Phys. Rev.* 72 (1947) 533
- 12) C. Zener, *Elasticity and Anelasticity of Metals* (University of Chicago Press, 1948)
- 13) G. G. Libowitz, *U.S. Atomic Energy Commission Report*, NAA-SR-5015 (1960)
- 14) M. L. Kronberg, *Acta Met.* 5 (1957) 507
- 15) Z. S. Basinski and J. W. Christian, *Acta Met.* 2 (1954) 101

## A METHOD SUITABLE FOR THE MEASUREMENT OF THE THERMAL DIFFUSIVITY OF IRRADIATED MATERIALS

D. SMART

*Nuclear Research Centre, C. A. Parsons & Co. Ltd., Fossway, Newcastle-upon-Tyne, UK*

Received 13 May 1960

A description is given of a transient method which is suitable for measuring thermal diffusivity of irradiated materials. The time taken for the measurement is short and some of the difficulties normally encountered in handling and machining radioactive material, prior to such a measurement, are avoided. The theory is developed, a prototype test equipment described and results quoted for brass, steel, natural uranium (unirradiated), copper and aluminium. For brass, steel and natural uranium specimens the accuracy is better than  $\pm 5\%$  of the accepted values reported in the literature. The accuracy for aluminium and copper could be improved by using longer specimens in a modified apparatus. The measurement is of the macroscopic thermal conductivity, i.e. averaged over an area much greater than that of a single crystallite.

On décrit une méthode rapide qui est bien appropriée à la mesure de la diffusibilité thermique des matériaux irradiés. Le temps pris pour la mesure est court et quelques-unes des difficultés, normalement rencontrées pour manipuler et usiner les matériaux radioactifs avant la mesure elle-même, sont évitées. La théorie est développée, un équipement prototype de mesure décrit et des résultats sont présentés dans le cas du laiton, de l'acier, de l'uranium naturel (non irradié), du cuivre et de l'aluminium. Pour le laiton, l'acier et

l'uranium naturel, la précision est supérieure à  $\pm 5\%$  des valeurs reportées dans la littérature. La précision pour l'aluminium et le cuivre pourrait être améliorée en utilisant des échantillons plus longs dans un appareil modifié. La mesure correspond à une conductibilité thermique macroscopique, c'est à dire qu'elle représente la moyenne obtenue sur une surface beaucoup plus grande que celle d'un seul cristallite.

Eine rasche Methode zur Messung der Wärmeleitfähigkeit bestrahlter Materialien wird beschrieben. Die gesamte, für eine Messung erforderliche Zeit ist kurz, und die Schwierigkeiten, die üblicherweise vor der Messung beim Bearbeitung und Umgang radioaktiven Materiale auftreten, werden vermieden. Es wird eine Theorie entwickelt und eine erste Prüf-anlage erläutert. Ferner sind Messergebnisse über Messing, Stahl, unbestrahltes Natururan, Kupfer und Aluminium aufgeführt. Für Messing, Stahl und Natururan weichen die Ergebnisse höchstens um  $\pm 5\%$  von den der Literatur entnommenen Werten ab. Bei Kupfer und Aluminium kann man die Genauigkeit der Ergebnisse durch Verwendung längerer Proben und einer abgewandelten Apparatur verbessern. Die Messungen ergeben wie bei der makroskopischen Wärmeleitfähigkeit Mittelwerte über eine Fläche, die viel grösser als ein einzelnes Kristallkorn ist.

### 1. Introduction

A transient method of measuring thermal diffusivity is described. The measurement involves the heating of a cylindrical specimen uniformly to a known temperature and then placing it co-axially on a cylinder of ice of the same diameter. The rate at which the ice melts is measured and from this the thermal diffusivity of the specimen can be calculated. If the specific heat and density of the material are

known, its thermal conductivity can also be determined.

This technique for determining thermal conductivity has several advantages over other methods in that during the test the only measurements necessary are of displacement and time. No direct temperature measurements on the specimen are needed, obviating the need for attaching thermocouples, nor is any special preparation of the specimen surface necessary,

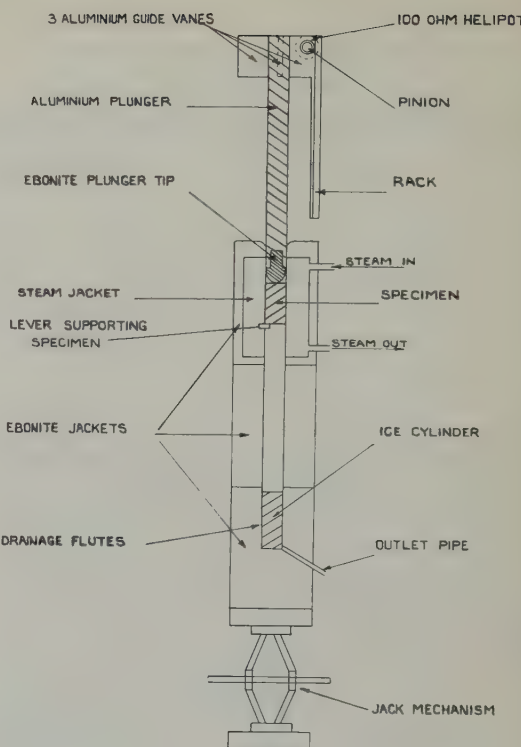
as good thermal contact between specimen and ice is maintained by a thin film of water. These last two points, together with the short time taken to complete the measurement (four minutes), are especially advantageous when tests on irradiated material are contemplated.

## 2. Apparatus

The apparatus (fig. 1) was intended for measurements on irradiated material. It was therefore designed to make use of remote handling techniques and to require a minimum of servicing. The body of the apparatus was constructed from ebonite since it is a good thermal insulator, non-porous, reasonably robust, and easy to machine. The specimen to be tested is supported inside the apparatus by a lever which protrudes through the wall of the steam jacket. To begin a test this lever is moved so that the specimen is allowed to fall on to the cylinder of ice held in the lower part of the apparatus.

To measure the rate at which the specimen melts the ice, a device is used which gives a permanent record of the motion of the specimen during the test. This consists of a plunger which follows the movement of the specimen inside the apparatus. A helical potentiometer is attached to one of the plunger guide vanes so that a pinion on the shaft of the potentiometer engages with a rack fastened to the side of the apparatus. Thus any movement of the plunger turns the shaft of the potentiometer. The potentiometer forms part of a simple resistance bridge circuit, and the out-of-balance voltage is applied to a high speed pen recorder. This arrangement permits remote reading of the displacement of the plunger.

The lower part of the apparatus, containing the ice chamber, is supported on a jack which gives a means of access to the ice chamber other than through the steam jacket. This is necessary because a cylinder of ice is used to cool the apparatus to 0° C and has to be replaced by a fresh cylinder immediately before a test. The ice chamber has four flutes cut into the walls



(Not to scale)

Fig. 1. Thermal conductivity apparatus.

to allow water produced during the test to drain away.

## 3. Test Specimens

Initially the test specimens were cylinders 2.9 cm dia. by 9.1 cm long. These dimensions were chosen at the request of the UKAEA as convenient for their purpose.

## 4. Experimental Method

The specimen was heated to about 110° C in an oven, then transferred to the steam jacket in the apparatus. It was left in the steam jacket for about 10 minutes to reach equilibrium at 100° C. This procedure was adopted for two reasons. First, if the specimen was heated up in the steam jacket it took 2½ to 3 hours to reach 100° C from room temperature. Second, if it was heated to 100° C outside the apparatus, a fall in temperature of about 10° C occurred while the specimen was being transferred to the

apparatus; it then took about 1 hour to reach equilibrium at 100°C in the steam jacket. By preheating to 110°C outside the apparatus, these difficulties were avoided and the interval between measurements was reduced from 3 hours to about 20 minutes.

Some time before a measurement, a cylinder of ice was placed in the ice chamber, to reduce the temperature of the surrounding parts of the apparatus to about 0°C. Immediately before a test was started this ice was removed and replaced by a fresh cylinder which had been stored at 0°C. After each test, the device used to measure the rate at which the specimen melted the ice was calibrated in terms of displacement, by moving the plunger through a fixed distance and observing the travel of the pen on the recorder chart. The fixed distance had previously been measured with a travelling microscope. This was done to avoid the effects on the measurement of long term changes in the sensitivity of the recording equipment.

When making measurements on a specimen with a high thermal diffusivity, the ice initially melted very rapidly and the water produced did not have time to drain away; a thin film of water was then raised by surface tension into the gap between the specimen and the tube walls. This had a considerable effect on the direction of heat flow in the end of the specimen and produced inaccurate results. It was not practicable to increase the size of the drainage flutes as the ice would be forced into them. To overcome this difficulty, the sides of the specimen were smeared with a thin film of silicone grease which prevented the water from moving into the gap between the specimen and the tube walls. This was only necessary with copper and aluminium specimens.

## 5. Theory †

A cylinder of metal heated uniformly to a known temperature,  $T_0$ , is placed co-axially on a cylinder of ice of identical cross-section. It is assumed that heat transfer takes place only at

† The meaning of the symbols used is explained in the Appendix.

the ice-metal interface, i.e. that all heat flow is parallel to the axis of the specimen.

From Carslaw and Jaeger<sup>1)</sup> (eq. (2), p. 100) it can be shown that the heat flux through the end of the cylinder is:

$$-kA \left( \frac{\partial \theta}{\partial z} \right)_{z=z_i} = \frac{2kT_0A}{l} \sum_{n=0}^{\infty} \exp \left[ -\frac{Kt_1\pi^2}{4l^2} (2n+1)^2 \right].$$

This expression is convergent for all  $t > 0$ . Integrating from  $t_1$  to  $\infty$ , the heat flux during this time is given by:

$$\begin{aligned} & -kA \int_{t_1}^{\infty} \left( \frac{\partial \theta}{\partial z} \right)_{z=z_i} dt = \\ & = \frac{8T_0Acpl}{\pi^2} \sum_{n=0}^{\infty} \left[ \frac{1}{(2n+1)^2} \exp \left\{ -\frac{Kt_1\pi^2}{4l^2} (2n+1)^2 \right\} \right]. \end{aligned}$$

This quantity must be equivalent to the amount of heat taken up by the ice melted in this time, i.e.

$$\begin{aligned} & [z_i(t_1) - z_i(\infty)] A \varrho_{\text{ice}} S = \\ & = \frac{8T_0Acpl}{\pi^2} \sum_{n=0}^{\infty} \left[ \frac{1}{(2n+1)^2} \exp \left\{ -\frac{Kt_1\pi^2(2n+1)^2}{4l^2} \right\} \right] \end{aligned} \quad \left. \right\} \quad (1)$$

The heat taken up by the total amount of ice melted from  $t=0$  to  $t=\infty$  must be equal to the amount of heat originally in the metal cylinder (referred to 0°C), i.e.

$$[z_i(0) - z_i(\infty)] A \varrho_{\text{ice}} S = Al \varrho c T_0. \quad (2)$$

If the specific heat of the specimen,  $c$ , is unknown, the positions  $z_i(0)$ ,  $z_i(t_1)$  and  $z_i(\infty)$  must be observed. Eq. (2) then gives  $c$ , and  $K$  can be obtained from a plot of the series part of eq. (1) against  $Kt\pi^2/4l^2$ .

If  $c$  is already known, the right hand side of (2) may be calculated; let this be  $Q$ . Then subtracting (1) from (2):

$$\begin{aligned} & [z_i(0) - z_i(t_1)] A \varrho_{\text{ice}} S = \\ & = Q - \frac{8T_0Acpl}{\pi^2} \sum_{n=0}^{\infty} \left[ \frac{1}{(2n+1)^2} \exp \cdot \right. \\ & \quad \left. \cdot \left\{ -\frac{Kt_1\pi^2(2n+1)^2}{4l^2} \right\} \right] \end{aligned} \quad \left. \right\} \quad (3)$$

and only two readings need to be taken.

It may be more convenient to measure the

time taken to melt a given thickness of ice, in which case the left hand side of (3) is a known constant, say  $P$ , resulting in:

$$\frac{\pi^2(Q-P)}{8T_0Ac\varrho l} = \sum_{n=0}^{\infty} \left[ \frac{1}{(2n+1)^2} \exp \cdot \right. \left. \cdot \left\{ -\frac{Kt_1\pi^2}{4l^2} (2n+1)^2 \right\} \right] \quad (4)$$

Since  $K = k/c\varrho$  is the only unknown involved in the right hand side of (4), the system could be calibrated by geometrically identical cylinders of different metals and then used as a comparative method.

Since  $Q = \varrho AclT_0$ , eq. (4) may be rearranged to give:

$$\frac{P}{Q} = 1 - \frac{8}{\pi^2} \sum_{n=0}^{\infty} \left[ \frac{1}{(2n+1)^2} \exp \cdot \right. \left. \cdot \left\{ -\frac{Kt_1\pi^2}{4l^2} (2n+1)^2 \right\} \right] \quad (5)$$

Corresponding values of  $P/Q$  and  $Kt\pi^2/4l^2$  are given in table 1.

TABLE 1

$Kt\pi^2/4l^2$	$P/Q$	$Kt\pi^2/4l^2$	$P/Q$
0.00	0.0000	1.00	0.7018
0.05	0.1606	1.05	0.7163
0.10	0.2272	1.10	0.7302
0.15	0.2782	1.15	0.7433
0.20	0.3213	1.20	0.7559
0.25	0.3592	1.25	0.7678
0.30	0.3934	1.30	0.7791
0.35	0.4249	1.35	0.7899
0.40	0.4542	1.40	0.8001
0.45	0.4816	1.45	0.8099
0.50	0.5074	1.50	0.8191
0.55	0.5317	1.55	0.8279
0.60	0.5547	1.60	0.8363
0.65	0.5766	1.65	0.8443
0.70	0.5973	1.70	0.8519
0.75	0.6170	1.75	0.8591
0.80	0.6357	1.80	0.8660
0.85	0.6535	1.85	0.8725
0.90	0.6704	1.90	0.8788
0.95	0.6865	1.95	0.8847
2.00			0.8903

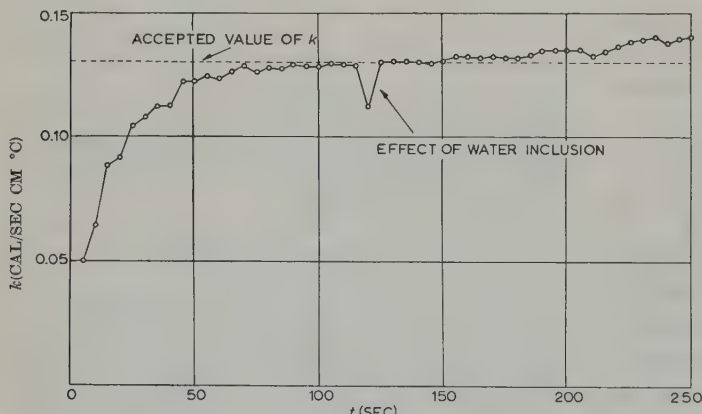


Fig. 2.  
Typical measurements on steel.

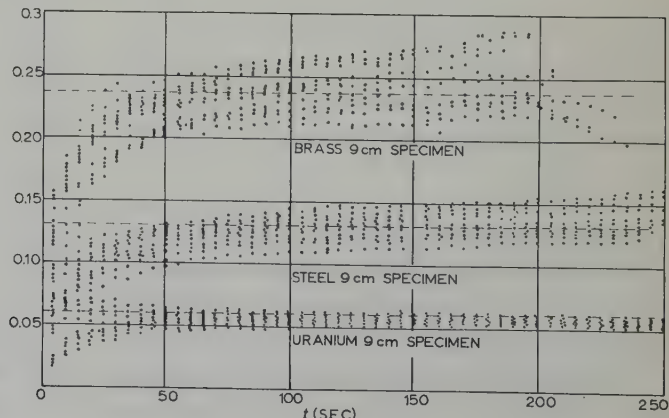


Fig. 3.  
 $k$  vs  $t$  for brass, steel and natural uranium specimens, 9.1 cm (3.6") long. Dashed lines indicate accepted values.

## 6. Results

After each test, the displacement of the specimen after successive intervals of five seconds was found and the value of  $k$  calculated. These results were plotted against time, such a graph for steel being shown in fig. 2. Fig. 3 shows the results obtained for 61/39 brass, steel and uranium.

The calculated values of  $k$ , at intervals of 5 seconds between 100 and 200 seconds, were then taken and the arithmetic mean found. This mean is taken as the measured value of  $k$  for the test, at an effective temperature of 50°C. The results of a dozen tests each on brass, steel and uranium samples were treated in this way and the mean, standard deviation,

and coefficient of variation of these results calculated (tables 2-4). These figures give an estimate of the dispersion of the results, and the accuracy is estimated by comparing the mean value of  $k$  obtained from the measurements with the generally accepted value of  $k$  for the material.

To test the validity of using the standard deviation and coefficient of variation as measures of dispersion in such a small sample, each table was divided in two and these quantities recalculated for each half. There was no great difference between the figures obtained for the whole, and each half of the table. It is then reasonable to assume that the twelve results shown for each specimen are a fair sample of

TABLE 2  
Measured  $k$  for 61/39 brass

Measured $k$
0.2689
0.2254
0.2493
0.2472
0.2557
0.2297
0.2155
0.2303
0.2301
0.2892
0.2667
0.2600

Units for  $k$ : cal/sec cm °C

TABLE 3  
Measured  $k$  for steel

Measured $k$
0.1302
0.1360
0.1380
0.1233
0.1139
0.1291
0.1314
0.1442
0.1235
0.1389
0.1212
0.1387

Units for  $k$ : cal/sec cm °C

Section of results	Mean	Standard deviation	Coefficient of variation (%)
First half of table	0.2460	0.014 84	6.03
Second half of table	0.2486	0.025 35	10.19
Whole table	0.2473	0.020 85	8.43

Measured  $k$ : 0.2473

Accepted  $k$ : 0.2360\*

% difference: +4.61

\* Handbook of Chemistry and Physics (Chemical Rubber Publishing Co.) (Value for 60/40 brass).

Section of results	Mean	Standard deviation	Coefficient of variation (%)
First half of table	0.1284	0.008 06	6.28
Second half of table	0.1329	0.008 42	6.34
Whole table	0.1307	0.008 55	6.54

Measured  $k$ : 0.1307

Accepted  $k$ : 0.1300\*

% difference: +0.53

\* Metals Handbook (American Society for Metals, 1948).

TABLE 4  
Measured  $k$  for unirradiated, natural uranium

Measured $k$
0.0577
0.0517
0.0457
0.0543
0.0561
0.0574
0.0571
0.0568
0.0599
0.0601
0.0676
0.0572

Units for  $k$ : cal/sec cm °C

Section of results	Mean	Standard deviation	Coefficient of variation (%)
First half of table	0.0538	0.004 158	7.73
Second half of table	0.0596	0.003 89	6.53
Whole table	0.0567	0.005 04	8.80

Measured  $k$ : 0.0567

Accepted  $k$ : 0.059\*

% difference: -3.9

\* Quoted by UKAEA.

those which could be obtained using this method.

No special preparation of the specimen surface was necessary; a bar which had been cut with a hacksaw was quite suitable, and a layer of oxide on the specimen surface had no significant effect on the results obtained. The specimens used in these experiments were initially 2.9 cm dia. by 9.1 cm long. Unsatisfactory results were, however, obtained for copper and aluminium specimens because of their high thermal diffusivity. The solution to this difficulty was indicated by the results obtained using longer specimens (fig. 4 and table 5). As a rough guide, specimens with  $k > 0.3$  cal/sec cm °C should be more than 9.1 cm long to obtain accurate results. Measure-

ments were made with lengths of 11.4 cm and 15.2 cm for copper and aluminium. These indicate that if the specimen length had been increased even further, the measurements of  $k$  for these materials would have been satisfactory; this was not possible, however, as a specimen more than 15.2 cm long could not be accommodated in the existing steam jacket. To check if increased specimen length gave more accurate results, tests were carried out on brass specimens of various lengths. The results of these tests, which confirm the above hypothesis, are shown in fig. 5. Some of these graphs are short as values of  $k$  were not calculated for  $P/Q > 0.8$ . They show, however, that as the

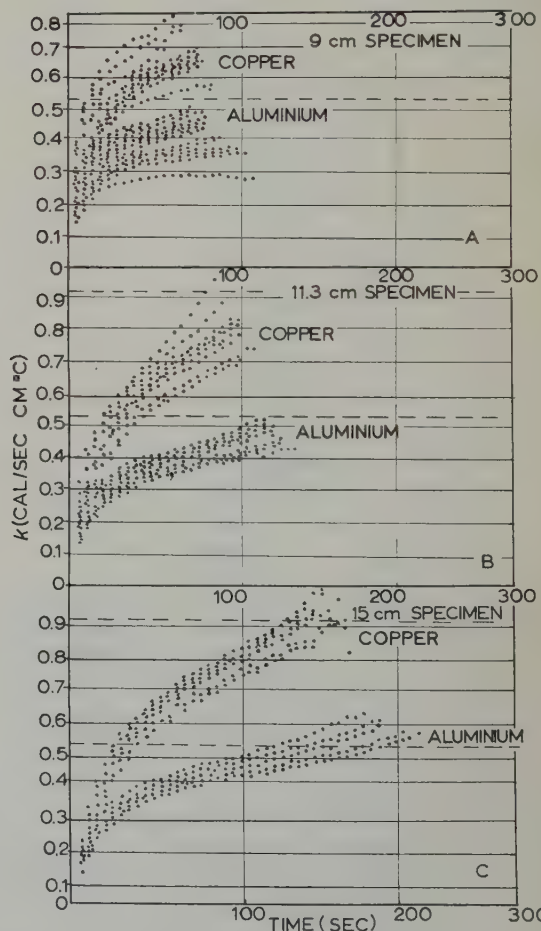


Fig. 4. Effect of length on  $k$  vs  $t$  relationship for copper and aluminium specimens, 9.1 cm (3.6"), 11.4 cm (4.5") or 15.2 cm (6") in length. Dashed lines indicate accepted values.

TABLE 5  
15.2 cm specimen

	Aluminium	Copper
	0.472	0.776
	0.444	0.787
	0.451	0.861
	0.492	0.826
	0.512	0.828
		0.848
Mean	0.474	0.821
Accepted value	0.530*	0.918**
% difference	10.6	10.6

11.4 cm specimen		
	Aluminium	Copper
	0.4890	0.8285
	0.4298	0.7556
	0.4141	0.6898
	0.4933	0.6661
	0.4295	0.7669
	0.4241	0.9006
	0.4854	0.7683
	0.4595	0.7757
	0.4768	0.7275
Mean	0.4548	0.7643
Accepted value	0.530*	0.918**
% difference	14.2	16.8

\* Aluminium (Nuclear Engineering Data Sheet No. 9).

\*\* Copper (Handbook of Chemistry and Physics).

The figures shown above are the average of results obtained after 100 seconds had elapsed. No figures are shown for 9.1 cm specimens as usually with these specimens  $P/Q$  exceeded 0.8 before 100 seconds had elapsed. The difference between the accepted conductivity values, and the values obtained experimentally for these short specimens, were 20.9 % and 33.1 % for aluminium and copper respectively.

specimen length is increased to a value dependent on the material, the results obtained become more satisfactory. When the length of the aluminium specimen was increased from 9.1 cm to 11.4 cm the graph showed an inflection and at 15.2 cm it showed the beginning of a plateau. The curve for copper showed an inflection when the specimen length was 15.2 cm.

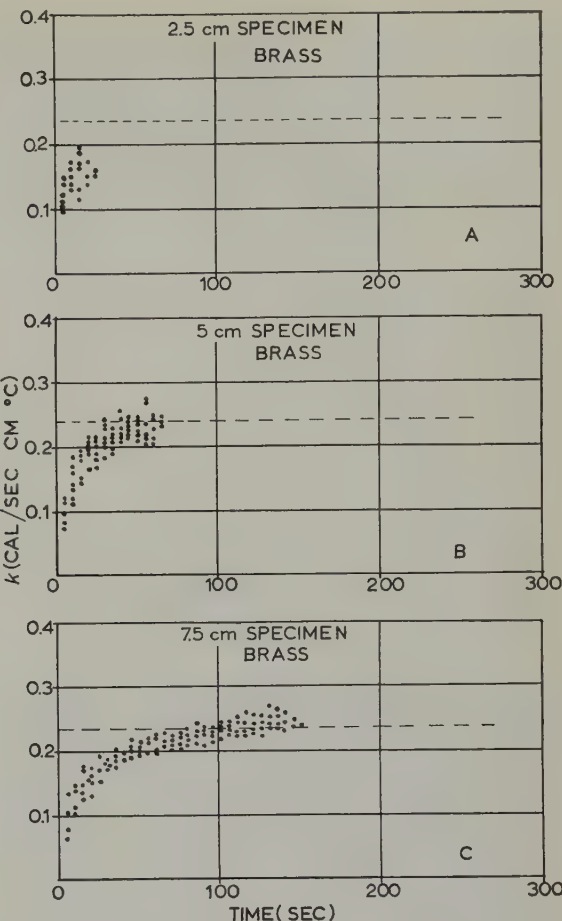


Fig. 5. Effect of length on  $k$  vs  $t$  relationship for brass specimens, 2.5 cm (1"), 5 cm (2") or 7.6 cm (3") in length. Dashed lines indicate accepted values.

## 7. Analysis of Results

The results obtained for brass, steel and uranium (fig. 3 and tables 2-4) indicate that the accuracy of the method is better than  $\pm 5\%$  of the values quoted in the literature.

Most of the results shown were evaluated using a digital computer, as the calculations are tedious when done by hand. Initially, however, hand calculations were carried out and during these, three peculiarities of the measurement became evident. The first point is that after starting the measurement, at least 100 seconds must elapse before any accurate results are obtained. This was due to errors made in measuring zero displacement and/or zero time. The effect that these errors had on the calcu-

lated value of  $k$  decreased as  $z$  and  $t$  increased and was negligible after about 100 seconds (fig. 2). The second point is that if the value of  $P/Q$  exceeds 0.8 the results become very inaccurate. The reason for this is evident on examining the graph of  $P/Q$  versus  $Kt\pi^2/4l^2$  (from table 1) shown in fig. 6. Above  $P/Q = 0.8$

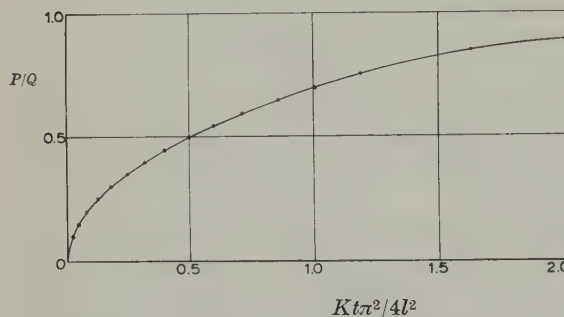


Fig. 6.  $P/Q$  vs  $Kt\pi^2/4l^2$  (from table 1).

the slope of the graph is such that a small error in  $P/Q$  gives a large error in  $Kt\pi^2/4l^2$ . For these reasons, if accurate results are to be obtained the measurement must be continued for more than 100 seconds and the value of  $P/Q$  must not attain or exceed a value of 0.8 before 100 seconds have elapsed.

These conditions can be satisfied by choosing a suitable length and diameter for the specimen. Care must be exercised in the choice of dimensions, as with too small a diameter, radial heat flow in the specimen becomes important and the theory shown above does not apply, whereas with too great a length it is difficult to maintain the specimen at a uniform temperature before the measurement is started.

The third point is that the quality of the ice used for the measurement had a large effect on the results. Ideally, this ice should be completely free from inclusions of air or water, but in practice this was difficult to achieve. Where inclusions did occur, an inclusion of air gave an apparent rise, and an inclusion of water gave an apparent fall, in thermal conductivity. The type of error that water inclusions produce is illustrated in fig. 2.

Although in theory it is possible to determine

the specific heat of the specimen by observing the total amount of ice melted during the test, the end point of the measurement is not sufficiently well-defined to do this. This is because when the measurement should be almost finished, the specimen begins to absorb heat from the apparatus and never actually comes to rest. This effect appears in the results as a gradual rise in the calculated value of  $k$  and can be seen in fig. 2 after  $t = 200$  seconds.

## 8. Conclusions

An effective method of measuring thermal diffusivity, which can be applied to irradiated uranium, has been devised. For the measurements made on brass, steel and uranium specimens with the apparatus and method described, the accuracy is better than  $\pm 5\%$  of the values quoted in the literature. For aluminium and copper, it is shown that if longer specimens were used the accuracy of the results would be improved.

The measurement is of the macroscopic thermal conductivity, i.e. the result is averaged over an area much greater than that of a single crystallite.

## Acknowledgements

This method of measuring thermal diffusivity was suggested by Dr. H. L. Ritz. The author was engaged on the testing of the method and design of the apparatus.

The author is grateful to C. A. Parsons & Co. Ltd., for permission to publish this work.

## Reference

- 1) H. S. Carslaw and J. C. Jaeger, *Conduction of Heat in Solids*, 2nd edition (Oxford, 1959)

## Appendix — Nomenclature

<i>A</i>	Area of cross section of specimen ( $\text{cm}^2$ )
<i>c</i>	Specific heat of specimen (c.g.s. units)
<i>k</i>	Thermal conductivity of specimen (c.g.s. units)
<i>l</i>	Length of specimen (cm)
<i>P</i>	Heat removed from specimen after time <i>t</i>

$Q$	Initial heat content of specimen (referred to $0^\circ\text{C}$ )	$\varrho$	Density of specimen (c.g.s. units)
$S$	Latent heat of fusion of ice (c.g.s. units)	$\varrho_{\text{ice}}$	Density of ice (c.g.s. units)
$t$	Time in seconds from the beginning of the test	$K$	Thermal diffusivity $k/c\varrho$
$T_0$	Initial temperature of the specimen ( $^\circ\text{C}$ )	$\frac{\partial\theta}{\partial z}$	Temperature gradient in the end of cylinder which is in contact with the ice.
$z_i$	Displacement of interface from its original position (in cm)	$P = A\varrho_{\text{ice}}S[z_i(0) - z_i(t_i)]$	
$z(t)$	Displacement of interface from its original position (in cm where $t$ denotes time)	$Q = A\varrho cT_0.$	

## KRYPTON EVOLUTION FROM METALLIC URANIUM

FRANCIS J. NORTON and C. W. TUCKER, Jr.

*General Electric Research Laboratory, Schenectady, N.Y., USA*

Received 27 June 1960

Krypton ions were put into uranium foil at 40 kV. The rate and temperature of release of the krypton gas was studied by the mass spectrometer. Evolution begins below 250° C and shows several peak rates. The temperature for release in this case is much lower than found in other work on fission gases formed *in situ*.

Des ions d'argon ont été introduits dans des lames d'uranium sous 40 kV. La vitesse et la température de dégagement du krypton ont été étudiées à l'aide d'un spectromètre de masse. Le dégazage commence en-dessous de 250° C et présente plusieurs pics de vitesse. La température dans ce cas est beaucoup plus faible

que celle trouvée dans d'autres travaux sur les gaz de fission formés *in situ*.

Kryptonionen wurden unter einer Spannung von 40 kV in Uranfolien eingeschossen. Anschliessend wurde die Geschwindigkeit des Entweichens von Kryptongas und die hierzu erforderliche Temperatur mit einem Massenspektrometer verfolgt. Die Gasabgabe beginnt unter 250° C und weist verschiedene Maxima der Geschwindigkeit auf. In diesem Fall ist also die für das Entweichen erforderliche Temperatur viel geringer als die Temperaturen, welche in anderen Arbeiten mit *in situ* gebildeten, gasförmigen Spaltprodukten gefunden wurden.

### 1. Introduction

Permeation rates of the rare gases through metals are exceedingly low under purely thermal conditions. However, if a rare gas is forced into a metal by ionic bombardment, its subsequent release on heating can readily be observed<sup>1,2</sup>).

In the case of formation of fission product gases *in situ*, other effects, such as bubble formation and changes in mechanical properties have been found<sup>3,4</sup>).

The diffusion of fission krypton from uranium has been measured<sup>5</sup>). Reynolds found that the diffusion of radiokrypton from specimens of irradiated uranium wire 60 mils (0.15 cm) diameter, 0.13 cm long was negligible at temperatures below 1000° C. At 1025-1075° C, and especially with cycling through the allotropic transition, some of the fission krypton could be recovered. He estimated the diffusion constant *D* to be no greater than  $10^{-15}$  cm<sup>2</sup> sec<sup>-1</sup> at 1025° C. Other investigators have found somewhat larger values<sup>4</sup>).

This paper is to report on the rate of release of krypton, forced into uranium foil as 40 kV ions, as the metal is heated in a mass spectrometer.

### 2. Experimental

Uranium discs 2 mils (50  $\mu$ ) thick, 0.13 cm diameter, weighing about 0.09 g each, were obtained from Hanford †. These were cleaned by electropolishing and annealed about  $\frac{1}{2}$  h in vacuum at 300° C. They were then bombarded by 40 kV krypton ions, the sample being at 25° C. The amount of bombardment was 2700 microamp-minutes. The bombardment took about 90 minutes.

The apparatus and technique used for ion bombardment is described in ref.<sup>3</sup>) and is similar to that used by others<sup>6</sup>).

After the bombardment was finished, dry

† We are indebted to Dr. D. R. Green of the Hanford Laboratories Operation for the sample of uranium.

nitrogen was admitted and the sample transferred to the mass spectrometer system for study of rare gas evolution on heating. This was done by the technique described by Norton<sup>7</sup>. The sample was placed in the side arm of an evacuated quartz glass tube which had been previously degassed above the temperatures to be used later. A thermocouple was at the central hot zone. The tube led directly to the mass spectrometer with no admission leak intervening. The mass spectrometer was set on the rare gas peak to be studied. From previous calibration through a leak system of known volume and known pump-out half-time, the height of the peak yielded directly the rate of rare gas evolution from the sample in absolute units of  $\text{cm}^3(\text{NTP})/\text{sec}$ . This gave a very sensitive measure of rate at each instant, and later the integration under the rate-time plot

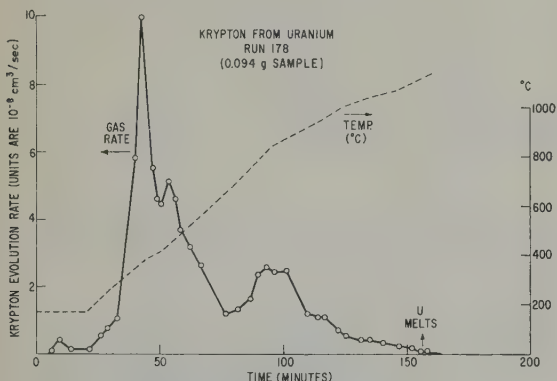


Fig. 1. Krypton from uranium, Run 178 (0.094 g sample).

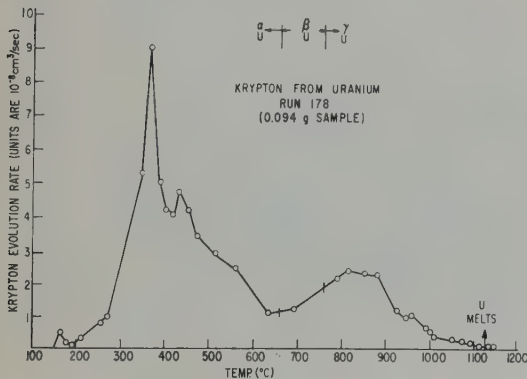


Fig. 2. Krypton from uranium, Run 178 (0.094 g sample).

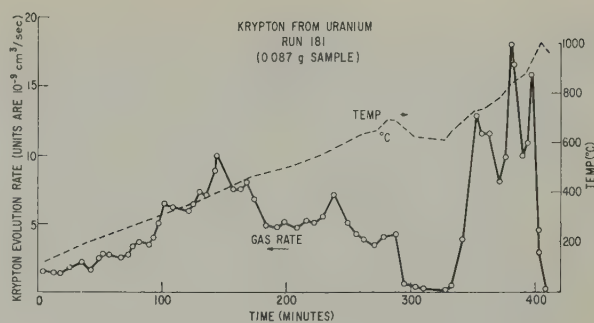


Fig. 3. Krypton from uranium, Run 181 (0.087 g sample).

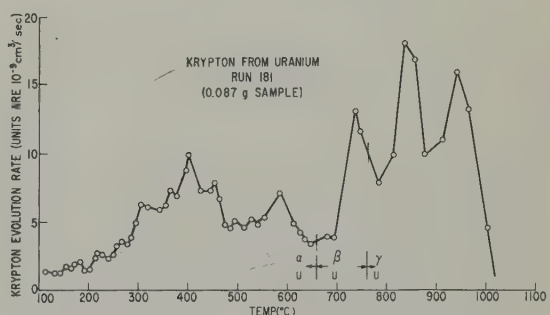


Fig. 4. Krypton from uranium, Run 181 (0.087 g sample).

gave the total amount. The temperature of the sample in the quartz glass evolution tube was gradually raised over a 2 to 8 hour period and the rare gas evolution rate continuously measured and recorded. Two sample discs of uranium were used, bombarded at the same time. The results for Run 178 are shown in graphs 1 and 2, and for Run 181 in graphs 3 and 4.

For Run 178 a rapid rate of temperature rise,  $8.8^\circ\text{C}$  per min, was employed at first. This gave a very high gas evolution rate peak, starting at about  $250^\circ\text{C}$  and comprising the temperature range  $300$ – $600^\circ\text{C}$ . A secondary smaller peak started just above the  $\alpha \rightarrow \beta$  uranium phase change at  $660^\circ\text{C}$ , and peaked just above the  $\beta \rightarrow \gamma$  change. After that the krypton evolution decreased as the temperatures went up. A temperature rise rate of  $4.3^\circ$  per minute was used above  $900^\circ\text{C}$ . No additional krypton was released on melting of the uranium.

Run 181 employed a much lower initial temperature rise rate of  $2.9^\circ\text{C}/\text{min}$ . A peak

appeared at 400°, smaller than in Run 178. There was a slow rate of release at 680° C, and on dropping the temperature to 600° C the rate decreased to a very low value. Then heating to 1000° C gave three high peaks and a drop to a low value at the end.

The amounts of krypton released, as obtained on integration of the time rate curves were, in units of  $\text{cm}^3$  krypton (NTP) per gram of uranium,

Run 178:  $1.55 \times 10^{-3}$

Run 181:  $1.45 \times 10^{-3}$ .

This amounts to a weight fraction for krypton of about  $5.5 \times 10^{-6}$ , or atom fraction of  $1.5 \times 10^{-5}$ , based on the weight of the whole disc of uranium, 2 mils thick.

The actual concentration of gas in the bombarded region is of course much higher than indicated by the preceding figures, due to the short range of the gas ions in the solid. The range of a 50 keV krypton ion in uranium can be estimated from the work of Nielsen<sup>8</sup>) to be approximately 200 Å. Based on this figure the amount of gas evolved corresponds to a concentration of 2 or 3 at % in the bombarded layer.

### 3. Discussion

The release of a rare gas from a metal at the low temperatures found in this investigation is striking. Fission product gases require much higher temperatures for release<sup>4,5</sup>). One essential difference in two cases is the mode of introduction of the gas. Ion bombardment is from outside into one side only, and it is possible that impact of these energetic ions produce damage paths in the metal through which the gas eventually can emerge. For fission products, such damage paths would be produced in the interior and in general not lead to the surface.

The difference in peak heights noted in Runs 178 and 181 may be explainable on this basis: the slower temperature rise of Run 181 gives more chance for annealing and healing of the

initial damage paths, resulting in a lower rate of krypton release at the lower temperatures. Later the phase changes occur and the emergence of the gas is aided by this. The work of Reynolds<sup>5</sup>) showed greater release of fission gases when he employed thermal cycling through the phase change region.

Ions put into metals by gas discharges may come out with difficulty. Blodgett and Vanderslice<sup>9</sup>) find extremely low rates of release, even at high temperatures, of neon, argon, krypton and xenon covered by sputtered tantalum and tungsten. The sputtered metal tightly seals in the gas atoms. The nature of the sputtered layer would govern the rate of release of the gas.

There seem to be three types of release of rare gases from metals, depending on how the gases arrived in the metal.

1. Fission gases put into uranium fuel by ion bombardment may be released easily at low temperatures.

2. Fission processes give gases which are released only with difficulty, at high temperatures.

3. Gas discharges can give ions buried in sputtered metal. These gases are not released until the metal is evaporated away.

### References

- 1) J. Koch, *Nature* **161** (1948) 566
- 2) C. W. Tucker, Jr. and F. J. Norton, *J. Nucl. Mat.* **2** (1960) 329
- 3) G. W. Greenwood, A. J. E. Foreman and D. E. Rimmer, *J. Nucl. Mat.* **1** (1959) 305
- 4) R. S. Barnes *et al.*, *Proc. 2nd Geneva Conf.* **5** (1958) 543
- 5) M. B. Reynolds, *Nucl. Sci. and Eng.* **1** (1956) 374
- 6) F. J. Norton, *J. Amer. Ceramic Soc.* **36** (1953) 90
- 7) O. Heinz, E. M. Gyorgy and R. S. Ohl, *Rev. Sci. Instr.* **27** (1956) 43
- 8) K. O. Nielsen, *Electromagnetically Enriched Isotopes and Mass Spectrometry*, Ed. M. L. Smith (Butterworths, London, 1956) pp. 68-81
- 9) K. B. Blodgett and T. A. Vanderslice, *J. Appl. Phys.* **31** (1960) 1017

LETTER TO THE EDITORS — LETTRE AUX REDACTEURS

THE PLASTIC DEFORMATION OF MONOCLINIC ALPHA PLUTONIUM

S. E. BRONISZ and A. E. GORUM †

*Los Alamos Scientific Laboratory, Los Alamos, New Mexico, USA and University of California*

Received 14 July 1960

One of the most interesting reasons, from our viewpoint, for studying the flow behavior of alpha plutonium is its unusual crystal structure. Zachariasen and Ellinger<sup>1)</sup> have reported that the structure is monoclinic, space group  $P2_1/m$ . Fig. 1 is a photograph of a ball model of this structure. The dark balls represent the sixteen atoms in one unit cell. Speculation on possible slip systems for this complex structure is complicated by the great differences in bond lengths and by the irregular packing. The (020) plane appears to be the most likely for slip, but a direction in this plane is not obvious.

The purpose of this investigation was to determine the effect of temperature and strain

rate on the plastic deformation of alpha plutonium and to determine the mode or modes of deformation which contribute to the plastic flow.

It has been reported by Gardner, Bloomster and Jefferes<sup>2)</sup> and Hampel<sup>3)</sup> that alpha plutonium is very brittle in tension. It was evident, therefore, that a study of the flow properties could best be made by means of compression tests.

Since it has not yet been possible to prepare large grains of alpha plutonium, all experiments were performed with fine-grained polycrystalline specimens. The specimens were in the form of right cylinders 0.9 cm ( $\frac{3}{8}$  in) long and 0.6 cm

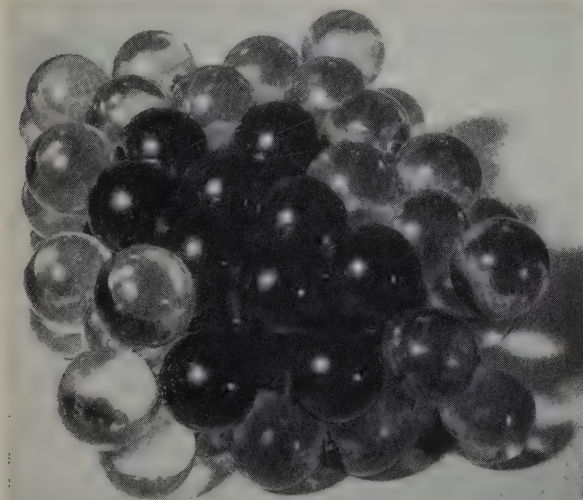


Fig. 1. A ball model of the alpha plutonium crystal structure.

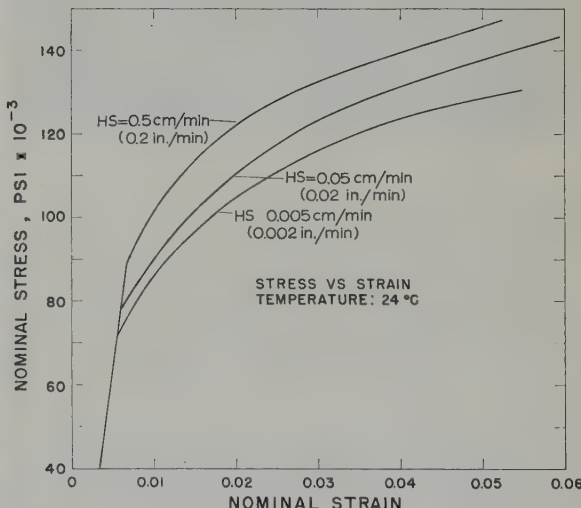


Fig. 2. The effect of strain rate on the compression stress-strain curves for alpha plutonium at room temperature.

† Presently with Rheem Semiconductor Corporation, Mountain View, California.

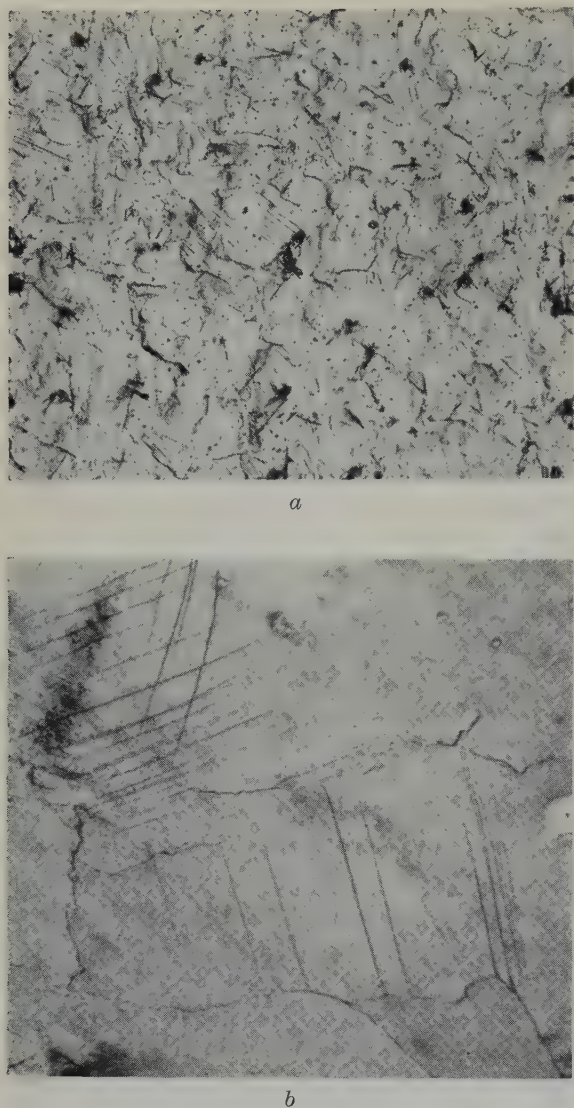


Fig. 3. Deformation of alpha plutonium caused by 4 % strain.

- a. General view showing orange peel structure, slip lines and possible grain boundary sliding.  $\times 100$ .
- b. Another area of the same specimen showing grain boundaries revealed by deformation and two sets of slip lines in one grain.  $\times 1500$ .

( $\frac{1}{4}$  in) in diameter. In addition, each specimen used in investigating the deformation mode had a flat portion ground on its side.

The total impurity content of the specimens was approximately 500 ppm. The major impurities were: carbon (135 ppm), iron (140 ppm) and nickel (85 ppm).

The stress-strain compression tests were run in an oil bath at temperatures ranging from 24° C (room temperature) to 100° C and at head speeds ranging from 0.005 to 0.5 cm/min (0.002 to 0.2 in./min). It was found that the yield stress of alpha plutonium varies directly with strain rate and inversely with temperature. The stress-strain curves obtained at room temperature are given in fig. 2. The total deformation in compression ranged from 20 % at room temperature to 80 % at 100° C. This is not indicated in the figure, because extensive barreling in the specimens beyond a few percent strain made nominal stress calculations meaningless.

In order to explore the deformation mode, the flat, side surface on each specimen was metallographically polished. Then strain was applied to the specimen in small increments and the progress of the resulting deformation observed microscopically. After the application of a strain of 1 %, an orange peel structure began to form. Further straining caused this structure to become more pronounced. At approximately 2 % strain, slip lines were first observed and apparently some grain boundary sliding occurred. Additional straining resulted in the orange peel structure becoming even more pronounced, and also resulted in an increase in the number of visible slip lines. Part a of fig. 3 illustrates the orange peel structure, the slip lines and the grain boundary sliding. Part b of the same figure shows the slip lines at higher magnification. The fact that some of these lines cross indicated that more than one slip system was in operation. Repolishing the flat surfaces after deformation obliterated all traces of deformation.

Although no evidence of twinning was seen in the flat sided specimens, metallographically prepared sections of the stress-strain specimens revealed the presence of twin-like bands. Examples of these are shown in fig. 4. Examination of these sections of the several specimens used at the various temperatures disclosed that the bands became more numerous at higher temperatures.

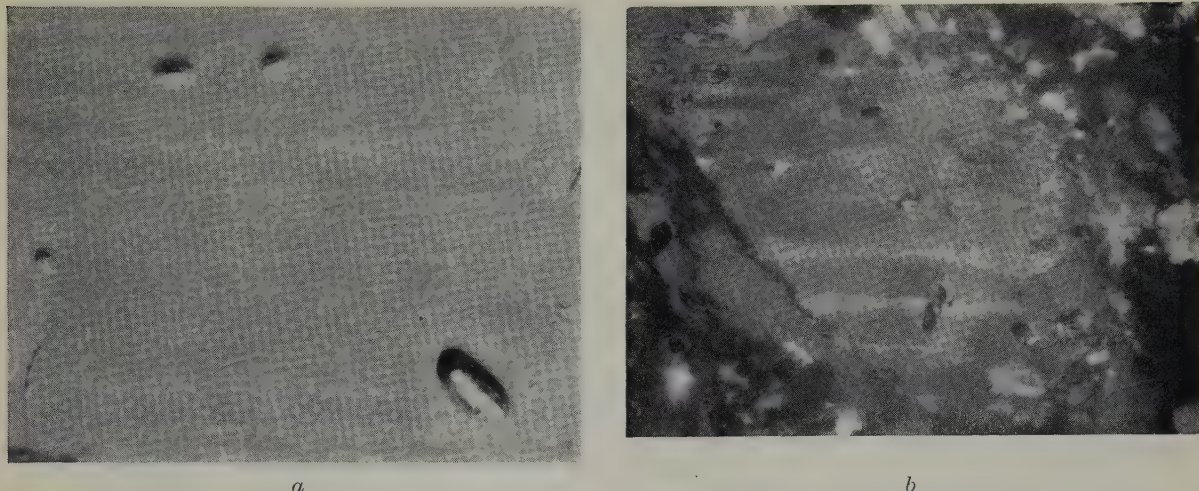


Fig. 4. Metallographically prepared section of a specimen strained in compression at 75°C. *a*. Twin bands as seen under bright field illumination. The specimen was etched and slightly anodized. 1000  $\times$ . *b*. Another area of the same specimen as seen under polarized light. 330  $\times$ .

It would seem then that alpha plutonium deforms primarily by slip, but that twinning and possibly grain boundary sliding contribute to the deformation. The two observations, grain boundary sliding at room temperature and an increase in the ease of twinning with an increase in temperature, are contradictory to the observed behavior of other materials. The explanation of this paradox may lie in the complicated crystal structure of alpha plutonium. Hopefully, it will be elucidated when plutonium of higher

purity and larger grain size becomes available and when a better understanding is gained of the forces involved during the straining of this material.

### References

- 1) W. H. Zachariasen and F. Ellinger, *J. Chem. Phys.* 27, No. 3 (1957) 811
- 2) H. R. Gardner, C. H. Bloomster and J. M. Jefferes, Proc. 2nd Geneva Conf. 6 (1958) 686
- 3) C. A. Hampel (Ed.), *Plutonium*, a chapter to be included in Rare Metals Handbook (in press)

## BOOK REVIEWS

C. E. CROUTHAMEL (Ed.) *Applied Gamma-Ray Spectrometry*. (International Series of Monographs on Analytical Chemistry). (Pergamon Press. ix + 443 pages. 1960. 50s.)

This is really two books in one. The first three chapters are written primarily with the physicist in mind, and are devoted to the physics of  $\gamma$ -ray emission, and the principles of operation, calibration and "diseases" of scintillation counters and their various constituent parts. The fourth chapter is devoted almost exclusively to a detailed account of the technique of *radioactivation analysis* for determining the concentration of impurities, or of individual isotopes. The sensitivity and accuracy of the technique are critically considered, and compared with the capacities of the mass spectrometric method. The link between the two sections of the book is, of course, the fact that  $\gamma$ -ray spectrometry is the chief tool in activation analysis.

An appendix, which occupies more than half the book, reproduces a large number of  $\gamma$ -ray spectra of individual radioactive isotopes. Using this information, the analyst can set his scintillation counting equipment to measure the radiation of a particular isotope and discriminate against other radiations which may be present.

R. W. CAHN

*Faraday Society's Discussion on CRYSTAL GROWTH* (1949). (Reprinted by Butterworths Scientific Publications, London, 366 pages. 1959, 60s.)

This is a reprint of a collection of papers which has become a classic of its subject. It has for some time been out of print, and this reprint has been issued in response to numerous requests received by the Faraday Society. For those unfamiliar with these papers, the section headings sufficient indicate their scope: I. Theory of Crystal Growth. II. Nucleation and Normal Growth. III. Abnormal and Modified Crystal Growth. IV. Mineral Synthesis and Technical Aspects. Section I includes the original paper by Frank predicting the formation of growth spirals on crystals containing dislocations.

R. W. CAHN

G. L. MILLER, *Tantalum and Niobium* (Butterworths Scientific Publications, London. 1959, 120s.)

The book is a compilation of almost everything which is known about the technology of the two metals tantalum and niobium. There are chapters on the occurrence, extraction and the separation of the metals, and on their production, consolidation and fabrication. Further chapters cover corrosion both by gases and liquid metals, the physical and structural properties, the binary constitutional diagrams of the metals, and finally the compounds which are important in the manufacture in what are usually known as the hard metals, that is to say, the carbides, nitrides, silicides and borides. The technologist faced with a problem involving either tantalum or niobium will be able, almost certainly, to find material relevant to his problem in the book, which, as an assembly of factual information, is indeed impressive. On the technological side it appears to be extremely comprehensive, but it must be regarded strictly as a reference book. It is very probable that the author intended that it should be just such a source book.

At the present stage of development of the metallurgy of tantalum and niobium, it is unlikely that any one man could give a critical review of all aspects of the literature which has already accumulated about the treatment and behaviour of the two metals. It is doubtful if enough is known about the fundamental behaviour of the metals to allow an author to assess the often conflicting claims of various workers. In the fields of extraction, separation, and production of the metals, where the author must be considered to be an expert, critical appraisal of results is very evident. In other fields such as physical and structural properties, and binary constitutional diagrams there is naturally a tendency for the author to be less critical. Very fairly, where the results of a number of workers are at variance, he gives all points of view. While this is valuable in supplying the necessary references, it makes this part of the book rather difficult to read as a continuous narrative. Indeed this is not the book for anyone wishing to gain merely a general outline of the properties of tantalum and niobium, but rather an essential tool for the practical metallurgist who is deeply involved in work on the metals.

On the scientific side understandably no attempts are made to relate the work already carried out on deformation mechanisms, which is described in a few pages, with the general deformation behaviour of the metals, nor is there any discussion of the way in which physical and alloying properties may be related to the electronic structure. It was also noted that a number

of rather interesting Russian and Polish papers concerned with physical properties had been missed. The author's achievements on the technological side are, however, sufficiently great to allow us to forgive him for not writing the perfect scientific, as well as a first class technological review of the metallurgy of tantalum and niobium.

A. D. MCQUILLAN

## CORRECTIONS

In the review of the book entitled "Fluid Fuel Reactors", J. Nucl. Mat. 2 (1960) 94, the address of the publishers, the Addison-Wesley Publishing Company Inc. was incorrectly given. The correct address is: Reading, Massachusetts, U.S.A.

Mme. J. Lehmann and R. F. Hills. — Proposed Nomenclature for Phases in Uranium Alloys (J. Nucl. Mat. 2 (1960) 261).

In the English version of table 1 of this paper, the seventh entry in the right-hand column should read  $\gamma_a$ , not  $\gamma_a'$  as printed. The French version of the table is correct.

## NEWS ITEM

### THE FARADAY SOCIETY

A General Discussion

on

### "RADIATION EFFECTS IN INORGANIC SOLIDS"

will be held by kind invitation, at the

Centre d'Etudes Nucléaires de Saclay, Gif-sur-Yvette (S.- et O.), France on the 11th and 12th April 1961.

The discussion, which will be confined to high-energy radiation, will be divided into three main sections:

- (1) Metals and alloys.
- (2) Semi-conductors and graphite.
- (3) Ionic crystals.

Further particulars will be issued in due course.



## AUTHOR INDEX

ANG, C. Y. and E. W. BURKHAMMER, Sintering of high density uranium dioxide bodies (Letter to the Editors) . . . . . 176

ANTILL, J. E. and K. A. PEAKALL, Attack of graphite by an oxidising gas at low partial pressures and high temperatures . . . . . 31

ANTILL, J. E., *see* PEAKALL

AYLMORE, D. W., S. J. GREGG and W. B. JEPSON, The high temperature oxidation of beryllium. Part I. In dry oxygen . . . . . 169

BANNISTER, G. H., R. C. BURNETT and Miss J. R. MURRAY, Ageing and hot hardness characteristics of certain thorium alloys. . . . . 51

BEL, A., R. DELMAS et B. FRANÇOIS, Le frittage des oxydes d'uranium (Lettre aux Rédacteurs) 192

BERMAN, R. M., M. L. BLEIBERG and W. YENISCAVICH, Fission fragment damage to crystal structures . . . . . 129

BLACKBURN, W. S.,  $\alpha$ - $\beta$  thermal cycling of uranium (Letter to the Editors) . . . . . 191

BLANCHARD, R., J. PELLISSIER et M. PLUCHERY, Effets de l'hydrogène sur les caractéristiques de rupture par traction d'acières inoxydables 216

BLEIBERG, M. L., *see* BERMAN

BLEWITT, T. H., R. R. COLTMAN, R. E. JAMISON, and J. K. REDMAN, Radiation hardening of copper single crystals . . . . . 277

BLOCH, Mme J., Changement de phase et mise en désordre par irradiation du composé U<sub>2</sub>Mo (Lettre aux Rédacteurs) . . . . . 90

BLUMENTHAL, BERNHARD, The transformation temperatures of high-purity uranium . . . . . 23

BLUMENTHAL, BERNHARD, Constitution of low carbon U-C alloys . . . . . 197

BRETT, N. H., *see* RUSSELL

BRONISZ, S. E. and A. E. GORUM, The plastic deformation of monoclinic alpha plutonium (Letter to the Editors) . . . . . 353

BURKHAMMER, E. W., *see* ANG

BURNETT, R. C., *see* BANNISTER

CAHN, R. W. and Mrs. H. TOMLINSON, The nature of subgrain boundaries due to phase transformation in uranium (Letter to the Editors) 88

CHANG, ROGER, Phase transformation, twinning and anelastic phenomenon associated with zirconium dihydride. . . . . 335

COLTMAN, R. R., *see* BLEWITT

COSTA, P., Détermination du pouvoir thermoelectrique de l'uranium et du plutonium . . . . . 75

DANIEL, J. L., *see* NEWKIRK

DELMAS, R., *see* BEL

DWIGHT, AUSTIN E., The uranium-molybdenum equilibrium diagram below 900° C . . . . . 81

ENGLANDER, M., *see* LANIESSE

EVANS, D. S., G. V. RAYNOR and R. T. WEINER, The lattice spacings of thorium-lanthanum alloys . . . . . 121

EVANS, D. S. and G. V. RAYNOR, Lattice spacings in thorium-yttrium alloys . . . . . 209

FRANÇOIS, B., *see* BEL

GARDINER, K. M., *see* YOUNG

GONSER, ULRICH, Strahlungswachstum von  $\alpha$ -Uran als Ergebnis korrelativer Stossprozesse 43

GORUM, A. E., *see* BRONISZ

GREGG, S. J., *see* AYLMORE

GREGG, S. J., R. J. HUSSEY and W. B. JEPSON, The high temperature oxidation of beryllium. Part II. The reaction with carbon dioxide and with carbon monoxide . . . . . 225

HARRISON, J. D. L., *see* RUSSELL

HILLS, R. F., *see* LEHMANN

HOWE, L. M. and W. R. THOMAS, The effect of neutron irradiation on the tensile properties of zircaloy-2 . . . . . 248

HUSSEY, R. J., *see* GREGG

JAMISON, R. E., *see* BLEWITT

JEPSON, W. B., *see* AYLMORE

JEPSON, W. B., *see* GREGG

LANIESSE, Mme J., P. MERIEL et M. ENGLANDER, Etude aux neutrons de la texture cristalline de barreaux d'uranium . . . . . 69

LEHMANN, Mme J., Processus des transformations dans les alliages uranium-molybdène de faibles teneurs en molybdène . . . . . 152

LEHMANN, Mme J. et R. F. HILLS, Nomenclature proposée pour les phases des alliages d'uranium — Proposed nomenclature for phases in uranium alloys. . . . . 261

LIBOWITZ, G. G., The nature and properties of transition metal hydrides (Review Article) . . . . . 1

LLOYD, LOWELL T., Recrystallization of deformed alpha-uranium single crystals . . . . . 141

MASTEL, B., *see* NEWKIRK

MERIEL, P., *see* LANIESSE

MURRAY, Miss J. R., *see* BANNISTER

NEWKIRK Jr., H. W., J. L. DANIEL and B. MASTEL, Electron microscope studies of damage in irradiated uranium dioxide (Letter to the Editors) . . . . . 269

NORTON, F. J., *see* TUCKER

NORTON, F. J. and C. W. TUCKER Jr., Krypton evolution from metallic uranium . . . . . 350

PEAKALL, K. A., *see* ANTILL

PEAKALL, K. A. and J. E. ANTILL, Oxidation of uranium dioxide in air at 350–1000° C (Letter to the Editors) . . . . . 194

PELISSIER, J., *see* BLANCHARD

PLUCHERY, M., *see* BLANCHARD

PORTNOFF–PORNEUF, A., Aspects fractographiques du bioxyde d'uranium fritté (Lettre aux Rédacteurs) . . . . . 181

PORTNOFF–PORNEUF, A., Clivage du bioxyde d'uranium (Lettre aux Rédacteurs) . . . . . 186

RAYNOR, G. V., *see* EVANS

REDMAN, J. K., *see* BLEWITT

ROBINS, R. G., Growth habit of electrodeposited uranium dioxide single crystals (Letter to the Editors) . . . . . 189

ROOF Jr., R. B., An experimental determination of the characteristic temperature for  $\text{PuO}_2$  39

ROTSEY, W. B., *see* YOUNG

RUSSELL, L. E., J. D. L. HARRISON and N. H. BRETT, Perovskite-type compounds based on plutonium . . . . . 310

SAULNIER, A., Etude structurale du beryllium par micrographie et microdiffraction électro- niques sur coupes minces . . . . . 299

SAWATZKY, A., The diffusion and solubility of hydrogen in the alpha-phase of zircaloy-2. . 62

SAWATZKY, A., Hydrogen in zircaloy-2: its distribution and heat of transport . . . . . 321

SCHANER, B. E., Metallographic determination of the  $\text{UO}_2\text{-U}_4\text{O}_9$  phase diagram . . . . . 110

SMART, D., A method suitable for the measurement of the thermal diffusivity of irradiated materials. . . . . 341

STOBO, J. J., Alpha-beta cycling of uranium . 97

THOMAS, W. R., *see* HOWE

Tomlinson, Mrs. H., *see* CAHN

TUCKER Jr., C. W. and F. J. NORTON, On the location and motion of rare gas atoms in metals . . . . . 329

TUCKER Jr., C. W., *see* NORTON

WALKER, R. M., On the production of displaced atoms by thermal neutrons . . . . . 147

WEINER, R. T., *see* EVANS

WILLIAMS, J., The sintering of uranium oxides (Discussion of paper by BEL, DELMAS and FRANÇOIS, J. Nucl. Mat. 1 (1959) 259.) (Letter to the Editors) . . . . . 92

YENISCAVICH, W., *see* BERMAN

YOUNG, A. G., K. M. GARDINER and W. B. ROTSEY, The plastic deformation of alpha-uranium . . . . . 234

## BOOK REVIEWS

BENESOVSKY, F., (Editor) Plansee Proceedings 1958 (R. W. CAHN) . . . . . 275

Colloque sur la Diffusion à l'Etat Solide. (Saclay 3, 4, 5 juillet 1958) (D. H. TOMLIN) . . . . 196

CROUTHAMEL, C. E., (Editor) Applied Gamma-Ray Spectrometry (R. W. CAHN) . . . . . 356

Faraday Society's Discussion on Crystal Growth (1949) (R. W. CAHN) . . . . . 356

Fuel Elements Conference. (USAEC) (R. W. CAHN) . . . . . 96

LANE, J. A., H. G. MACPHERSON and F. MASLAN (Editors), Fluid Fuel Reactors (B. T. R. FROST) (See also correction p. 357). . . . . 94

MILLER, G. L., Tantalum and Niobium (A. D. McQUILLAN) . . . . . 356

Nuclear Metallurgy, Volumes I–VI, 1955–1959 (AIME) (R. W. CAHN) . . . . . 276

ROUGH, F. A. et A. A. BAUER, Constitution of Uranium and Thorium Alloys (G. CABANE) . . . . . 94

STARR, CHAUNCEY and R. W. DICKINSON, Sodium Graphite Reactors (JOHN P. HOWE) . . . . . 274

Summaries of Physical Research in Metallurgy, Solid State Physics and Ceramics. (USAEC) (R. W. CAHN) . . . . . 96

## SUBJECT INDEX

### Alloys (*Constitution*)

The uranium-molybdenum equilibrium diagram below 900° C, AUSTIN E. DWIGHT . . . . .	81
Processus des transformations dans les alliages uranium-molybdène de faibles teneurs en molybdène, Mme J. LEHMANN . . . . .	152
Constitution of low carbon U-C alloys, BERNHARD BLUMENTHAL . . . . .	197
Nomenclature proposée pour les phases des alliages d'uranium – Proposed nomenclature for phases in uranium alloys, Mme J. LEHMANN and R. F. HILLS . . . . .	261

### Alloys (*Properties and Preparation*)

Ageing and hot hardness characteristics of certain thorium alloys, G. H. BANNISTER, R. C. BURNETT and Miss J. R. MURRAY . . . . .	51
Processus des transformations dans les alliages uranium-molybdène de faibles teneurs en molybdène, Mme J. LEHMANN . . . . .	152
Effets de l'hydrogène sur les caractéristiques de rupture par traction d'acières inoxydables, R. BLANCHARD, J. PELISSIER et M. PLUCHERY . . . . .	216

### Beryllium

The high temperature oxidation of beryllium. Part I. In dry oxygen, D. W. AYLMORE, S. J. GREGG and W. B. JEPSON . . . . .	169
The high temperature oxidation of beryllium. Part. II. The reaction with carbon dioxide and with carbon monoxide, S. J. GREGG, R. J. HUSSEY and W. B. JEPSON . . . . .	225
Etude structurale du beryllium par micrographie et microdiffraction électroniques sur coupes minces, A. SAULNIER . . . . .	299

### Ceramics

The sintering of uranium oxides (Letter to the Editors), J. WILLIAMS . . . . .	92
Metallographic determination of the $UO_2-U_4O_9$ phase diagram, B. E. SCHANER . . . . .	110
Sintering of high density uranium dioxide bodies (Letter to the Editors), C. Y. ANG and E. W. BURKHAMMER . . . . .	176
Aspects fractographiques du b oxyde d'uranium fritté (Lettre aux Rédacteurs), A. PORTNOFF-PORNEUF . . . . .	181
Clivage du b oxyde d'uranium (Lettre aux Rédacteurs), A. PORTNOFF-PORNEUF . . . . .	186
Growth habit of electrodeposited uranium dioxide single crystals (Letter to the Editors), R. G. ROBINS . . . . .	189
Le frittage des oxydes d'uranium (Lettre aux Rédacteurs), A. BEL, R. DELMAS et B. FRANÇOIS . . . . .	192
Oxidation of uranium dioxide in air at 350–1000° C (Letter to the Editors), K. A. PEAKALL and J. E. ANTILL . . . . .	194
Constitution of low carbon U-C alloys, BERNHARD BLUMENTHAL . . . . .	197
Electron microscope studies of damage in irradiated uranium dioxide (Letter to the Editors), H. W. NEWKIRK Jr., J. L. DANIEL and B. MASTEL . . . . .	269

### Corrosion (*including Oxidation*)

Attack of graphite by an oxidising gas at low partial pressures and high temperatures, J. E. ANTILL and K. A. PEAKALL . . . . .	31
The diffusion and solubility of hydrogen in the alpha-phase of zircaloy-2, A. SAWATZKY . . . . .	62
The high temperature oxidation of beryllium. Part I. In dry oxygen, D. W. AYLMORE, S. J. GREGG and W. D. JEPSON . . . . .	169
Oxidation of uranium dioxide in air at 350–1000° C, (Letter to the Editors), K. A. PEAKALL and J. E. ANTILL . . . . .	194
The high temperature oxidation of beryllium. Part II. The reaction with carbon dioxide and with carbon monoxide, S. J. GREGG, R. J. HUSSEY and W. B. JEPSON . . . . .	225
Hydrogen in zircaloy-2: its distribution and heat of transport, A. SAWATZKY . . . . .	321

## Crystallographic Data

The nature and properties of transition metal hydrides, G. C. LIBOWITZ . . . . .	1
An experimental determination of the characteristic temperature for $\text{PuO}_2$ , R. B. ROOF, Jr. . . . .	39
Etude aux neutrons de la texture cristalline de barreaux d'uranium, Mme J. LANIESSE, P. MERIEL et M. ENGLANDER . . . . .	69
The nature of subgrain boundaries due to phase transformation in uranium (Letter to the Editors), R. W. CAHN and Mrs. H. TOMLINSON . . . . .	88
The lattice spacings of thorium-lanthanum alloys, D. S. EVANS, G. V. RAYNOR and R. T. WEINER . . . . .	121
Fission fragment damage to crystal structures, R. M. BERMAN, M. L. BLEIBERG and W. YENISCAVICH . . . . .	129
Recrystallization of deformed alpha-uranium single crystals, LOWELL T. LLOYD . . . . .	141
Lattice spacings in thorium-yttrium alloys, D. S. EVANS and G. V. RAYNOR . . . . .	209
Perovskite-type compounds based on plutonium, L. E. RUSSELL, J. D. L. HARRISON and N. H. BRETT . . . . .	310
Phase transformation, twinning and anelastic phenomenon associated with zirconium dihydride, ROGER CHANG . . . . .	335

## Diffusion

Phase transformation, twinning and anelastic phenomenon associated with zirconium dihydride, ROGER CHANG . . . . .	335
--	-----

## Experimental Techniques

The diffusion and solubility of hydrogen in the alpha-phase of zircaloy-2, A. SAWATZKY . . . . .	62
Effets de l'hydrogène sur les caractéristiques de rupture par traction d'acières inoxydables, R. BLANCHARD, J. PELISSIER et M. PLUCHERY . . . . .	216
Hydrogen in zircaloy-2: its distribution and heat of transport, A. SAWATZKY . . . . .	321
On the location and motion of rare gas atoms in metals, C. W. TUCKER, Jr., and F. J. NORTON . . . . .	329
A method suitable for the measurement of the thermal diffusivity of irradiated materials, D. SMART . . . . .	341
Krypton evolution from metallic uranium, F. J. NORTON and C. W. TUCKER . . . . .	350

## Gazes in Metals

Hydrogen in zircaloy-2: its distribution and heat of transport, A. SAWATZKY . . . . .	321
---	-----

## Graphite

Attack of graphite by an oxidising gas at low partial pressures and high temperatures, J. E. ANTILL and K. A. PEAKALL . . . . .	31
---	----

## Hydrides

The nature and properties of transition metal hydrides, G. G. LIBOWITZ . . . . .	1
Hydrogen in zircaloy-2: its distribution and heat of transport, A. SAWATZKY . . . . .	321
Phase transformation, twinning and anelastic phenomenon associated with zirconium dihydride, ROGER CHANG . . . . .	335

## Impurities

The diffusion and solubility of hydrogen in the alpha-phase of zircaloy-2, A. SAWATZKY . . . . .	62
Effets de l'hydrogène sur les caractéristiques de rupture par traction d'acières inoxydables, R. BLANCHARD, J. PELISSIER et M. PLUCHERY . . . . .	216
Etude structurale du beryllium par micrographie et microdiffraction électroniques sur coupes minces, A. SAULNIER . . . . .	299
Hydrogen in zircaloy-2: its distribution and heat of transport, A. SAWATZKY . . . . .	321
On the location and motion of rare gas atoms in metals, C. W. TUCKER Jr. and F. J. NORTON . . . . .	329
Krypton evolution from metallic uranium, FRANCIS J. NORTON and C. W. TUCKER Jr. . . . .	350

Irradiation Damage (*Theory and Experiment*)

Strahlungswachstum von $\alpha$ -Uran als Ergebnis korrelativer Stoßprozesse, ULRICH GONSER . . . . .	43
Changement de phase et mise en désordre par irradiation du composé $U_2Mo$ (Lettre aux Rédacteurs), Mme J. BLOCH . . . . .	90
Fission fragment damage to crystal structures, R. M. BERMAN, M. L. BLEIBERG and W. YENISCAVICH . . . . .	129
On the production of displaced atoms by thermal neutrons, R. M. WALKER . . . . .	147
The effect of neutron irradiation on the tensile properties of zircaloy-2, L. M. HOWE and W. R. THOMAS . . . . .	248
Electron microscope studies of damage in irradiated uranium dioxide (Letter to the Editors), H. W. NEWKIRK JR., J. L. DANIEL and B. MASTEL . . . . .	269
Radiation hardening of copper single crystals, T. H. BLEWITT, R. R. COLTMAN, R. E. JAMISON and J. K. REDMAN . . . . .	277
A method suitable for the measurement of the thermal diffusivity of irradiated materials, D. SMART . . . . .	341

## Mechanical Properties

Effets de l'hydrogène sur les caractéristiques de rupture par traction d'acières inoxydables, R. BLANCHARD, J. PELLISSIER et M. PLUCHERY . . . . .	216
The plastic deformation of alpha-uranium, A. G. YOUNG, K. M. GARDINER and W. B. ROTSEY . . . . .	234
The effect of neutron irradiation on the tensile properties of zircaloy-2, L. M. HOWE and W. R. THOMAS . . . . .	248
Radiation hardening of copper single crystals, T. H. BLEWITT, R. R. COLTMAN, R. E. JAMISON and J. K. REDMAN . . . . .	277
The plastic deformation of monoclinic alpha plutonium (Letter to the Editors), S. E. BRONISZ and A. E. GORUM . . . . .	353

## News Item

The Faraday Society . . . . .	357
-------------------------------	-----

## Phase Transformations

The transformation temperatures of high-purity uranium, BERNHARD BLUMENTHAL . . . . .	23
The uranium-molybdenum equilibrium diagram below 900° C, AUSTIN E. DWIGHT . . . . .	81
The nature of subgrain boundaries due to phase transformation in uranium (Letter to the Editors), R. W. CAHN and Mrs H. TOMLINSON . . . . .	88
Changement de phase et mise en désordre par irradiation du composé $U_2Mo$ (Letter to the Editors), Mme J. BLOCH . . . . .	90
Processus des transformations dans les alliages uranium-molybdène de faibles teneurs en molybdène, Mme J. LEHMANN . . . . .	152
Phase transformation, twinning and anelastic phenomenon associated with zirconium dihydride, ROGER CHANG . . . . .	335

## Physical Properties

The nature and properties of transition metal hydrides, G. G. LIBOWITZ . . . . .	1
Détermination ou pouvoir thermo-électrique de l'uranium et du plutonium, P. COSTA . . . . .	75

## Plutonium and Plutonium Compounds

An experimental determination of the characteristic temperature for $PuO_2$ , R. B. ROOF JR. . . . .	39
Détermination du pouvoir thermo-électrique de l'uranium et du plutonium, P. COSTA . . . . .	75
Perovskite-type compounds based on plutonium, L. E. RUSSELL, J. D. L. HARRISON and N. H. BRETT . . . . .	310
The plastic deformation of monoclinic alpha plutonium (Letter to the Editors), S. E. BRONISZ and A. E. GORUM . . . . .	353

## Powder Processes

The sintering of uranium oxides (Letter to the Editors), J. WILLIAMS . . . . .	92
Sintering of high density uranium dioxide bodies (Letter to the Editors), C. Y. ANG and E. W. BURKHAMMER . . . . .	176
Le frittage des oxydes d'uranium (Letter to the Editors), A. BEL, R. DELMAS et B. FRANÇOIS . . . . .	192

## Thorium and Thorium Alloys

Ageing and hot hardness characteristics of certain thorium alloys, G. H. BANNISTER, R. C. BURNETT and Miss J. R. MURRAY . . . . .	51
The lattice spacings of thorium-lanthanum alloys, D. S. EVANS, G. V. RAYNOR and R. T. WEINER . . . . .	121
Lattice spacings in thorium-yttrium alloys, D. S. EVANS and G. V. RAYNOR . . . . .	209

## Uranium and Uranium Alloys

The transformation temperatures of high-purity uranium, BERNHARD BLUMENTHAL . . . . .	23
Strahlungswachstum von $\alpha$ -Uran als Ergebnis korrelativer Stossprozesse, ULRICH GONSER . . . . .	43
Détermination du pouvoir thermo-électrique de l'uranium et du plutonium, P. COSTA . . . . .	75
The uranium-molybdenum equilibrium diagram below 900° C, AUSTIN E. DWIGHT . . . . .	81
The nature of subgrain boundaries due to phase transformation in uranium (Letter to the Editors), R. W. CAHN and Mrs H. TOMLINSON . . . . .	88
Changement de phase et mise en désordre par irradiation du composé U <sub>2</sub> Mo, Mme J. BLOCH . . . . .	90
The sintering of uranium oxides (Letter to the Editors), J. WILLIAMS . . . . .	92
Alpha-beta cycling of uranium, J. J. STOBO . . . . .	97
Recrystallization of deformed alpha-uranium single crystals, LOWELL T. LLOYD . . . . .	141
Processus des transformations dans les alliages uranium-molybdène de faibles teneurs en molybdène, Mme J. LEHMANN . . . . .	152
$\alpha$ - $\beta$ thermal cycling of uranium (Letter to the Editors), W. S. BLACKBURN . . . . .	191
Le frittage des oxydes d'uranium (Lettre aux Rédacteurs), A. BEL, R. DELMAS et B. FRANÇOIS . . . . .	192
Constitution of low carbon U-C alloys, BERNHARD BLUMENTHAL . . . . .	197
The plastic deformation of alpha-uranium, A. G. YOUNG, K. M. GARDINER and W. B. ROTSEY . . . . .	234
Nomenclature proposée pour les phases des alliages d'uranium. Proposed nomenclature for phases in uranium alloys, Mme J. LEHMANN and R. F. HILLS . . . . .	261
Krypton evolution from metallic uranium, FRANCIS J. NORTON and C. W. TUCKER Jr. . . . .	350

## Uranium Carbides

Constitution of low carbon U-C alloys, BERNHARD BLUMENTHAL . . . . .	197
--	-----

## Uranium Oxides

Metallographic determination of the UO <sub>2</sub> -U <sub>4</sub> O <sub>9</sub> phase diagram, B. E. SCHANER . . . . .	110
Fission fragment damage to crystal structures, R. M. BERMAN, M. L. BLEIBERG and W. YENISCAVICH . . . . .	129
Sintering of high density uranium dioxide bodies (Letter to the Editors), C. Y. ANG and E. W. BURKHAMMER . . . . .	176
Aspects fractographiques du bioxyde d'uranium fritté (Lettre aux Rédacteurs), A. PORTNOFF-PORNEUF . . . . .	181
Clivage du bioxyde d'uranium (Lettre aux Rédacteurs), A. PORTNOFF-PORNEUF . . . . .	186
Growth habit of electrodeposited uranium dioxide single crystals (Letter to the Editors), R. G. ROBINS . . . . .	189
Le frittage des oxydes d'uranium (Lettre aux Rédacteurs), A. BEL, R. DELMAS et B. FRANÇOIS . . . . .	192
Oxidation of uranium dioxide in air at 350-1000° C (Letter to the Editors), K. A. PEAKALL and J. E. ANTILL . . . . .	194
Electron microscope studies of damage in irradiated uranium dioxide (Letter to the Editors), H. W. NEWKIRK Jr., J. L. DANIEL and B. MASTEL . . . . .	269

## Zirconium and Zirconium Alloys

The diffusion and solubility of hydrogen in the alpha-phase of zircaloy-2, A. SAWATZKY . . . . .	62
The effect of neutron irradiation on the tensile properties of zircaloy-2, L. M. HOWE and W. R. THOMAS . . . . .	248
Hydrogen in zircaloy-2: its distribution and heat of transport, A. SAWATZKY . . . . .	321



**DATE DUE**

**RENEWALS**  
**996-2724**

DEMCO 38-297